FOCUSING, IMAGING AND RESONACE PROPERTIES OF MICROPHOTONICS STRUCTURES AND DEVICES

by

Farzaneh Abolmaali

A dissertation submitted to the faculty of
The University of North Carolina at Charlotte
in partial fulfillment of the requirements
for the degree of Doctor of Education in
Your Major Here

Charlotte

2018

Approved by:

____
Dr. Vasily N. Astratov

____
Dr. Glenn Boreman

____
Dr. Michael A. Fiddy

____
Dr. Ishwar Aggarwal

____
Dr. Mikhail Klibanov

ABSTRACT

FARZANEH ABOLMAALI. Focusing, imaging and resonance properties of microphotonics structures and devices. (Under the direction of DR. VASILY N. ASTRATOV)

Structures and devices built using microspherical building blocks attract significant attention in recent years due to an extraordinary high-quality factor ($Q>10^6$) of whispering gallery modes in dielectric microspheres and due to their ability to tightly focus light – so-called "photonic nanojets." In this Ph.D. theses work, we explore these properties in much more sophisticated structures where the microspheres are brought together to form so-called "photonic molecules" and 2-D arrays, where the individual resonant modes are strongly coupled forming optical supermodes with novel properties.

Chapters 2 and 3 are devoted to resonant coupling properties of such photonic molecules and sensor devices. Through finite difference time domain modeling, we introduce novel properties of such structures such as spectral signatures of photonic molecules. We show that the spectral signatures are determined by the number and configuration of constituting photonic atoms. We study spectral and spatial properties of the optical supermodes in different molecules. We also demonstrate how the simplest bi-atomic molecules can be used for achieving routing and

switching functionality in 4-port structures where such molecules are coupled to stripe waveguides.

Chapter 4 is devoted to application of photonic nanojets for enhancing the collection of light and angle-of-view (AOV) in midwives-infrared focal plane arrays. The problem in this area is related to the thermal noise in uncooled cameras. We show that we can tackle this problem by designing devices integrated with microspheres where the size of the pixels can be significantly reduced to decrease the noise, still keeping high photon collection efficiency and large AOV, thus allowing increasing the operation temperature.

Chapter 5 is devoted to application of microspheres for superresolution imaging. The problem in this area is related to an intriguing role which nanoplasmonic plays in achieving optical superresolution properties. By performing extensive comparative nanoscale imaging of fluorescent nanospheres through silica microspheres (index n=1.46), we experimentally demonstrate an important role which localized surface plasmon resonances in different metals such as Au and Al play in superresolution properties of such devices. We demonstrate that the virtual imaging of fluorescent nanospheres is possible with λ/6 resolution, if the size of features and periods of nanoplasmonic arrays is sufficiently small.

DEDICATION

I dedicate this dissertation to my parents Sharifeh and Hassan for their endless support,

encouragements and persistent love.

ACKNOWLEDGEMENTS

It gives me great pleasure in acknowledging the support and encouragement of my professor Vasily N. Astratov for mentoring me throughout the period of my Ph.D. studies. Without his support and mentorship, the completion of this dissertation would not have been possible. His scientific intuition and insights have always been very helpful. In addition to the scientific side, he has also provided me with invaluable help in carefully managing research projects, constructive criticisms on my presentations, papers, and dissertation. I have truly learned a lot during my thesis, which go beyond science itself, and thank professor Astratov for this.

I want to especially thank the other members of the committee, Profs. Glenn Boreman, Ishwar Aggarwal, Michael A. Fiddy, and Mikhail Klibanov for their valuable comments, suggestions and guidance and supports for the completion of this dissertation.

During my graduate studies I have enjoyed productive interactions and discussions with my fellow Mesophotonics Laboratory members, Dr. Yangcheng Li, Dr. Kenneth W. Allen, Navid Farahi, and Aaron Brettin over a broad range of research projects, which have led to great collaboration works.

I am thankful to Scott Williams, Dr. Lou Deguzman, and Dr. Robert Hudgins for their help of operating equipment in the Optoelectronics Center at UNCC. Also, I would like to thank Mark Clayton and Elyse Poston for assisting me throughout many administrative issues.

I was supported by the GASP tuition award from UNCC Graduate School throughout my graduate studies. I am thankful for the teaching assistantship provided by the Department of Physics and Optical Sciences. My research assistantship in Prof. Vasily N. Astratov's Mesophotonics Laboratory was supported through grants from Army Research Office and National Science Foundation.

I am very thankful to Dr. Nicholaos I. Limberopoulos, Dr. Augustine M. Urbas, for the stimulating interactions I experienced during my PhD study. At last, I wish to express my deep gratitude to my parents for their endless love and support and to my brother for his encouraging me with their best wishes throughout my education.

TABLE OF CONTENTS

LIST OF FIGURES

LIST OF ABBREVIATIONS

2-D	two-dimensional
3-D	three-dimensional
~	approximately
≈	approximately equal to
α	attenuation coefficient
a	radius
AOV	angle-of-view
Au	gold
Au	arbitrary units
BaTiO3	barium titanate
dB	decibel
°C	degrees Celsius
D	diameter
η	efficiency parameter
Ei	incident electric field
ε	permittivity
FDTD	finite-difference time-domain
FEM	finite element method
FPA	focal plane array

FWHM	full width-half maximum
FM	fundamental mode
g	gap
HF	hydrofluoric acid
IPA	isopropyl alcohol
IR	infrared
λ	wavelength
l	angular mode number
μ	permeability
μ-	micro- (10^{-6})
f-	femto- (10^{-15})
m	azimuthal mode number
m	meter
m-	milli- (10^{-3})
MCW	microsphere-chain waveguide
MWIR	mid-wave infrared
NCW	nanosphere-chain waveguide
NIM	nanojet-induced mode
NSOM	near-field scanning optical microscope
n	index of refraction
n-	nano- (10^{-9})
NA	numerical aperture

PDMS	polydimethylsiloxane
PFM	periodically-focused mode
PM	photonic molecule
PML	perfectly matched layer
PSF	point spread function
q	radial mode number
Q	quality factor
R	radius of curvature
r	radius of sphere
SEM	scanning electron microscope
TE	transverse electric
TM	transverse magnetic
3-D	three dimensional
WGM	whispering-gallery mode
X	size parameter

CHAPTER 1: INTRODUCTION

1.1: Outline and Overview of the Dissertation

Mother Nature favors spherical shape in a sense that dielectric microspheres can be fabricated by many completely different technologies with an extremely high surface quality. In its turn, high surface quality is very important for realizing the optical properties of microspheres in agreement with theories based on a model of perfect spheres. These models include Mie theory [1], whispering gallery mode theory [1], and the theory of focusing properties of microspheres termed "photonic nanojets"[2].

In this dissertation, we consider the optical properties of more complicated structures and devices where the microspheres are combined to form clusters, photonics molecules, and 2-D arrays. The optical properties of such structures and devices are complicated compared to their single photonic atom counterparts. We show that they give rise to spectral fingerprints and supermodes in photonic molecules, photonic nanojet-induced modes in chains of spheres, and unusual superresolution imaging properties of single and multiple spheres. What is even more important, all these properties are highly desirable for developing novel devices. These include novel sensors of nanoparticles, near-IR focal plane arrays, and devices for superresolution imaging.

The first task of this PhD theses work was to understand the basic physics of formation of coupled-cavity spectra and supermodes in photonic molecules and arrays of microspheres. The second task was related to use of arrays of microspheres for increasing the sensitivity, angle-of-view, and, potentially, operating temperature of IR imaging devices. The third and final task is related to studies the mechanisms of superresolution imaging by dielectric microspheres aimed at near field optical coupling mechanisms between the nanoscale objects and microspheres These studied are also aimed at understanding fundamental role which nanoplasmonic structured illumination plays in increasing the resolution of these systems

Chapter 1 is dedicated to overview the relevant literature and important articles existing in the field of study. The sub-sections can be considered as introductions to corresponding Chapters 2-5.

Chapter 2 is devoted to photonic molecules and sensor applications of circular resonators. Photonics molecules were a subject of continuous interest for the last two decades. One of the main problems in this field is related to a basic question how to make microresonators with the identical position of their WGM resonant peaks required for their efficient coupling. If WGM resonances are misaligned in the individual photonic atoms, their resonances are spectrally detuned, and their coupling and hybridization are inefficient.

On the other hand, aligning extremely narrow WGM resonances in individual microspheres represents a challenging problem. At the same time, coupled cavity structures can be fabricated without using microspheres by standard in-plane technologies, but these studies revealed the same problem related to inevitable size and shape variations of individual microdisks, rings, and photonic crystal cavities with corresponding misalignment of their resonances. Due to such difficulties, just the simple cases of single or double micro resonators, along with the concept of bonding and antibonding coupled modes were carefully studied. In this theses research proposal, we study the more complicated photonic molecules as well as coupled mode hybridization in such structures. A separate subject within Chapter 2 is represented by sensor applications of WGM resonators. By using numerical modeling, we demonstrate advantages of using coupled resonators for building sensors of nanoparticles deposited at the sidewall surfaces of such structures.

Chapter 3 is devoted to the optical transport properties of coupled WGM microresonators. We want to engineer photonics molecules in order to give them some advance functionality such as optical routing, wavelength demultiplexing, and unidirectional optical transport properties which can be very useful for developing chip-scale telecom and sensor devices. The ports in such structures can be connected in narrow spectral ranges and in only one direction or in both directions. This part of our work is closely related to such topics as optical nonreciprocity in photonic microstructures which attracted a lot of attention in photonics community in recent years. We develop an original approach to these problems based on designing the structures which comprise optical asymmetry and losses. This combination of properties is responsible for the spectrally dependent optical routing of electro-magnetic pulses in such structures.

Chapter 4 is about designing mid wave-IR (MWIR) focal plane arrays (FPAs) with advanced functionality. As it mentioned above, dielectric microspherical structures have also the ability to produce extraordinarily tightly focused beams termed “photonic nanojet”. Using this unique property of microspherical structures opens a promising way to increase the efficiency of MWIR-FPAs. A natural way of increasing the resolution, decreasing the thermal noise, and, potentially, increasing the operation temperature of MWIR imagers is connected with the reduction of the diameter (d) of individual photodetector pixels. Since the microspherical lenses are able to produce such tightly focused beam, they can allow photodetector pixel’s reduction. In our previous work, we suggested using “photonic jets” produced by dielectric microsphere, to enhance the sensitivity of FPAs, and in this thesis work we plan to optimize our designs for achieving maximal angle of the views (AOVs) for spheres with different diameters, as well as various indices of refraction. It should be noted that the standard solution of the light collection efficiency problem is offered by the commercial microlens arrays. This solution, however, comes at a price of very narrow AOV~1-2° of the resulting mid-IR imaging system. We show that the microspheres allow combining high light collection efficiencies with very large AOVs which is very attractive for developing next generation of FPAs.

Chapter 5 is devoted to study of the nanoplasmonic contributions to the resolution of nanoscale structures in microspherical nanoscopy. The research included in this Chapter continues super-resolution studies previously performed in Prof. Astratov's lab in the context of using contact microspheres. Despite all the success with developing super-resolution imaging techniques, the Abbe limit poses a severe fundamental restriction on the resolution of far-field imaging systems based on diffraction of light. Use of contact microspheres allows to pick the objects' near-fields and to project them in the far-fields. The microsphere plays a role of dielectric lens and, simultaneously, an antenna which creates a virtual image located at larger focusing depth below the sample surface. The mechanisms of super-resolution by microspheres are debated in the literature, but the essential component is connected with a combined effect of collection of the optical near-fields and magnification of the virtual image created with some contribution of these optical near-fields. The factor which was less studied is connected with a role of structured illumination of nanoscale objects by nanoplasmonic arrays fabricated on a substrate. By looking into spectral and spatial characteristics of such coupling between fluorescent dielectric nanospheres and nanoscale metallic arrays we come to the conclusion that localized surface plasmon resonances play an essential role in mechanisms of superresolution imaging properties of such structures. The results for nanoplasmonic enhancement are illustrated by finite difference time domain modeling.

In the following sections, we review resonant mechanisms of light interaction with dielectric spheres based on whispering gallery modes (WGMs) excitation in the microspherical cavities. We also review the non-resonant mechanisms of light interaction with dielectric spheres. We will discuss the basic physics of resonant and non-resonant interaction mechanism.

1.2. Resonant Properties of Dielectric Spherical Microcavities

1.2.1. Whispering Gallery Modes in Spherical Microcavities

Optical resonators are able to confine significant electromagnetic power in small volume and for extended periods of time. These properties make them fundamental in any laser device as well as nonlinear optics applications, optical and RF communications, quantum optics [3], optical signal processing, and sensing [4, 5]. A particular class of optical resonators is constituted by structures with spherical symmetry, where the light waves are almost perfectly guided round by total internal reflection and focused by the surface itself. The specific resonances (or modes) of a wave field that are confined inside these spherically symmetric resonators (Fig. 1.1) so-called whispering gallery modes (WGMs). The term of whispering gallery modes first introduced by John William Strutt (Lord Rayleigh) for the traveling sound rays making up chords of the circular gallery due to the refocusing effect of the curved surface [6].

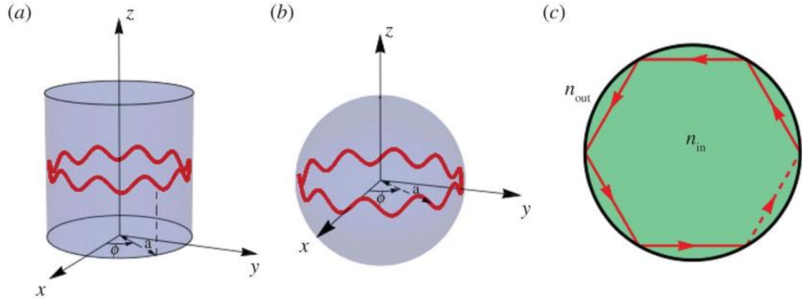

Figure1.1: (a,b) Schematic illustration of a cylindrical and a spherical dielectric microcavity. (c) Top view of the microresonators. Resonances occur when the optical path length equals an integer number of the wavelength inside the cavity [7].

The initial study of the spherical microparticle in a properly shaped object made of a dielectric material was published by Richtmyer in 1939 [8] showing a spherical microresonator could sustain high-resonance modes. Due to minimal reflection losses and to potentially very low material absorption, these modes can also reach remarkably high-quality factors. Later in 1961, Garrett *et al.*, noticed the application of spherical resonators as laser resonators [9], detection of biomedical molecules and viruses [10-14], detection of nanoparticles [15, 16], environmental medium sensors [17-20], temperature sensors [21], force sensors [22, 23], rotation sensing (Application of optical whispering gallery mode resonators for rotation sensing) and micro-lasers [24-28] are examples of other applications for microspherical resonators. There is a variety of geometries for WGM resonators including cylindrical optical fibers [29], microspheres [30, 31], fiber coils [32], microdisks [32-34], microtoroids [35-38] (Fig. 1.2), photonic crystal cavities [10, 39, 40], microcapillaries [24], and some exotic structures, such as bottle [41, 42] and bubble microresonators (Fig. 1.3) [43, 44].

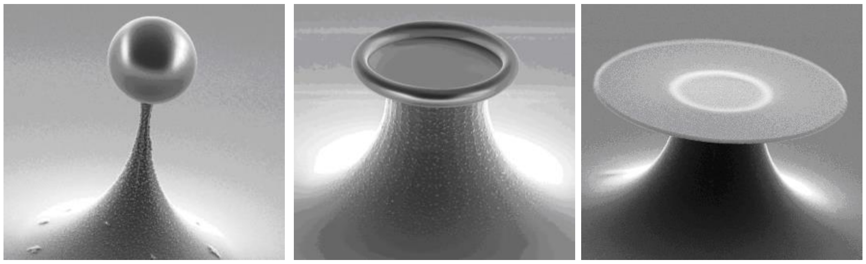

Figure1.2 : SEM micrographs of a silica microdisk on a Si-chip with a radius of 40 µm, a microtoroid with a radius of 25 µm, and a silica microsphere with a radius of 11.5 µm [45].

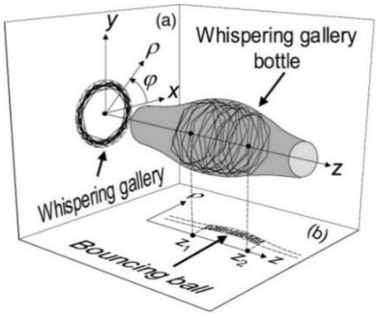

Figure1.3: Illustration of the WGB bottles: (a) projection of the WGB on plane (ρ,φ), (b) projection of the WGB on the plane (z,ρ) [41].

In this dissertation, we mainly consider WGMs in microspheres due to easier manipulation, commercial availability [46, 47], and their higher Q-factor [14, 48, 49]. The confined electromagnetic waves inside the dielectric sphere, correspond to waves circling around the cavity, supported by continuous total internal reflection off the sphere surface, that meet the resonance condition (after one roundtrip ($\sim 2\pi R$) they return to the same point with the same phase and hence interfere constructively with themselves, forming standing waves [50]. The constrictive condition can be expressed as $\approx l(\lambda_0/n)$ where λ_0/n is the wavelength in the medium with refractive index n [51].

Microsphere resonators are usually fabricated by means of surface tension and can be made of materials in liquid, amorphous and crystalline forms. The earliest demonstrated optical microresonator and also the simplest, is a micron-sized liquid droplet with a near perfect spherical surface due to surface tension [52]. The solid-state microsphere resonators are other type of microsphere which made from fused silica (SiO2)[52]. In this case the tip of a silica optical fiber is heated by an electric arc or a flame and forms a sphere to retain a minimum its surface energy. The melted silica solidifies in a microsphere shape as soon as the heat is removed. The radius of sphere can be adjusted by the size of the fiber tip. One more technology is represented by the cluster-aggregation reactions in the solutions with one of the examples represented by small, micron-scale silicon microspheres or synthetic opals.

The other type of circular resonator such as disk, circuit and ring resonators can be fabricated in three basic processes: deep ultraviolet (DUV) lithography, electron beam lithography (EBL) with higher feature resolution for closely packed structures than DUV lithography, however is much slower/has lower throughput than DUV lithography, and nanoimprinting lithography (NIL) which has high throughput as well as high feature resolution [52].

The propagation of electromagnetic eigenmodes inside a dielectric sphere with radius R placed in vacuum can be defined in spherical coordinates (r, ϑ, φ) [1, 53].

$$\Psi_{n,l,m}(r,\vartheta,\varphi) = \begin{cases} AP_l^m(cos\vartheta)e^{im\varphi}j_l(k_{1,\zeta}r) & ; \quad r < R \\ BP_l^m(cos\vartheta)e^{im\varphi}h_l(k_{0,\zeta}r) & ; \quad r > R \end{cases} ; \tag{1.1}$$

$$k_{1,\zeta} = k_{0,\zeta}\sqrt{\varepsilon\mu} \ ; \ k_{0,\zeta} = \frac{\omega_\zeta}{c_0} \tag{1.2}$$

Where P_l^m is Legendre polynomials, j_l spherical Bessel, and h_l spherical Hankel functions. ω_ζ is the angular frequency of the resonance, c_0 is the speed of light in vacuum. ε and μ are the relative electric and magnetic permittivity of the sphere respectively. Here, n, l and m uniquely determine the radial, polar and azimuthal quantum mode numbers respectively [54]. n equals the number of WGM intensity maxima along the radial direction inside the sphere, l equals the number of wavelengths that can fit into the optical length of the equator. The azimuthal (m) mode number $-l \leq m \leq l$

determines the spread of the modes away from the equator (fundamental mode with m=l corresponding to propagation in the equatorial plane) towards the poles. Using appropriate boundary conditions at the sphere's surface we can calculate ratio A/B and $k_{0,\zeta}$ as constant numbers. In a degenerate case of perfectly spherical shape, the resonant frequency depends only on the indices n and l, but not on m, hence the degeneracy of the modes is $2l+1$ [53]. Also, $l-m+1$ equals the number of field maxima in the polar direction (perpendicular to the equatorial plane). For $n=1$ more or less there is no fluctuations inside the sphere, thus the modes with lower n are better confined in the sphere (higher Q-factor) and leak out more slowly than those with larger n [55].

For small indices l the mode fills almost the whole volume of the microsphere, while for large indices l (bigger than 100) the modes are highly localized close to the surface of the microsphere (Fig. 1.4) [53].

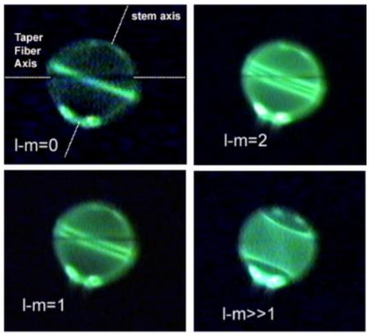

Figure1.4: Formation of whispering-gallery modes visible by implanted Er^{3+} ions via up-conversion luminescence in a coupled system of microsphere and tapered optical fiber. The number field of maxima in the polar direction is given by $l-m+1$ [54].

For $m = l$ we also get no oscillations of amplitude in the polar direction, and since $P_l^l(cos\vartheta) \propto sin^l\vartheta$, such a mode is, for large indices l, highly localized also in the polar direction. These properties are very similar to what described by Lord Rayleigh to his whispering gallery waves and that is why we call modes with $n = 1$ and $m = l \gg 1$ fundamental whispering gallery modes of the sphere [53].

In practice, by small deformations of the microspheres from the spherical shape [56]or by any perturbation at the surface of the sphere the degeneracy of the azimuthal number, m, can be removed. As shown in Fig. 1.5(a) the fundamental WGMs with $m = l$ are defined ((69) parallel to the substrate in the equatorial plane of the sphere. The highest Q-factors can be expected for such fundamental modes, due to the fact they are separated from the substrate by the radius of the sphere as illustrated in Fig. 1.6(b). On the other hand, the modes with $m << l$ are damped, since the spatial mode distribution approaching to the high refractive index substrate (with maximum intensity) as shown in 1.6(c). A typical fluorescence spectrum of a single dye-doped polystyrene (n=1.59) microsphere with diameter of D=5 μm on a glass substrate is shown in Fig. 1.5(d) [57]. The WGM peaks with orthogonal polarizations are characterized by TE_l^n and TM_l^n respectively.

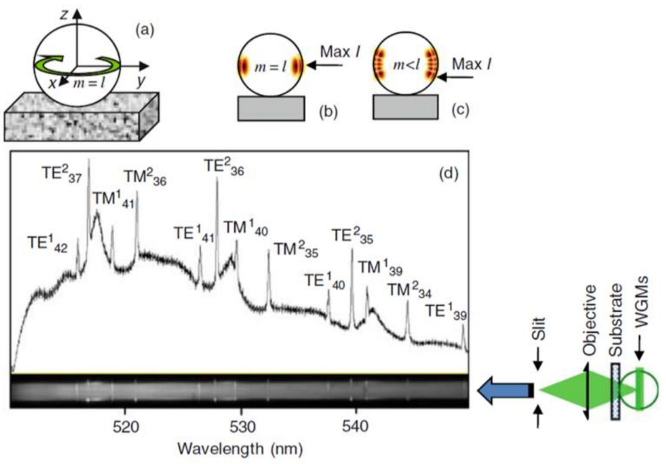

Figure1. 5: (a-c) Schematic illustration of WG modes distribution with different m, for a single microsphere positioned on a substrate. (d) Fluorescence spectral image and emission spectrum of a single green fluorescent D=5.0 µm sphere with TE_l^n and TM_l^n WGM peaks measured through the transparent substrate [57, 58].

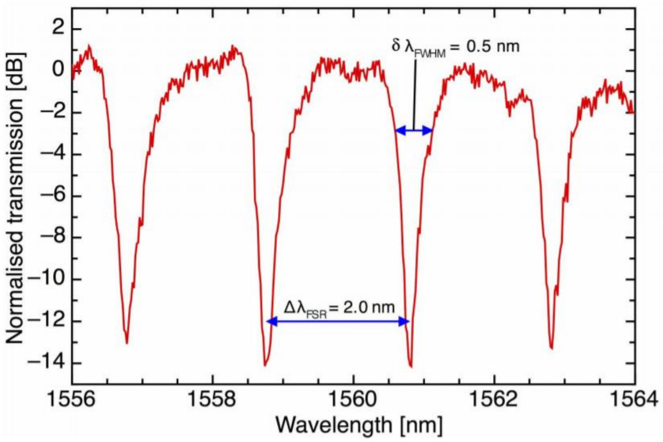

Figure1. 6: Measured wave transmission spectrum of the bus waveguide coupled to a microring resonator. The measured free spectral range of the microresonator is $\Delta\lambda_{FSR} = 2.0 \pm 0.01$ nm. The spectral width of the resonances (full-width at half-minimum of the dip) was $\delta\lambda_{FWHM} = 0.5 \pm 0.05$ nm [59].

In general, angular modes are separated by the free spectral range (FSR) for typical resonators (Fig. 1.6), $\Delta\lambda_{FSR} \approx \lambda^2/(2\pi R)n_g$. The calculated group effective index $n_g = n_{eff} - \lambda(\delta n_{eff}/\delta\lambda)$ includes both the material dispersion and the modal dispersion of the effective index of the guided mode n_{eff}. The modal dispersion mostly becomes important in the case of single-mode waveguides [60].

The approximated positions of WGM resonance modes in a dissipated system where the electromagnetic fields leak from the optical cavity can be derived from Maxwell's equations solved in the spherical coordinates by using the Mie scattering. In this approximation resonators are considered with diameters large relative to λ, therefore the radiative leakage of the energy is small, and the radiative part outside the sphere as negligible; thus, the resonance condition expressed can be written as

$$P\frac{J_\nu'(Nx)}{J_\nu(Nx)} = \frac{N_\nu'}{N_\nu} \tag{1.3}$$

Where parameter $x = 2\pi a/\lambda$, J and N are Bessel and Neumann functions respectively, and $\nu = l + 1/2$ translating the spherical Bessel and Neumann functions to their cylindrical counterparts [56, 61, 62]. The Bessel and Neumann functions as well as their derivatives in eq. (1) can be expressed as asymptotic series in powers of v−1/3 and Airy functions which allows the resonance positions to be obtained:

$$Nx_{l,n}^{P} = \nu + a_{1n}\nu^{1/3} + a_0\nu^0 + a_{-1n}\nu^{-1/3} + \cdots \tag{1.4}$$

Where $a_{1n} = 2^{-1/3}\alpha_n$, $a_0 = -P/\sqrt{N^2-1}$, $a_{-1n} = \frac{3}{10}2^{-2/3}\alpha_n$, and α_n are roots of the Airy function $A_i(z)$ and associated with the radial order n. here the Free Spectral Range (FSR) corresponds to the spacing between two modes with the same polarization and with the same n of the circular resonator can be defined as $\Delta\nu_{n,l}^{TE,TM} \approx \frac{c}{2\pi Na}\frac{\sqrt{N^2-1}}{N}$. The spacing between two adjacent modes labeled as TE and TM and only differs by one unit of their quantum number l [61].

Fig. 1.7 shows a typical fluorescence (FL) emission spectrum with WGM peaks along with the spectral image of a 5 m polystyrene (index of 1.59) microsphere on a glass substrate. The WGM peaks with orthogonal polarizations are labeled TE_l^n and TM_l^n respectively. The measured Q-factor for the first order modes (n=1) in Fig. 1.7 equals Q=4×10^3, which is well below the theoretical limit (Q>10^5) calculated for perfect 5 μm sphere [58].

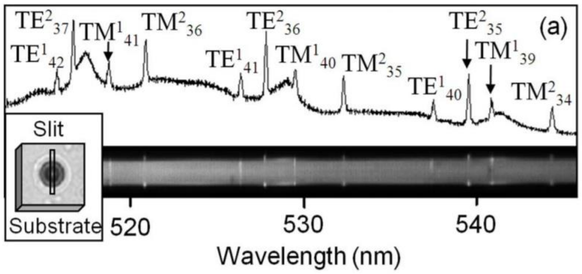

Figure1. 7: FL spectrum of a single dye-doped 5 m polystyrene (index of 1.59) sphere on a glass substrate [58].

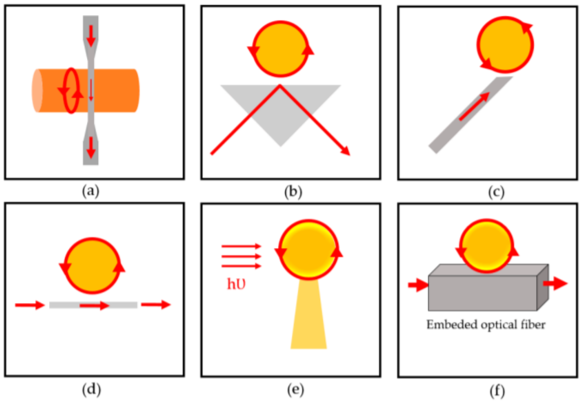

Figure1. 8: Various types of optical coupling. (a) Tapered; (b) prism; (c) angled fiber; (d) planar waveguide side; (e) free-space; (f) polished half-block coupler [63].

1.2.2: Overview of Coupling Methods and Critical Coupling

The prerequisite for the practical application of WGM resonators asks for high-Q (WGMs), with negligible parasitic loss. Therefore, achieving a controllable and efficient coupling of light in and out of a WGM resonator is essential. WGM optical coupling using Free-space excitation is not efficient due to different phase velocities of light in air and dielectric microcavity. There are various techniques for coupling the light into circular resonator which all rely on energy exchange between a WGM and the evanescent part of guided modes or total internal reflection waves. The earliest evanescent coupling method used to couple light in WGM microresonators works based on prism frustrated total internal reflection [64-66] where the beam evanescent wave in the prism overlaps with the evanescent field of a WGM resonator with coupling efficiency of 80% [65, 67, 68]. A variation on the prism coupler is an angle polished optical fiber coupler, which provides better compatibility with fiber optics but limited coupling efficiency of 60% [65, 69]. Other examples of coupling methods for illuminating resonator structures are planar waveguide side coupling [68, 70, 71], and polished half-block coupler as schematized in Fig. 1.8 [72].

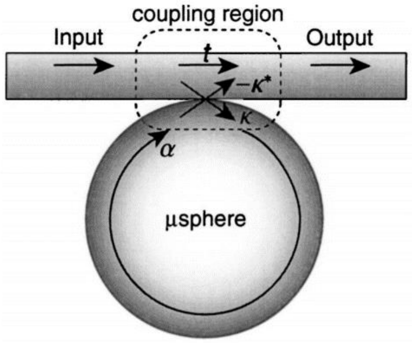

Figure1. 9: Illustration of an ideal coupled circular resonator with tapered fiber. t is the transmission coefficient through the coupler. κ is the mode coupling amplitude and can be expressed by $\kappa = i\sqrt{1-t^2}$, and α is the transmission coefficient for the E-field on a round trip in the circular resonator [73].

The most common method with high coupling efficiency of 99.8% being tapered fibers with micrometer or smaller diameter to critically couple high-Q-factor WGM resonators [74]. There are several advantages using a fiber taper waveguide (4) including simple tapering? (I would use “focusing” with the lens) and alignment of the input beam, as well as collection of the output beam when the tapered fiber placed alongside a resonator. Moreover, in critical coupling condition, it can very efficiently select the fundamental modes by filtering out all other waveguide modes at both the input and the output. The critical coupling refers to the condition in which the internal loss of the resonator is equal to the coupling loss of the waveguide for a matched resonator waveguide system, at which point the resulting transmission at the output of the waveguide goes to zero on resonance [75].

For ideal mode matching in a coupler, the waveguide-microsphere system can be expressed by a single coupling parameter t and a resonator round-trip factor α as it illustrated in Fig. 1.9. The exchange of optical power for unidirectional lossless coupling between a ring resonator and a waveguide can be explained by simple analysis of the coupling [73]:

$$1 - T = \frac{C}{1 + f\, sin^2\left(\pi \frac{\nu}{\Delta\nu_{FSR}}\right)} \tag{1.5}$$

$$f \equiv \frac{4\alpha t}{(1-\alpha t)^2} \tag{1.6}$$

$$C \equiv 1 - \left(\frac{t-\alpha}{1-\alpha t}\right)^2 \tag{1.7}$$

Where C is the resonator coupling parameter, f is the coefficient of finesse, $\Delta\nu_{FSR}$ is the resonator free-spectral range. The critical coupling (complete power transfer and dissipation of waveguide power) happens when $C = 1$. In this condition, for a properly designed taper-microsphere system it is possible to nearly extinct the power transmission at the output of the waveguide due to the high degree of filtering performed by the taper fiber. This contrasts with a prism coupler where very limited mode filtering is performed and most of the light scattered by the circular resonator is collected. Therefore, in this case dissipation of power transmission at the output of the waveguide would be very limited.

1.2.3: WGMs Coupling in Photonic Molecules

The term photonic atom has been brought up by Arnold et al. [76] for a phenomenon involving electromagnetically-interacting optical circular microresonators. The properties of confined photon states in optical microresonators are very analogous to the confined electron states in atoms [77]. Based on this analogy, optical circular microresonators can be called "photonic atoms". Considering this terminology, the individual photonic atom can be used as a building block to form a cluster of several mutually-coupled atoms referred to as photonic molecules [78]. In photonic molecule structures, the optical modes of individual atoms interact and give rise to a spectrum of hybridized super-modes of photonic molecules [78]. Photonic molecules have emerged as structures with promising properties for investigation of fundamental science as well as for applications such as biochemical sensing and information processing.

1.2.4. Optical Coupling in Double-Resonator Photonic Molecule

The simplest structure of photonic molecules is the double-microresonator. Electromagnetic coupling between WGMs microdisk, microring, and microsphere resonators (19, 49–57) results in the splitting of individual resonator modes into shorter wavelength anti-bonding (blue-shifted) and longer wavelength bonding (red-shifted) super-modes. The spatial distributions of bonding and antibonding modes are shown on the right of Fig. 1.10. The amount of the shift in the resonant frequency varies based on the strength of the coupling between individual photonics atoms. Moreover, the values of Q-factors for bonding and antibonding super modes (referred to as 'loss splitting' (16)) depend on the change in the inter-cavity coupling efficiency. These two effects are shown in Figs. 1.10 (a, b) where two microdisk resonators coupled via an airgap.

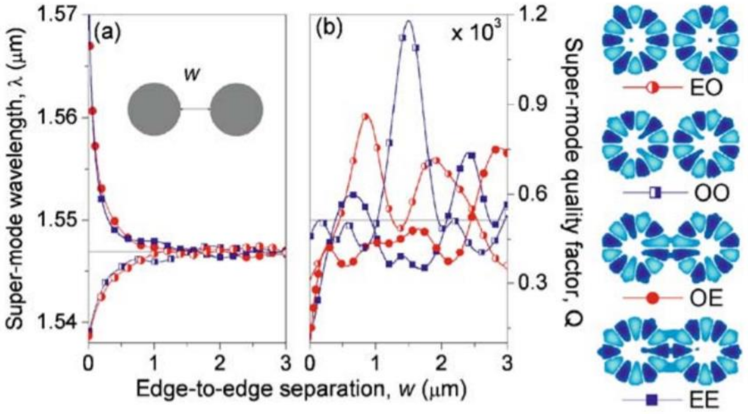

Figure 1.10: WG modes splitting in a double-microdisk photonic molecule (with radius of 0.9 µm, effective refractive index *n*= 2.63), and TE polarization). (a) bonding and antibonding super modes wavelengths and (b) quality factors as a function of the airgap size between microdisks. The inset illustrates the spatial distribution of magnetic field for bonding and antibonding super modes [79].

To study the case of identical two microsphere in contact, another experiment was performed by H. Miyazaki and Y. Jimba [79] to measure an energy spectrum for normal incidence of light. Fig. 1.11 shows the spectrum which normalized by the vacuum electromagnetic energy of the bi-sphere

$U_0^{bi-sphere} = \frac{2}{3}a^3$ where a is the radius of microspheres. To specify the characteristic feature of the spectrum two general rules should be considered: (1) the interaction between microspheres is limited only between modes of the same azimuthal mode number m, and (2) no degeneracy is removed between m and $-m$ which means the total number of peaks for a certain l mode is at most $2\,(l+1)$ in the range $0 \ll |m| \ll l$ [79]. These peaks are recognized as bonding and antibonding modes.

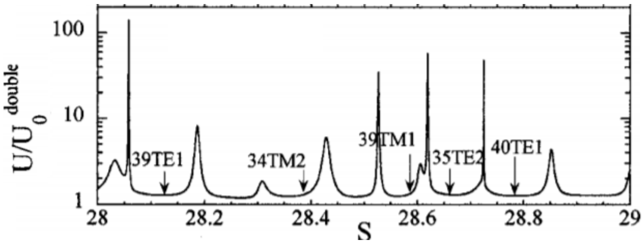

Figure 1.11: Internal energy U vs size parameter $S = k_0 a$, The Mie resonance positions of a single sphere are indicated by the arrows [79].

As an example of mode splitting, in Fig. 1.11, for the cases of TE_{39}^{1} and TE_{40}^{1}, supermodes are almost equally split compare to resonance position of single microsphere (uncoupled mode), however the upper peak is broader than the lower one. In contrast, mode TM_{39}^{1} shows the asymmetric split with almost the same width for bonding and antibonding modes. In this case, lower peak of mode TE_{35}^{2} appears as a small peak just below the upper peak of mode TM_{39}^{1}. In fact, the asymmetric split of mode TM_{39}^{1} in some way contributes with TE_{35}^{2} which can be explained based on the double-mode tight-binding model [79]. Also it can be observed that all the peaks for supermodes are much broadened compared with the uncoupled mode peaks of the individual microsphere [80] due to the interaction with more dissipative modes of lower *l* in Fig. 1.11 [79].

1.2.5: WGMs Coupling Properties for Linear Chains of Microresonators

For a linear chain of identical microresonators where N photonic atoms are side-couple to form a photonic molecule, the optical spectrum has multiple super-mode peaks. In this situation where microresonators are placed close to each other, photons in one resonator can tunnel to the neighbor resonator due to the overlap of the adjacent evanescent cavity modes. The number of coupled modes tends to be equal to the number of spheres in the chain and to the degeneracy number of the modes in the stand-along atom. This situation is shown experimentally by Kuwata-Gonokami et al. [81], which used dye-doped Polystyrene spheres of 4.2 µm in diameter with refractive index of 1.59. Fig. 1.12(a) illustrate the typical spectra of spheres with 1% size variation. The select spheres were positioned in a linear chain structure on a silicon V groove substrate to ensure the straightness and reproducibility of the microsphere chain, as seen in Fig. 1.12. It is known [57, 58, 82] that only WGMs with the intensity maxima separated from the substrate have sufficiently high Q-factors. Therefor the gap shown in the inset between the spheres and the V groove favors WG modes in a plane perpendicular to the substrate [81].

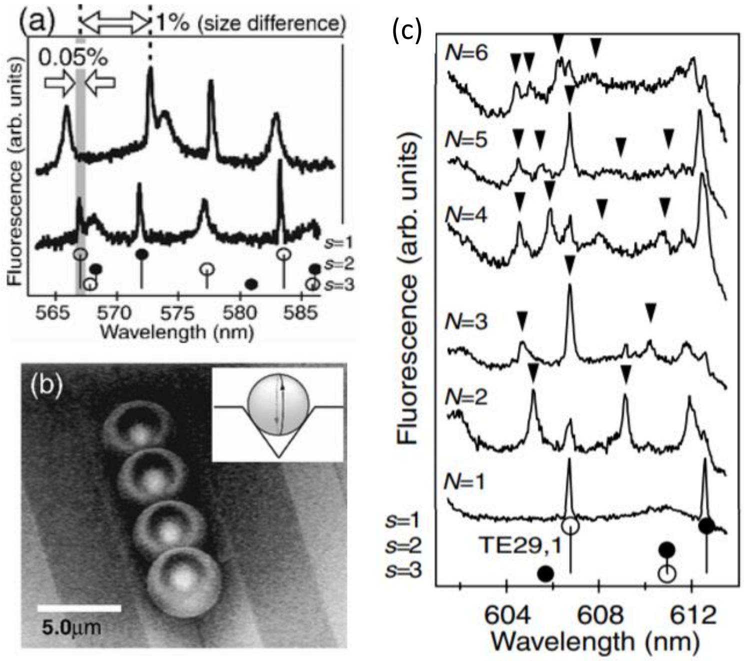

Figure 1.12: Fluorescence spectra of spheres with 1%- size variation. (b) Scanning electron microscope image of four microspheres with diameter of 5.1 μm arranged linearly on a silicon V groove. The inset shows the gap between groove and spheres which supports WGM. (c) Fluorescence spectra from a microsphere array structure consisting of one to six spheres.

Figure 1.12(c) illustrates the fluorescence transmission spectra for a single microsphere as well as size-matched two to six-sphere chains in the vicinity of TE_1^{29} resonance. The positions of coupled WGMs in each sphere chains were shown by arrows. It can be seen that the number of coupled modes is proportional to the number of coupled resonators. Although in experimental condition some of the coupled modes are not visible because of low signal to noise ratios. A peak at the resonance of uncoupled mode from single sphere was observed in all spectra due to large NA of the collecting fiber.

1.3: Resonant Optical Routing and Unidirectional Transmission in Photonic Molecules

In this paragraph, we change our focus from the optical coupling effects in microcavities to a broader understanding of the directionality of light transport in such structures and to the role which structural asymmetry and losses play in such properties.

1.3.1: Introduction to Non-Reciprocity

As it was mentioned above, the quest for on-chip optical isolators and has recently leaded to many new isolator structures and nonreciprocal/unidirectional systems. On the practical level, nonreciprocal devices are not only critical for signal processing applications but also needed for simplifying the structure of photonic networks. In this section, the essential characteristics of an isolator, and the requirement of nonreciprocity is reviewed.

1.3.2: Device Solutions for Unidirectionality

As it mentioned, an asymmetric scattering matrix, which breaks the Lorentz reciprocity is required for isolator devices. In the conventional solutions using magneto optical effects (Faraday rotation), could provide asymmetric scattering matrix, and therefore optical nonreciprocity [83, 84]. Although these magneto-optical solutions are generally adopted in commercial optical isolators and circulators, the bulky components and external magnetic field make them difficult to integrate with on-chip and nearby devices [85, 86]. To break the reciprocity in optical systems beyond the conventional magneto-optical methods, other strategies have been recently developed to address the need of on-chip optical nonreciprocal devices, including optical nonlinearity such as electro-absorption modulation [87], cholesteric liquid crystals [88], opt mechanical cavities [89] and the opto-acoustic effect [90], interband photonic transitions [91], and PT symmetric optics [92, 93] which are briefly discussed in the following sections.

1.3.2.1: Magneto-Optical Effects

Perhaps the most common optical isolator relies on the Faraday Effect and 45° crossed polarizers [5]. Here, a magneto-optically active material gives rise to polarization rotation, which has opposite signs for backward and forward propagation (Fig.1.15).

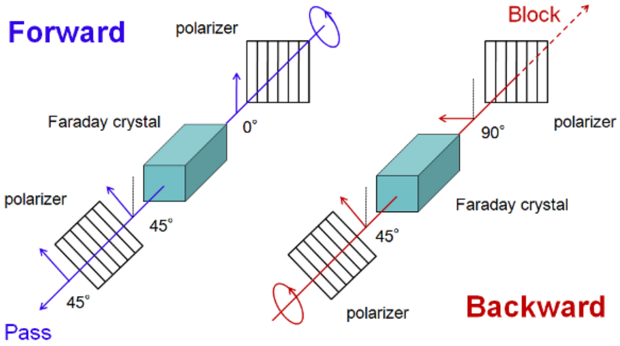

Figure 1.15: Schematic structure of ordinary optical isolator [94].

Other isolators based on magneto-optical materials usually use waveguides with different propagation constants in the forward and backward directions [94, 95], nonreciprocal propagation losses [96], and induce frequency splitting in resonators [85, 97].

Although magneto optical non-reciprocal photonic devices commonly used in optical communications, but such devices are still deficient in semiconductor integrated photonic systems [83, 98] because of some difficulties in both materials side and device design. Since nonreciprocal magneto-optical garnets has large lattice size, they show thermal mismatch with semiconductor substrates, and it makes it difficult to reach uniform integration of garnets, and it is requiring wafer bonding to combine them on a semiconductor platform. Therefore, there is no proper phase purity, high

Faraday rotation and low transmission loss [99, 100]. Also, on the device side, the length scales of integrated optical isolators start from millimeters to centimeters, so it has large foot print.

1.3.2.2: Optical Nonlinearity

Nonlinear materials are another group of materials that breaks reciprocity and can be used for isolators. For instance, isolators that uses Raman amplification [101], and stimulated Brillouin scattering [102] which have linear responses to the input power below the pump level and chirped nonlinear optical photonic crystals [103] which works only in a certain signal power range. Isolators with a time-varying refractive index are other devices in this class [104, 105].

Since longitudinally non-uniform structures of nonlinear materials have a nonreciprocal response, they can be considered as alternatives to the Faraday by using graded amplifying media or quadratic waveguides which are concentrated asymmetric along the propagation direction. By this way a high contrast optical diode can be fabricate by engineering the second-harmonic generation cascading effects in forward and backward propagation through proper modifying of the nonlinear response of a channel waveguide. Unidirectional devices based on cascaded nonlinearities usually use a well-designed quasi phase matching (QPM) grating in a recombined proton exchanged waveguide (Fig.1.16). In this structure a dephasing domain of δL is introduced at $x = L1$ inside a perfectly uniform grating of period L_0 with total length L, so the grading is perturbed by a localized “defect”. The cascading of two parametric interactions occurs in the uniform QPM segments L_1 and $L2 - L1 - \delta L$, but the defect can change the phase relationship locally between the fundamental and second harmonic waves. By suitable placement of L_1 and δL of the defect, the forward transmission can be maximized by fully restoring the fundamental power at the output via cascaded up-and-down, however the device turns as an efficient frequency doubler in the backward direction, causing negligible transmission [106].

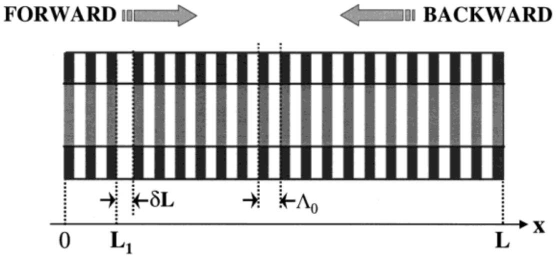

Figure 1.16: QPM grating profile used for optical diode: dark and bright sections represent positive and negative nonlinearity respectively. The arrows indicate nominal forward and backward propagation directions, respectively [106].

In addition, since the liquid crystals (LCs) among various optically nonlinear materials have orientational third-order nonlinearities which are already up to several orders of magnitude larger than Kerr electronic nonlinearities of conventional dielectrics, therefore, the efficiency of optical nonreciprocal approaches based on LCs can be enhanced in QPM structure by embedding a LC defect layer asymmetrically inside it [107].

1.3.2.3: Thermo-Optical Effect

Using high–quality factor (Q) Si microrings is another method for constructing optical nonreciprocity as a diode effect based on strong optical nonlinearity. Si microrings consists of a high-Q all pass notch filter (NF) which operates near the critical coupling regime, and an add-drop filter (ADF), with asymmetric power coupling to the bus waveguides (Fig. 1.17) [107].

To match the resonant wavelength of the notch filter with add-drop filter, the wavelength can be thermally tuned through thermo optic effect of silicon. At this resonance wavelength, light couples into the micro ring in the ADF through two different gaps, G_2 and G_3, and optical energy accumulates in the micro ring. Because of the asymmetric design, the energy enhancement factor in the ring depends on the propagation direction [107].

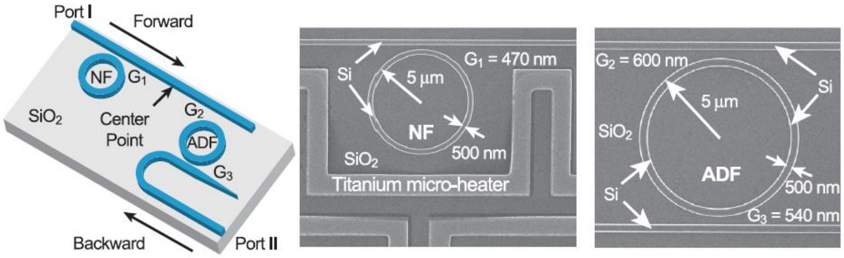

Figure 1.17: Fabricated Notch filter (NF) and add-drop filter (ADF) as two resonance-matched filters. Forward direction is defined as Input at port I and output at port II; backward direction: input at port II and output at port I [107].

Since the ring resonator has high Q factors and small radius, with high input power, the power density inside it will be considerably amplified. This induces optical nonlinearity in silicon, and a red shift in the ring's resonance. Therefore, less energy is stored in the ring during forward propagation, and the amount of resonance shift in the forward direction will be smaller than that in the backward direction. This leads to a case in which forward transmission exceeds backward transmission. The optical nonlinear effects in silicon include the Kerr effect, two-photon absorption, the free carrier effect, and the thermo-optic effect. Because of the large thermal dissipation time of the SiO_2, the thermo optic effect is dominant, and since it does not require external magnetic fields, radio-frequency modulation, or optical pumping, its functionally makes it similar to electrical diodes [107].

1.3.2.4: Parity-Time (PT) Symmetric Optics

The engineered photonic structures combining gain and loss, have received increasing attention in the optical information processing and optical communications communities recently Such systems provide new possibilities for manipulating light beyond conventional structures having only loss or only gain [108]. In fact, these compound-optical systems with gain and loss provide a powerful analogy to test theoretical proposals in quantum mechanics described by non-Hermitian parity-time (PT)-symmetry PT-symmetric optical systems are open physical systems combining balanced gain (amplification) and loss (absorption) which are reciprocative under parity (P) reflection and time reversal (T), and, therefore gain and loss are interchangeable in such systems [108]. Interestingly, the PT symmetric system under some conditions that the non-Hermitian factor crosses a critical threshold, can exhibit a phase transition from PT symmetry to broken- PT symmetry. Some phenomena like nonreciprocal light transmission in integrated photonic devices (such as on-chip optical circulators and optical isolators) can significantly benefit from crossing that "exceptional critical threshold" and using broken-PT symmetry to introduce nonreciprocity and unidirectionality into the optical system. Since such on-chip PT symmetric optical devices can be integrated with photonic circuits, consequently, they provide a viable alternative to conventional solutions using magneto optical effects (Faraday rotation) [108].

For example, in a system of two coupled micro-resonators by adding gain on the first micro-resonator (case (b) in Fig. 1.18(b)) and keeping the gain and loss ratio at a fixed value, we again monitored the spectral positions of the bonding and antibonding modes as a function of the gap (blue line in Fig. 1.18(b)) [109].

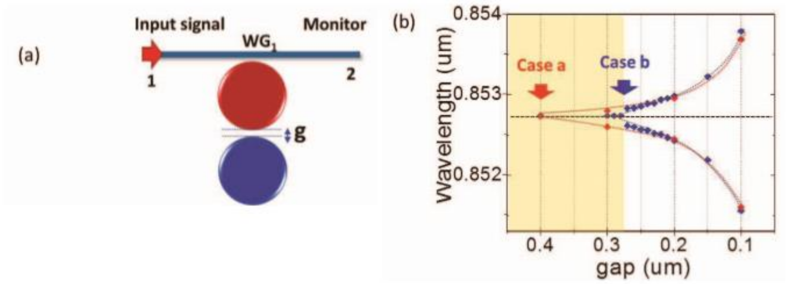

Figure 1.18: (a) System of two coupled active and passive WGM micro-resonators. (b) Mode splitting of supermodes as a function of the gap between two micro-resonators [108, 109].

Unlike case (a), the mode splitting could not be detected for a gap between the micro-resonators exceeding 275 nm. Reducing the gap, generally, increases the role played by dissipative (light scattering) processes at the wavelengths of bonding and antibonding modes. Sudden appearance of splitting at the 275 nm gap can be interpreted as a result of a phase transition in the system from broken PT symmetry to PT symmetry. For smaller gaps, the energy in the active resonator flows fast enough into the passive one and the loss in the passive resonator can be compensated, hence the gain and loss are in balance, and the system is PT symmetric. On the other hand, when the gap is larger than 275 nm and the resonators are weakly coupled, the energy only accumulates in the active resonator. The gain and loss cannot be in balance and the system is in its broken PT symmetry region. This region for broken PT symmetry can be potentially used to introduce unidirectionality and non-reciprocity into the optical system [108, 109].

By the Lorentz reciprocity theorem, any linear system described by symmetric and time-independent permittivity and permeability tensors is necessarily reciprocal. Therefore, the scattering matrix of such system will be symmetric and hence unsuitable for isolation. To introduce nonreciprocity into the system, many approaches are stablished which among them, using magneto-optics effects are most common, but the bulky components and external magnetic field make them difficult to integrate with on-chip and nearby devices. Therefore, to achieve nonreciprocity without magneto-optics, one necessarily has to rely upon either nonlinear or time-dependent effects. Based on these facts other methods such as optical nonlinearity, interband photonic transitions, Optical-thermo effect and PT symmetric optics are developed to address the need of on-chip optical nonreciprocal devices.

1.4. Non-Resonant Properties of Dielectric Spherical Microcavities

In this Section we change our focus to the optical properties of circular dielectric objects which are not directly related to their high-quality internal resonances and more related to their ability to focus light as microlenses or microlens arrays. Near-field coupling effects will still play some role, especially in imaging aspects considered later in Section 1.4.2. We start, however, from more simple focusing properties which often can be understood in a geometrical optics, especially for sufficiently large microspheres with D>>10λ, where D is the sphere diameter and λ is the wavelength of light.

1.4.1: Highly Efficient Mid IR- Focal Plane Arrays with Large Angle-of-View (AOV)

Infrared focal plane arrays (FPAs) have a dynamic journey since the primary 2-D arrays were manufactured in the late 70s. Today's fixed and portable mission necessities are motivating the development of these thermal imaging systems for a wide variety of space science, security, surveillance, military, and commercial applications. The designs of modern focal plane arrays (FPAs) used in mid-wave infrared (MWIR, λ ~3-5 μm) detection are being developed towards minimization of the pixel sizes and increasing the operational temperature. The dark current is proportional to the detector's area (A). However, in the case of illumination of FPA by quasi-plane waves, the reduction of A would also cause the reduction of the photocurrent. This means that one needs a specially designed microstructure or a "concentrator" which would allow to deliver all incident power to a photodetector mesa with reduced size and, consequently, reduced dark current. In FPAs equipped with such concentrators the operation temperature can be increased compared to similar structures with large photodetector mesas operating without concentrators. Here we review some of these photon trap structures such as photonic crystals, textured surfaces with pyramidal relief features, and curved FPAs.

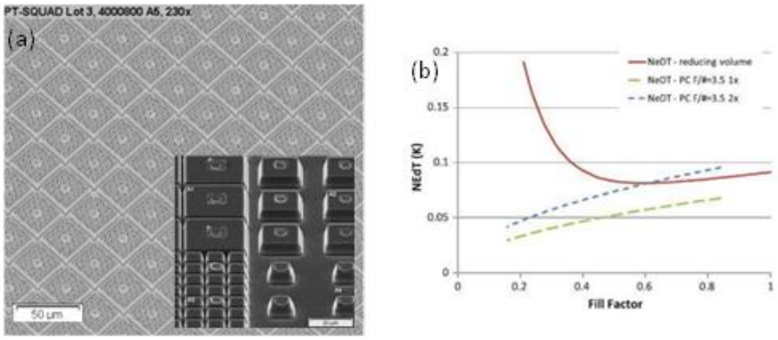

Figure 1.19: (a) 512 x 512 30 μm array of photonic crystal holes on a 5 μm pitch in a standard mesa, subset shows a corner of multiple variable unit cell regions on a 512 x 512 30 μm array. (b) NEDT for a HgCdTe detector with a 5 μm cutoff at 200 K reducing mesa approach compared with a photonic crystal approach [110].

One of the determined requirements for enhancing the performance of IR detectors is to obtain high (> 80 %) quantum efficiency over the broad 0.5 to 5.0 µm spectral range while minimizing dark current and improvement in operation temperature. The application and using photonic crystals for IR detectors first was shown by Krishna et al [111] reported that by removing material, the QE can be improved from 7% to 93%. Fig. 1.19 shows one example of photonic crystal arrays as well as the modeling result for device performance comparison for a baseline shrinking mesa and an idealized photon trap detector when the fill factor is reducing. The fill factor is calculated as the volume of material remaining divided by the volume of the unit cell. To do the comparison, the noise equivalent temperature difference (NEdT) for HgCdTe detector with 5 µm cut-off (based on a diffusion-limited detector) and photonic crystal 1x and 2x are calculated. As it can be seen in Fig. 1.19 the effect of volume reduction is to decrease NEdT for mesa until a critical point where the volume reduction removes so much material the performance degrades. However, for the case of the photonic crystal it can be seen there is a continues improvement in performance as volume is removed [110].

The other strategy to achieve pioneering performance of IR detectors is development of devices that rely upon bandgap engineering for the reduction of dark currents in depletion-region. In particular, a properly designed nBn device bandgap [112-114] are able to overturn the flow of majority carrier electrons due to the large conduction band barrier. In fact, the nBn structure facilitates diffusion-dominated detector performance determined by the bulk minority carrier (hole) lifetime. This is in contrast with the high dark currents associated with depletion region generation-recombination currents in a conventional p-n junction. One example of such detectors is shown in Fig. 1.20. In the detector structure, for each pixel an array of multiple pyramid-shaped absorbers fabricated in the n-type InAsSb absorber. In fact, such structure for the detector offers a strategy to increase operating temperatures of the IR detectors consists of reducing the volume fill ratio of absorber material, exclusion of front-side reflection for incident light over a broad bandwidth, and enhanced photon trapping for high absorbance of incident light [113].

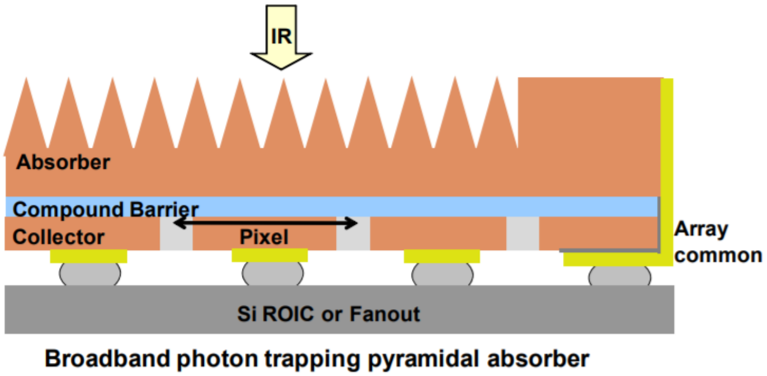

Figure 1.20: Schematic depiction of Compound barrier detector architecture with pyramid shaped absorber layer [113].

In conventional FPAs, practically the shape of the detector elements is square in order to have nearly 100% fill factor. The fill factor is defined as the fraction of the detector element area that is active in light detection. Since generally the more photon collection by a given detector pitch is desirable, then the fill factor should be considered as larger as possible. This leads to a higher signal-to-noise-ratio (SNR). But on the other hand, a high fill factor also tends to reduce the resolution and increase blurring due to the pixel cross-talk [115]. In the case of the per-pixel electronics, the area which is available for each pixel is reduced, so fill factor is often decreased to 60%. Therefore, the light falling in non-active region is either lost or, creates artifacts in the image due to the generating electrical currents in the active region [116].

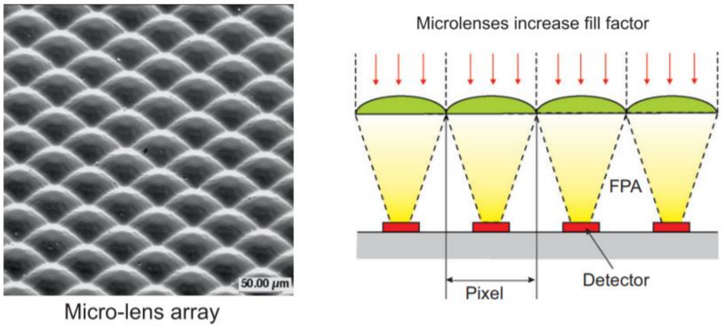

Micro-lens array

Figure 1.21: Micrograph and depiction of the micro-lensed FPA cross-sectional.

The fill factor and photon collection efficiency also can be regained by using the commercial microlens arrays as illustrated in Fig. 121. Microlens arrays allow collection of light from the entire area of the array followed by focusing light into compact photodetector mesas in such a way that each microlens is optically coupled to an individual pixel as illustrated in Fig. 1.22.

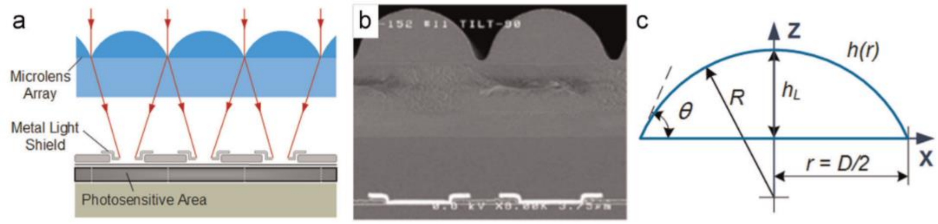

Figure 1.22: Depiction of typical microlens placement. (b) Micrograph of microlens array with plano-convex lens shape corresponds to one pixel. (c) A plano-convex microlens parameters including the lens diameter D, the height at the vertex h_L the radius of curvature R, the refractive index n and the contact angle θ [117].

Considering $h_L$as height of the vertex, and $r = D/2$ as the radius of plano-convex lens. Then, the radius of curvature (R) at the vertex and the vertex focal length (f) of the plano-spherical refractive lens can be given by [117]:

$$R = \frac{h_l}{2} + \frac{r^2}{2h_l} \qquad (1.10)$$

$$f = \frac{R}{n(\lambda) - 1} = \frac{h_l + r^2/h_l}{2(n(\lambda) - 1)} \qquad (1.11)$$

Where $n(\lambda)$ is the refractive index of lens material at desired wavelength (λ). Also, the lens profile $h(r)$ is generally described as [117]:

$$h(r) = \frac{1}{R} . \frac{r^2}{1 + \sqrt{1 - r^2/R^2}} \qquad (1.12)$$

But in practice, such commercially available optics provide imaging with relatively small angle of view (AOV) around ~1 degree. This is determined by the fact that the microlenses with a dome shape have only a single refracting surface with rather limited refractive index contrast [118]. Much larger AOVs are required for developing imaging sensors, optical perception systems, and, in general, systems for imaging in a broad range of distances and directions. micro-lenses are less effective [119] and may not be appropriate for all applications.

More recently, research from Professor Astratov's Mesophotonics Laboratory [120] has shown another application of microspheres associated with their ability to channel and concentrate light beams which can be very useful for improving sensitivity of the light detectors, especially detectors with limited photosensitive area or a device mesa [119, 120]. This is the subject of Chapter 4 of this dissertation and will be discussed later in more detail. In this dissertation, we present the results of numerical modeling describing the functionality and advantages of such FPAs. We will also mention about a possible technology which can be used for fabrication of such structures. The results on fabrication of such structures go beyond the scope of this theses work. (Including fabrication results in your theses would create a problem for Aaron's theses because the same results can be defended only once. Since you did the numerical modeling and Aaron did the fabrication, it seems that we should divide this work in your PhD theses, so that we will remove any penitential problem in future. Remember that both PhD theses will be published on Internet, and people would see who did what. It is in our interests to defend the part which you did, but to make sure that the other part is not claimed to avoid a potential problem in future).

1.4.2: Super-Resolution Microscopy

Achieving a spatial resolution that is not limited by the diffraction of light is the subject of interest for the Chapter 4 in this dissertation. In 1873, Ernst Abbe derived a formula explaining how the optical diffraction can limit the resolution of optical imaging system. However, lifting some of the constraints allows to extend the resolution beyond the diffraction limit. Multiple approaches to this so called optical super-resolution microscopy had been successfully demonstrated over last decades. In this section, we review some of the basic concepts as well as text book associated with defining the resolution of an optical system.

The resolution of an optical imaging system can be limited by factors such as imperfections in the lenses, aberrations or misalignment. However, there is a fundamental maximum to the resolution of any optical system which is due to diffraction. Light with wavelength λ, traveling in a medium with refractive index n and converging to a spot with half-angle θ will make a spot with radius

$$d = \frac{\lambda}{2n\,sin\theta} = \frac{\lambda}{2NA} \tag{1.13}$$

The portion of the denominator $n\,sin\theta$ is called the numerical aperture (NA) as illustrated in Fig. 1.24. Half-angle θ is the angle of the maximum cone of light that can enter or exit the lens. For standard lens in far field the NA can be defined as the ratio of diameter of the entrance pupil D to the twice focal length $2f$:

$$NA = \frac{D}{2f} \tag{1.14}$$

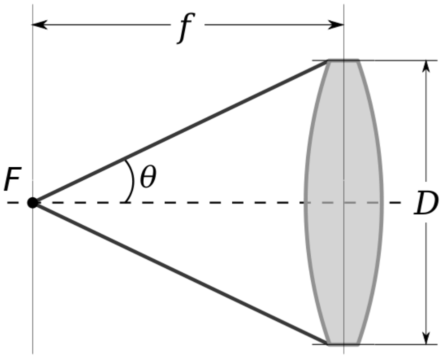

Figure 1.24: Illustration of the numerical aperture with respect to the point P.

There are some techniques used to enhance the image spatial resolution by optimizing NA. For instance, resolution improvement can be achieved by immersing both the objective lens and objective space in a transparent oil of high refractive index, thereby increasing the numerical aperture of the objective lens.

Using solid immersion lenses [121-129], either hemispherical (h-SIL) or super-spherical (sSIL) geometries are other options. The collection angle, and consequently spatial resolution can be also increased with the s-SIL. The resolving power of the optical imaging system also could be increased by using light of a shorter wavelength, i.e. violet or ultraviolet light [130-132]. However, it should be noted that the super-resolution imaging arises when the resolution of the imaging system beats the values predicted by these classical far-field diffraction limit.

1.4.2.1: Diffraction Limit and Resolution Criteria

The resolution of any optical imaging system can be limited either by aberration or by diffraction resulting in blurring of the image. These two phenomena are totally unrelated and have different roots. Aberrations basically can be described based on geometrical mechanism of ray optics and can in principle be corrected by increasing the optical quality of the optical system. While, diffraction comes from the wave nature of light and is determined by the finite aperture of the optical elements. The interplay between diffraction and aberration can be characterized by the point spread function (PSF). The PSF describes the response of an imaging system to a point source or point object. In other word, PSF being the impulse response of a focused optical system. In fact, any point in the object plane can be considered as a Dirac delta function, which should be convolved with the PSF of the imaging system and then form an image (impulse response) in the image plane [133].

The resolution of a system is defined based on the minimum distance d at which the points can be discerned. Several definitions are used to quantitatively determine the resolution. In the following section we describe the theoretical estimates of resolution, and various criteria which have been proposed such as Abbe [133], Rayleigh [134], Sparrow [135], and Houston [136]. In this review, we will consider incoherent image formation.

In this far-field case, a lens basically works as a low-pass wave filter. The field radiated by the small source in far field is modulated by the FT of the source distribution. Then, the lens transmits only that portion of radiated field which lies inside the collection cone of the lens. So, the plane wave components, which lie beyond the collection cone of the lens, are not captured by the lens and are not transferred over to the image plane. Consequently, loss of the high spatial frequency content causes blurring and loss of sharpness.

The Abbe diffraction limit for a microscope: In 1873 the German physicist Ernst Abbe discovered how microscopes were limited by the diffraction of light. According to the Abbe's microscope theory, an array of objects separated by distance d works as a diffraction grating with period d, therefore the incident light can be diffracted by these object features. This enables the use of the grating equation:

$$d\, sin(\theta_m) = m\lambda \tag{1.15}$$

Where θ_m is the angle between the m^{th} diffraction order and the normal vector to the surface of the grating, and λ is considered the free-space wavelength. The diffracted orders can be collected totally or partially by the imaging system, as shown in Fig. 1.25. The solution of grating equation for passing one of the first order diffracted rays through the lens gives us the Abbe diffraction limit. This was simultaneously formulated by Helmholtz as well:

$$d = \frac{\lambda}{2NA} \tag{1.16}$$

According to Abbe diffraction formula, for the imaging system, two-point objects, should be separated by more than roughly half the wavelength of illumination in order to resolved. The Abbe limit for the conventional white light source microscopes is $\backsim 200 - 250\ nm$.

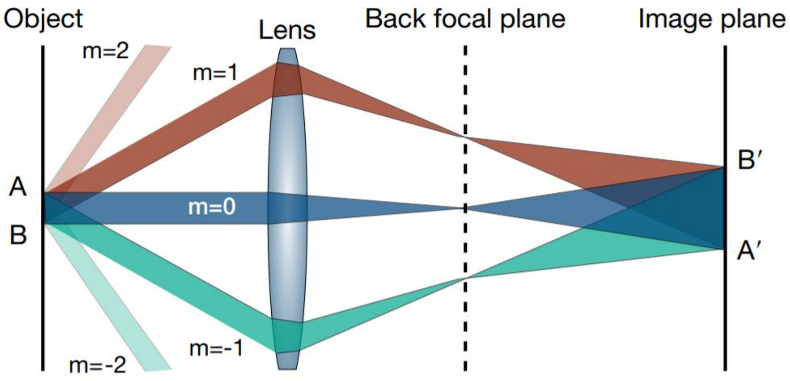

Figure 1.25: The two points objects AB is illuminated with coherent light. The light is diffracted into orders, shown with different colors (some orders are collected by the lens). In the back focal plane, the orders are separated; in the image plane, diffracted orders interfere to form the image $B'A$ [137].

The Rayleigh criterion is the generally accepted criterion for the minimum resolvable detail when the first diffraction minimum of the image of one-point object coincides with the maximum of another. Applying Rayleigh's resolution criteria for the irradiance patterns which produced from diffraction by square or circular shape apertures produce saddle points of 81.1% and 73.6%, respectively as illustrated in Fig. 1.26. Considering a circular shaped aperture, the PSF would be in the form of $Jinc^2 = J_1^2(x)/x^2$, where $J_1(x)$ is the first kind Bessel function. The irradiance pattern for the circular aperture is:

$$I(r) = I_0\left(\frac{2J_1(k_0 r\ NA)}{k_0 r\ NA}\right)^2 \tag{1.17}$$

Where the $k_0 = 2\pi/\lambda_0$ is the free space wave number of the illumination light. It can be shown that, for a circular aperture of diameter D, the first minimum in the Airy disk diffraction pattern occurs at $x = 1.22\pi$ where the distance between the point sources is equal to the radius of the mutual Airy disks. Therefore, the lateral resolution in Rayleigh limit calculated as:

$$\Delta_x = \frac{0.61\,\lambda_0}{NA} \tag{1.18}$$

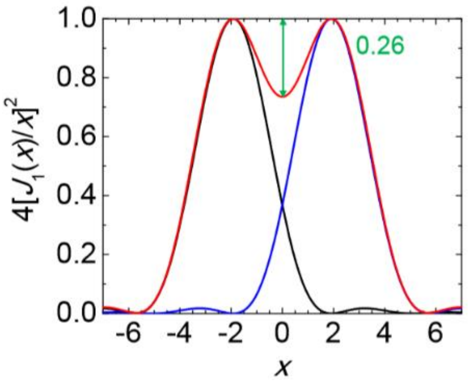

Figure 1.26: Rayleigh criterion for a circular aperture [138].

The other resolution criterion is the Sparrow resolution limit which is defined as the distance between two-point sources where there is no longer a minimum in brightness between the central peaks, but instead exhibit constant brightness across the region between the peaks, i.e. $\frac{\partial^2 I}{\partial x^2} = 0$ at $x = 0$ [135]. Mathematically the Sparrow's diffraction-limited resolution can be expressed as:

$$\Delta_x = \frac{0.473\,\lambda_0}{NA} \tag{1.19}$$

The Sparrow resolution limit is closer to the Abbe value and approximately two-thirds of the Rayleigh resolution limit. Moreover, the Sparrow is used more often in astronomy, while the Rayleigh and Abbe criterion are more conventional in microscopy.

The Houston criterion states that two-point sources with equal intensities separated by distance d can be resolved if the distance between the central maxima of the superposition of their irradiance profiles is equal to the full-width at half maximum (FWHM) of the irradiance distribution of either individual point source. The FWHM of the PSF for a circular aperture with NA is:

$$\Delta_x = FWHM = \frac{0.515\,\lambda_0}{NA} \tag{1.20}$$

This point should be considered that for all these criteria mentioned above, the image contract or signal-to-noise (SNR) which always present in experimental measurement is neglected. As a result, the resolution fundamentally depends on SNR. Also, if the PSF of the imaging system is precisely known, then there would not be any limitation to define the resolution of the system since two-point object model could be perfectly fitted to the data, regardless of the distance between the two-point objects. However, due to the lens imperfection, and aberration in experimental condition, the PSF of the imaging system could not be accurately measured [139].

Finally, it should be noted that super resolution microscopies are the techniques which improve the resolution of optical imaging systems without reducing the wavelength or increasing the framework of the instrument. In the following section we review some of these techniques which beat the diffraction limit.

1.4.2.2: Super-Resolution Techniques

Despite the advantages of traditional far field microscopies, the resolution of these techniques still is limited by diffraction of the light as it mentioned in previous section. In fact, in far filed microscopy, the role of evanescent waves which carry high spatial frequencies corresponding to sub-wavelength features of the sample is missed. Near-field optical systems can be beyond the classical diffraction limit by interacting with the evanescent wave or non-propagating fields which is light localized around object surface and drop off exponentially with distance from the object. The near-field scanning optical microscopy (NSOM) is an important method which provide an effective way to gain optical information of surface structures and optical field with a subwavelength resolution (Fig. 1.27). In this method the detector tip is scanning the sample using either at a constant height or with regulated height by using a feedback mechanism. Spatial resolution in NSOM techniques is then not limited by the applied wavelength or NA, and rather is limited by the size of the detector tip as well as the separation distance between the tip of the tapered optical probe and the sample surface. Currently for NSOM measurements the resolution is in order of ~50–100 nm range [140, 141]. However, long scan times for large sample areas for high resolution imaging, very low working distance and extremely shallow depth of field are the limitations should be counted.

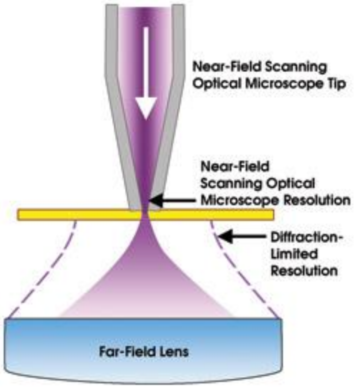

Figure 1.27: The schematic shows an apertured NSOM operating in transmission mode [142].

Emerging the fields of plasmonic and metamaterials within the last decade offer solutions for engineering extraordinary material properties such as negative refractive index (metamaterials) [143, 144]. This has provided great opportunities for novel lens to overcome diffraction limit. In the year 2000, John Pendry Initiated seminal concept of the perfect lens [145] to achieve nanometer-scaled imaging for focusing below the diffraction limit. The initial lens was based on using a slab of material with negative refraction of n = −1 as a flat lens. Such a lens allows near-field rays, which normally decay due to the diffraction limit, to focus once within the lens and once outside the lens, allowing subwavelength imaging. Pendry's theory experimentally demonstrated [146] (14??) at RF/microwave frequencies, and UV range (using thin layers of silver illuminated with UV light to produce "photographs" of objects smaller than the wavelength [147, 148]. Negative refraction of visible light was also experimentally verified in a transparent crystal in 2003.

Once capability for near-field imaging was demonstrated, the next step was to project a near-field image into the far-field. This concept, including technique and materials, is dubbed "hyperlens" [149, 150]. In fact, hyperlenses project super-resolution information to the far field through a magnification mechanism. Recently, there have been numerous designs for hyperlenses, bringing fresh theoretical and experimental advances, though future directions and challenges remain to be overcome.

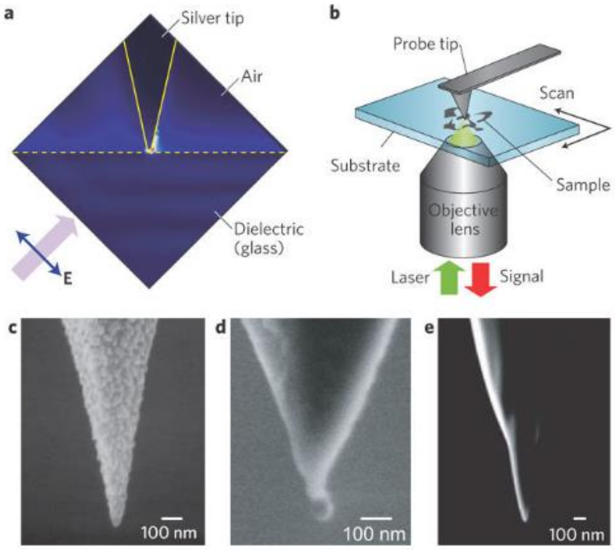

Figure 1.28: Schematic representation and SEM images of metallic nanoprobes (with 100 nm scale) applicable to see an object in nanometer resolution [151].

Immersion Microscopy techniques such as hemispherical SIL (h-SIL) [121] super-spherical SIL (s-SIL) [152] with possession of two aplanatic points (spherical aberration-free focal points) in a dielectric sphere [129] (Fig. 1.29) and nanometric scale SIL (nSIL are other type of super-resolution microscopy related to a theory by Born and Wolf [18] (Fig. 1.30). Such techniques are capable to improve resolving power by as much as 25%, in comparison to conventional millimeter scale SIL (macro SIL).

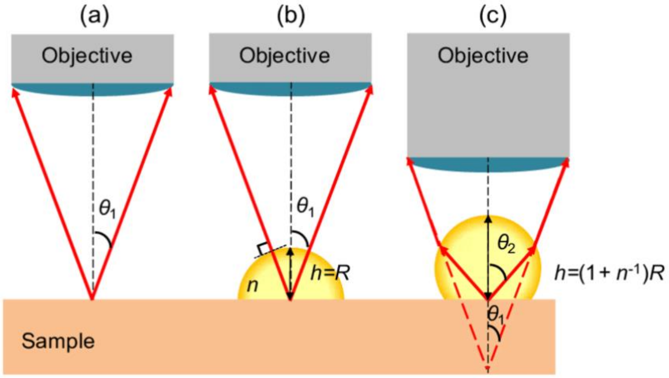

Figure 1.29: Schematic depiction of (a) An objective lens, (b) a hemispherical solid immersion lens (h-SIL), and (c) a super-spherical solid immersion lens (s-SIL). [138].

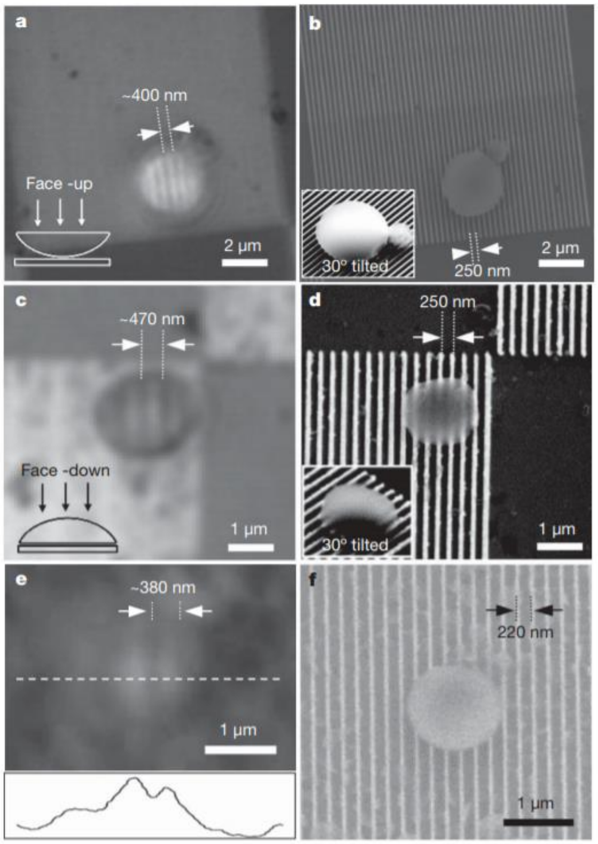

Figure 1.30: SEM images for images for nSILs. (a,b) a face-up lens and (c-f) face down lens, placed on a glass substrate with stripe patterns [153].

In 2011, it was proposed by Wang, et. Al [154], that the dielectric microspheres have the ability to resolve fine features due to the producing photonic nanojets as a consequence of optical reciprocity. Experimentally it was shown that Silica (n~1.46) microspheres 2<D<9 μm positioned on the stripes of a Blu-ray® disk (in 170 nm width and 130 nm separation) along with a nanometric scale star (fabricated with a ~90 nm corner) can form super resolved virtual image of these objects as shown in Fig. 1.31. It was claimed that this technique does not work either for full-immersion of microsphere or in the case when the refractive index of microsphere is bigger than 1.8 [154].

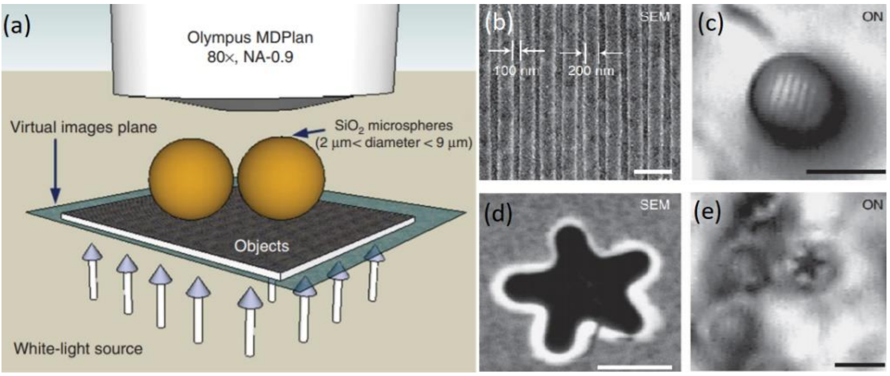

Figure 1.31: (a) Depiction of an optical nanoscope in its transmission mode. (b) SEM image of a Blu-ray® disk without microsphere, (c) the optical imaging of the Blu-ray through microsphere superlens in reflection mode, (d) and (e) the SEM image and optical image of nanometric scale star respectively [154].

More insight into the microsphere assisted microscopy was performed by Professor Astratov's research group in Mesophotonics Laboratory [155-159]. Initially, they used high-index (n~2) barium titanate glass (BTG) microspheres immersed in a liquid. It was an important advancement in this field because it opened the gates for imaging biomedical samples such as subcellular structures, viruses, and proteins. After that they performed label free super resolution microscopy using BTG microspheres which were embedded in polydimethylsiloxane (PDMS) thin-films They demonstrated that the resolution ~λ/6-λ/7 (where λ is the illumination wavelength) can be systematically achieved in the images of nanoscale arrays of Au dimers and bowties (Fig.1.32). They also developed a technology regarding the fabrication of transparent elastomeric PDMS slabs holding hundreds of high-index BTG microspheres. Such coverslips can be considered as a novel optical component for super-resolution microscopy [155].

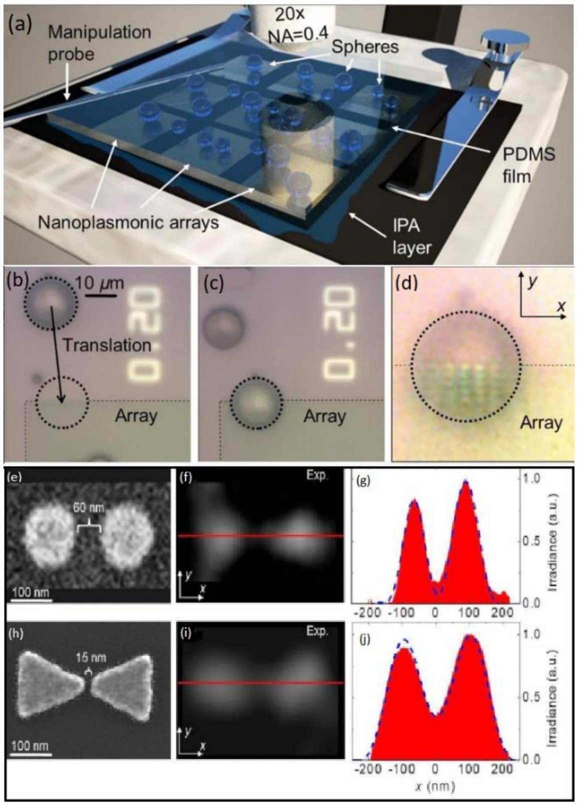

Figure 1.32: (a) Schematic representation of the microscopy experimental setup using BTG microsphere embedded in PDMS coverslip, (b-d) translation of the coverslip lubricated with IPA. (e,h) SEM image of Au dimer and bowtie respectively. (f,i) Virtual image of the dimer and bowtie obtained through the 5 μm and 53 μm BTG microsphere respectively and (g,j) calculated resolution using 2-D PSFs with FWHMs of λ/7 and λ/5.5 for Au dimer and bowtie respectively[155].

Along with the methods we mentioned so far, there are other methods for functional super-resolution microscopy which basically fall in two main groups of, (a) stochastic super-resolution which use mathematical models to reconstruct a sub diffraction limit from many sets of diffraction limited images (including photoactivated localization microscopy (PALM), stochastic optical reconstruction microscopy (STORM), and Structured illumination microscopy (SIM)) , and (b) deterministic super-resolution which rely on the non-linear response of fluorophores commonly used to label biological samples in order to achieve an improvement in resolution (such as stimulated emission depletion (STED) microscopy [160-162]), and ground state depletion (GSD) microscopy [163, 164]). Here we briefly review one example for each category.

Structured illumination microscopy (SIM) is a wide-field fluorescence technique in which a series of excitation light patterns are generated through interference of diffraction orders and superimposed on the unknown sample structure while capturing images [165]. The concept behind structured illumination microscopy can be understood based on Moiré effect when two fine patterns are superposed multiplicatively, a beat pattern or Moiré fringes will appear in their product in Fourier space as illustrated in Fig. 1.33. Such moiré fringes can be much coarser than either of the original patterns, and in particular may be easily observable in the microscope. Since the illumination pattern is known, the moiré fringes contain the information about the unknown structure. The Fourier transform (FT) of an SI image contains superimposed additional information from different areas of reciprocal space which cause normally inaccessible high-resolution information to be encoded into the observed image [165].

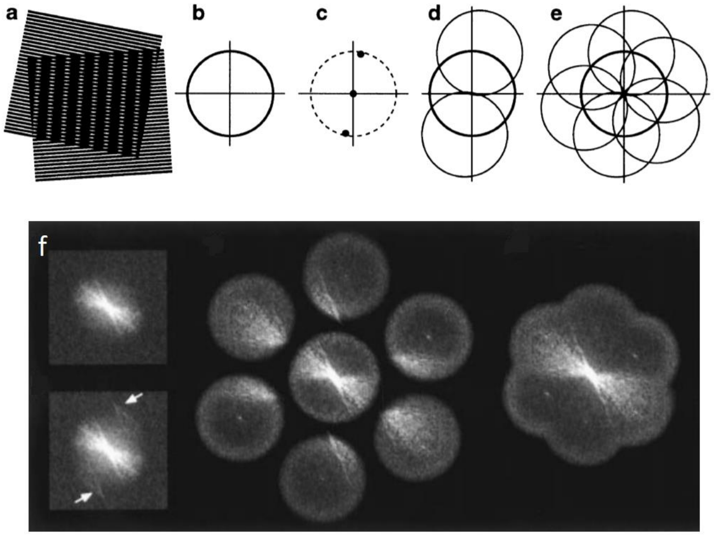

Figure 1.33: Illustration of the concept of resolution improvement in SIM. (a) formation of moiré fringes where two fine patterns are superposed multiplicatively. Reciprocal space translated for (b) conventional microscope (c) A sinusoidally striped illumination pattern (d) three Fourier components of the illumination in reciprocal space which move information beyond the diffraction limit circle in (b). (e) different orientation and phase of the pattern which make it possible to recover information from an area twice the size of the normally observable region, and consequently exceed the fundamental resolution limit of the wide-field fluorescence microscope by a factor of two. (f) example for the reconstruction procedure in reciprocal space [165].

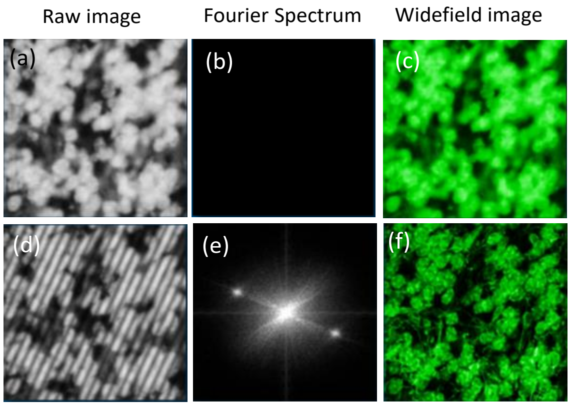

Figure 1.34: Comparison of the resolution obtained by conventional microscopy (top) and structured illumination microscopy (bottom) [166].

Fig. 1.34 shows a comparison between conventional microscopy versus SIM as well as their FT of the images in the reciprocal space. In SIM several images are captured for each orientation angle of the grid to generate one image subset. After image subsets are obtained for each of the grid orientations, the collection can be analyzed through a specialized algorithm to produce a reconstructed image having a lateral resolution approximately twice that of diffraction-limited instruments Fig. 1.33. The widespread availability of dyes and fluorescent proteins for labeling specimens and the ease of conducting multicolor imaging are some benefits of high resolution structured illumination microscopy, however the length of processing time necessary to generate high resolution images is about 1 to 30 seconds, which makes a drawback for this method in some application [166].

There are some extension of SIM method including plasmonic structured illumination microscopy (PSIM) [167], localized plasmonic structured illumination microscopy (LPSIM) [168], and optical tweezers based LPSIM (OT- LPSIM) [169]. It was experimentally shown by Feifei Wei et al., [167] that by replacing the laser interference fringes in conventional SIM with surface plasmon (SP) interference patterns, the resolving power can be enhanced due to the unique properties of SP waves. Also using finely structured, resonant, and controllable near-field excitation from localized surface plasmons in a planar nanoantenna array, the wide-field surface imaging with resolution down to 75 nm can be achieved. Reasonable speed and compatibility with biological samples are the advantages of these methods.

STED microscopy operates by using two laser beams to illuminate the sub-diffraction object [160]. In this technique, by using the second laser, the effective PSF of the excitation beam is altered in a way to suppresses fluorescence emission from fluorophores located away from the center of excitation as illustrated in Fig. 1.35. The suppression of fluorescence can be happening through stimulated emission before spontaneous fluorescence emission occurs in the depletion region. As a result, only the center of illumination where the STED laser intensity is zero, fluorescence remains unaffected and is detected by single-photon sensitive detectors. This action effectively narrows the point spread function and ultimately increases resolution beyond the diffraction limit [160-162]. This sub diffraction resolution can be described by modified Abbe's equation:

$$d = \frac{\lambda}{2n\, sin\alpha \sqrt{1 + \frac{I}{I_{sat}}}} \tag{1.21}$$

Where n is the refractive index of the medium, I is the intracavity intensity and I_{sat} is the saturation intensity. Currently STED microscopy is capable of 20 nanometer (or better) lateral resolution.

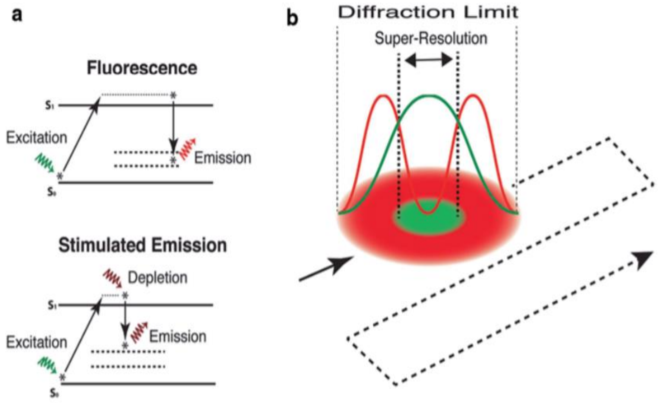

Figure 1.35: Illustration of stimulated emission depletion (STED) microscopy principle. (a) simplified Jablonski diagram illustrating the transitions in electronic state during normal fluorescence and during stimulated emission (b) A doughnut-shaped depletion laser (in red) effectively reduces the point spread function (PSF) of normal fluorescence (in green and marked by a double arrow) below its diffraction limit [170].

1.5: Summary

This Ph.D. dissertation is devoted to study the optical properties and device functionality of Mesophotonics structures formed by dielectric spheres and by microphotonics building blocks with characteristic dimensions varying from several wavelengths up to hundreds of wavelengths. These building blocks are capable of confining light inside them due to total internal reflection which leads to formation of high-quality whispering gallery mode resonances. They are also capable of focusing of light leading to formation of so-called photonic nanojets. In more complicated structures and devices formed by multiple building blocks it leads to the following effects:

- Fundamental WGM hybridization effect due to spatial overlap of the evanescent fields of WGMs in neighboring circular resonators.
- WGM excitation in complex structures and devices determined by evanescent coupling with tapered fibers and stripe waveguides. The mechanisms of coupling light in- and out of such structures play an important role in designing sensors of nanoparticles.
- Optical routing and unidirectional optical transmission in photonic molecules and coupled cavities where spatial asymmetry and losses play an important role.
- Use of photonic jets produced by dielectric microspheres for increasing sensitivity and angle-of-view of MWIR detectors, and

- Experimental approach for super resolution nanoscopy where nanoplasmonic nanoarrays is used either as object for imaging or as layers providing structured illumination of various nanoscale objects.

The work presented in Chapter 2 builds upon previous studies of simplest coupled cavity structures such as dielectric bi-spheres. The unresolved issues in this area include mechanisms of coupling between multiple cavities, namely the questions about the spatial configuration of supermodes and how the spectral properties of these supermodes correlate with spatial configurations of photonic molecules. They were only few studies of these effect in previous literature and the task of this theses work was to perform a systematic study of these effects using finite difference time domain modeling. To simplify the task, in this dissertation we used a simplified 2-D model of in-plane coupling between circular resonators. This simplified geometry catches the essential physics of evanescent WGM coupling effects taking place in equatorial plane of touching or almost touching real physical 3-D microspheres. The problem of numerical studies is the fact that each computed result describes only one set of parameters and making conclusions about the physical properties and effects requires a significant variation of all structural parameters. In this theses work, this is achieved by variation of the refractive index of circular resonators and surrounding medium as well as the diameter of such resonators. By using systems side-coupled to a stripe-waveguide, we study photonic molecules with various number of constituting atoms assembled in various spatial configurations. By varying the structural parameters in a wide range, we come to the conclusion that some of the spectral properties of given photonic configuration are preserved. Namely, this is a type of splitting of WGM components in such strongly coupled systems which we called “spectral signatures” of photonic molecules.

In Chapter 3, we study the transmission properties of side-coupled circular cavity systems based on numerical two-dimensional finite-difference time domain modeling. The spatial asymmetry is introduced due to different separations between the circular resonators and side-coupled stripe waveguides. These structures can be viewed as 4-port routers where different ports are connected due resonant coupling between the guided modes in stripe-waveguides and whispering gallery modes in circle resonators. Due to strongly asymmetric geometry, significant optical losses, and mode conversion processes, such structures display strongly asymmetric optical transmission properties for the waves propagating in forward and backward directions between the ports. We show that conventional theory of coupled cavities is often based on a concept of phase-matching. This concept leads to a predictable direction of the flux of energy in more complicated multi-port coupled-cavity structures. However, we show that it works only for sufficiently large circular resonators with sufficiently small refractive index contrast where the effective length of the coupling regions with the stripe-waveguides is much longer than the wavelength of light. We show that in the case of coupled-cavity structures formed by high-index circular resonators with compact dimensions, the coupling conditions between the cavities and coupling conditions with the stripe-waveguides are changed in a sense that the effective length of the coupler regions becomes comparable to the wavelength of light and, as a result, the phase matching condition is relieved. This leads to much more complicated connectivity between different ports in such structures which depends on such parameters as spectral properties of excitation, a degree of spatial asymmetry of such structures leading to asymmetric losses for propagation in forward and backward direction. Another fundamental issue is connected with the mode conversion processes taking place in such structures. The modes excited in different parts of such structures have different symmetry and polarization properties. The combination of spatial asymmetry in a form of asymmetric coupling gaps with the stripe-waveguides leading to asymmetric losses and mode conversion taking place inside such structures result in very complicated functionality. As an example, we show that the optical pulses centered around different wavelengths in such structures can be delivered to different ports which generally represent routing functionality. We also show that transmission between two different port can be highly asymmetric in such structures.

In Chapter 4, we develop previous results of Prof. Astratov's lab based on developing various applications of photonic jets. One of the trends in design of mid-wave infrared (MWIR) focal plane arrays (FPAs) consists in reduction of the pixel sizes which allows increasing the resolution and decreasing the dark currents of FPAs. To keep high light collection efficiency and to combine it with large angle-of-view (AOV) of FPAs, previously it was proposed to use photonic nanojets produced by dielectric microspheres in order to focus light on a compact photodetector mesa. However, the engineering of such structures remained largely unexplored. As an example, the microspheres need to be fixed on a surface on FPA in such a way that each sphere is centered with the corresponding pixel. This implies that some kind of glue or a photoresist layer with the ability to solidify can be used to fix microspheres in a position. In this PhD theses work, we developed practical designs of such structures which include these layers used for fixing spheres in two situations. One is the case of back-illuminated and another one is the case of front-illuminated structures. We varied the index and size of microspheres as well as the thickness of the photoresist layer to achieve the best focusing on the photodetectors of FPAs. We study how the efficiency of such FPAs enhanced by microspheres depend on the angle of incidence and we demonstrate significantly larger angle-of-views (AOVs) of such structures compared to standard microlens arrays.

In Chapter 5, we experimentally as well as using modeling study investigate the impact of nano-plasmonic effect on super resolution nanoscopy by using dye doped nano-spheres and different plasmonic arrays via confocal microscopy. The idea of our experiments is based on the fact that localized surface plasmon resonances (LSPRs) have drastically different spectral properties in different metals. LSPR are rather broad and their spectral positions depend on the size of metallic islands leading to different amount of size quantization contributions to the energy of LSPR. However, if we skip the details and consider the resonant properties on more quantitative scale, one can say that LSPRs in sufficiently small Au nanostructures tend to resonate in green and red regions of visible spectrum, whereas LSPRs in Al nanostructures with comparable dimensions tend to resonate in blue. By using these arrays for structured illumination of blue and green fluorescent nanospheres, we showed that the best resolution of green FL nanospheres can be achieved with Au arrays, whereas the best resolution of blue FL nanospheres require Al arrays. Thus, our results provide a direct experimental prove of the important role which LSPRs play in achieving optical super-resolution. In addition, we show that maximal resolution requires minimization of the periods of these arrays. The latter property is related to mechanisms of SIMs.

CHAPTER 2: MODELING STUDY OF WHISPERING GALLERY MODE HYBRIDIZATION IN PHOTONIC MOLECULES

2.1 Introduction to Photonic Molecule

In this Chapter of the dissertation, we study the resonant optical properties of photonic molecules through FDTD modeling. As is discussed in Introduction Chapter, photonic molecules can be formed by electromagnetic coupling of two or more optical microresonators in different configurations including linear chains and 2-D clusters of resonators. In general, artificial molecules can be synthesized from nanoscale and microscale resonant building blocks such as nanoplasmonic particles or microspherical whispering gallery resonators. The inspiration in this area comes from chemistry where molecular complexity and symmetry are central concepts for predicting hybridization of electronic states evolving from the individual atomic orbitals. In plasmonics, in recent years, all types of simple artificial molecules have been developed from metallic nanostructures including dimers [171-173] , trimers [174], planar quadrumers [175], hexamers and heptamers [176]. In all these structures, the electromagnetic fields of individual particles extend away from the particles in a way reminding behavior of atomic wave functions. By bringing metallic particles closer to each other, a transition from isolated to collective modes of plasmonic molecules can be realized [176]. It should be noted, however, that the localized surface plasmon resonances

(LSPR) associated with collective excitation of conductive electrons in the metallic nanoparticles are spectrally broadened with the typical width on the order of 20-40 nm [177]. This factor simplifies the fabrication of homogeneous plasmonic molecules where the individual LSPRs are aligned. In addition, the spectral manifestation of hybridization effects in plasmonic molecules can be described in a relatively simple way in a dipole approximation using such concepts as bonding and antibonding modes as well as dark-hot resonances [178]. In contrast, microspherical whispering gallery modes (WGMs) have much higher effective quality (Q) factors usually $>10^4$.

The analogy between the quantum mechanics and the classical electromagnetics was noted long ago, and Stephen Arnold was the first to introduce the terminology of "photonic atoms" [76]. However, building photonic molecules from classical photonic atoms brings about an interesting problem of identity of microspherical WGM resonators required for achieving homogeneous photonic molecules and circuits. If WGM resonances are misaligned in the individual photonic atoms, their coupling and hybridization is inefficient [56, 179-183]. On the other hand, aligning extremely narrow WGM resonances in individual microspheres represents a challenging problem. At the same time, coupled cavity structures can be fabricated without using microspheres by standard in-plane technologies, but these studies revealed the same problem related to inevitable size and shape variations of individual microdisks, rings and photonic crystal cavities with corresponding misalignment of their resonances [184-186].

It should be noted that one of the primary motivations to study WGM resonators is related to their sensor applications [187, 188]. The use of clusters of microspheres for developing sensor applications has been proposed as a way of diversification of WGM spectra and distinguishing individual clusters of microspheres [189]. However, the sorting of individual atoms with resonant properties was not performed in this work, and the WGM hybridization effects were outside the scope of Ref. [189]. Another example of application of weak coupling between WGMs was a proposal of detection of the orientation of molecules' dipole moments in clusters of identical microspheres separated with micron-scale gaps [190]. In contrast, in the present study we introduce the "spectral signature" of a photonic molecule, strictly as a result of WGM hybridization effects. In the present work, these effects take place in sorted spheres with almost identical wavelengths of the uncoupled WGM peaks when such spheres are placed in a contact position.

The potential advantages of strongly coupled cavities over individual resonators in sensor applications have been noted previously. It has been suggested that they are capable of differentiating between bulk and surface perturbations of the ambient refractive index as well as between specific and nonspecific binding of molecules on the sensor surface [191]. This is based on tracking the shifts of hybridized bonding and antibonding optical modes in coupled optical microcavities [191]. They can be potentially used in Raman or fluorescent sensors with tailored excitation and emission spectral resonances [192] and in opto-plasmonic molecules [193, 194]. Similar to single microresonators [195], they can be used for developing on-chip single nanoparticle detection and sizing by mode-splitting. In this work, we predict more sensitive detection of single nanoparticles in two-atom molecules compared to single atom systems.

In the first studies of simplest homogeneous molecules [58, 81, 196, 197] this task was solved by manual sorting of few spheres with similar WGM peak positions out of hundreds of spheres with a standard size deviation of about 1%. This method made it possible for some basic studies of WGMs hybridization in bi-spheres considered as an analog of "photonic hydrogen" molecule. However, this methodology was too inefficient for developing more complicated structures and practical applications.

In parallel with building the simplest photonic molecules, an interest emerged in resonant light forces which can be used for manipulation of microspheres[198-200]. Practical methods for largescale sorting of microspheres based on using resonant optical forces was previously proposed in Mesophotonics Lab [201], experimentally realized spectrally resolved optical propulsion of microspheres in evanescent field couplers [202-205], and developed the theory of these effects [57, 58, 179, 181, 206-247]. These developments in principle allow sorting large quantity of microspheres with uniquely identical resonant properties which can be used for developing new technology of heterogeneous artificial photonic molecules with the WGM resonance deviations within 0.01%.

The WGM hybridization effects in such structures are considerably more sophisticated compared to their nanoplasmonic counterparts. Such narrow WGM peaks allow observations of fine splitting effects related to symmetry and topology of the photonic molecules. Besides the purely fundamental interest, such artificial molecules can be used for engineering the density of photonic states, designing structures with the “optical supermodes”[78, 248], exploring quantum-optics analogies in photonics [249], and designing structures with unidirectional optical transport properties [250]. On a more practical level, such structures can be used for reducing the threshold of lasers, developing coupled-resonator optical waveguides (CROWs) with controllable pulse delay properties, as well as sensors and filters with desired spectral characteristics.

In this Chapter of dissertation, we performed a theoretically study of WGM hybridization in photonic molecules built by resonant microspheres with wavelength matching WGMs. The schematic representation of various molecules studied in planar geometry using side-coupling to WGMs is illustrated in Fig. 2.1. The numerical simulation is performed in 2-D case corresponding to the equatorial cross-section of the 3-D structures. The modes’ excitation is provided evanescently using side-coupled tapered fiber

[213]. Fiber transmission spectra were presented for 3-sphere and 4-sphere chain molecules as well as 2-D molecules such as trimers, quadrumers and hexamers. The transmission spectra were investigated with three different sphere/medium index combinations.

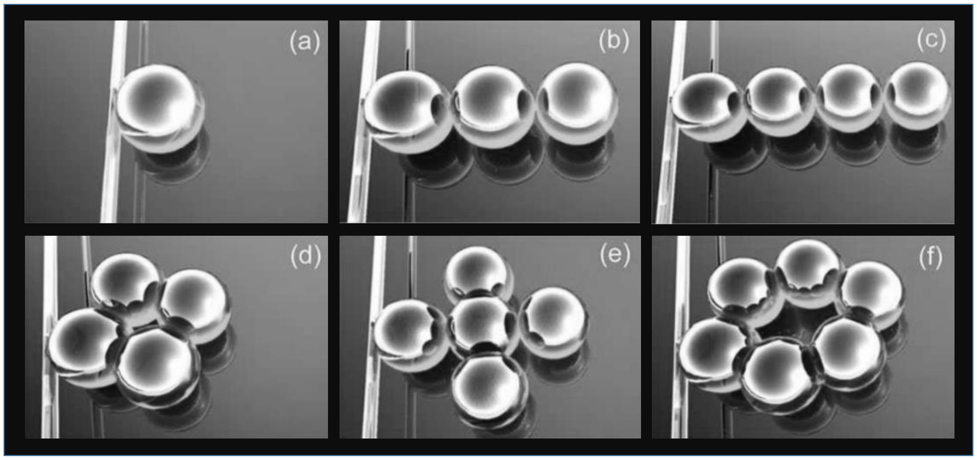

Figure 2. 1: Schematic presentation of the various configurations of photonic molecule side coupled with tapered fiber: (a) single atom, linear chains of (b) 3 circular resonators and (c) 4 circular resonators, and planar(d) quadrumer, (e) 5-atom cross and (f) hexamer [251].

One of the important observations of our work is that photonic molecules have certain spectral properties which are closely related to the topology and geometry of a given molecular configuration. The number of atoms determines the number of spectral components which can be split or degenerate depending on the symmetry. The spatial configuration determines the spectral positions of the split components relative to the uncoupled WGM peaks. The precise amount of splitting depends on the parameters of a given system such as the diameter and index of the microspheres and index of the surrounding medium. However, in more qualitative terms, the type of the splitting depends on the symmetry and topology of the given molecules so that it represents the number of atoms and their spatial arrangement for a given molecule. The stable spectral characteristics are represented by the total number of the split components and their spectral shifts considered in relative units. We termed the combination of these properties "spectral signature" of a given photonic molecule. Numerical methods of electromagnetic modeling used in our work do not allow us to generalize our observations and to claim that the spectral signatures are absolutely fixed characteristics. However, we show that in a certain range of variation of parameters which corresponds to a variety of practical situations, the spectral signatures are relatively stable. This means that in principle they can be used for identification of various molecules and such spectroscopic characterization can allow distinguishing between different photonic molecules. Such spectral molecular identification is of course only a distant analogue of Raman spectroscopy. Still, such identification can be made reliably.

2.2: Spectral Signature of Photonic Molecules by FDTD Simulation

We used a simplified 2-D model for understanding the underlying physical properties of 3-D geometry of the optically coupled microspheres. In 3-D case, WGMs in microspheres are defined by radial (q), angular (l), and azimuthal (m) mode numbers [56, 58, 81, 196, 197]. The radial number, q, indicates the number of WGM intensity maxima along the radial direction, the angular number, l, represents the number of modal wavelengths that fit into the circumference of the equatorial plane of the sphere. The azimuthal mode number, m, describes the field variation in the polar direction, with the number of intensity maxima along this direction being equal to $l-|m|+1$. The "fundamental" mode has l=m and q=1. In deformed spheres, the degeneracy of azimuthal modes represented by m numbers can be lifted [252]. The splitting of azimuthal modes, however, is usually observed in fluorescence measurements where all WGMs can be relatively easily excited. In contrast, in experiments with tapered microfibers the orientations of the WGMs orbits are determined by the positions where the tapered fibers touch the spherical surface. In this sense, the orientation of the modes excited in first sphere adjacent to the taper is determined by the position and orientation of the taper. The photonic molecules are assembled on a substrate, and individual WGMs in different spheres couple most efficiently in the equatorial plane parallel to the substrate. If the taper is parallel to the substrate and touches the closest microsphere in this equatorial plane, as schematically shown in Fig. 2.2, the coupling problem acquires some features of 2-D geometry. The spheres can be modeled as circular resonators with the diameter equal to the sphere diameter. A tapered fiber can be modeled as a 2-D strip waveguide with 1.5 µm width and refractive index of 1.45. It was placed in close vicinity (typically 100 nm in our modeling) to the circular resonator for side-coupling.

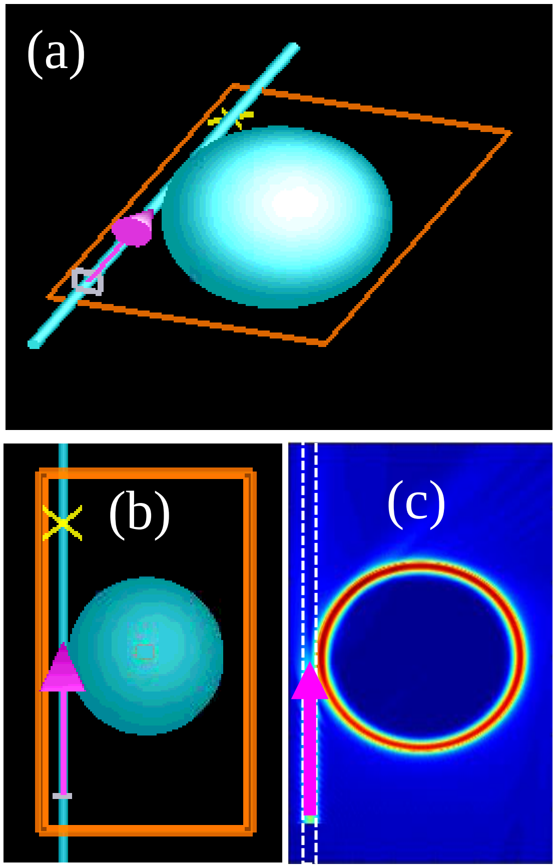

Figure 2. 2: Schematic presentation of single sphere side coupled to tapered fiber waveguide. (a) 3-D geometry. (b) Circular resonator in 2-D geometry at the equatorial cross-section of the 3-D structure (c) Electric field map in frequency domain at the resonant wavelength.

The WGMs in such 2-D geometry are described by radial and angular numbers [220]. This model is also applicable to cylindrical resonators such as semiconductor micropillars [214, 253]. The numerical simulation was performed by finite difference time-domain (FDTD) method [254] with commercial software by Lumerical [197]. A Gaussian modulated pulse (Fig. 2.3) of ~10 femtoseconds width was launched into the waveguide from the bottom upwards, as illustrated in Fig. 2.2(b,c).

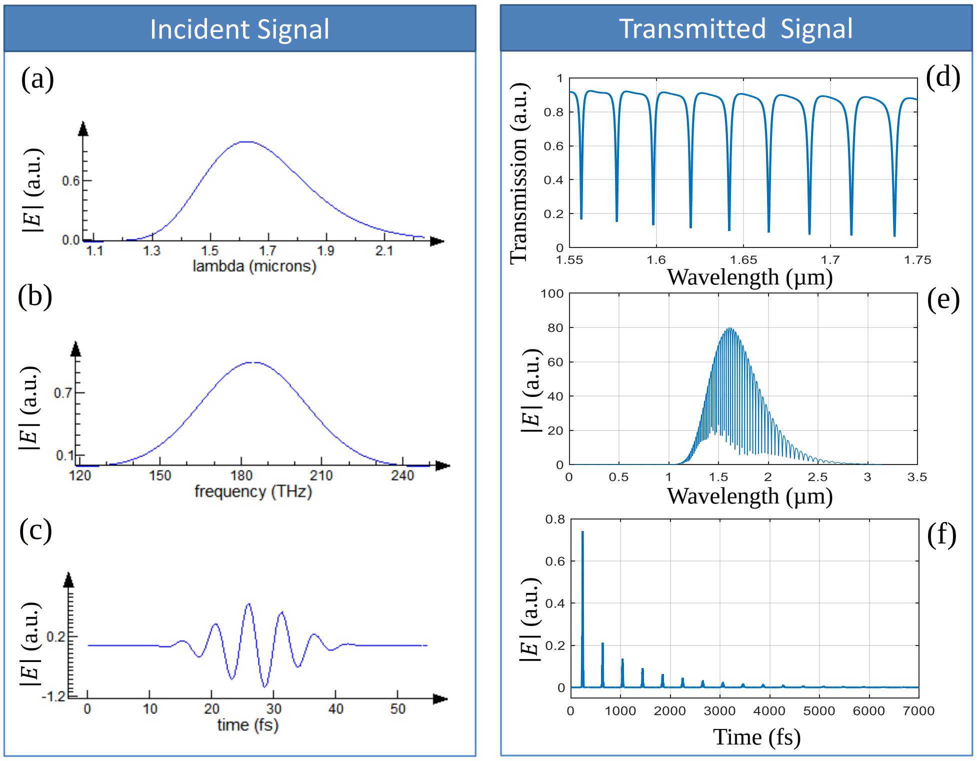

Figure 2. 3: (a-c) Input pulse of the electric field, (a) Spectrum vs Wavelength, (b) Spectrum vs Frequency, and (c) Signal vs Time. (d-f) Calculation of E-field transmission spectrum using (d,e) frequency domain monitors in terms of wavelength, and (f) time domain monitor.

The electric vector of electromagnetic waves was linearly polarized in the plane. In 3-D case, this situation has a close analogy with excitation of TM polarized WGMs in the equatorial plane of spheres. The transmission through the fiber was calculated as a function of time, and the broadband transmission spectra were obtained using Fourier transform [255-259]. Due to WGMs' nature of trapping light, the simulation involving microresonators needs sufficient time to allow multiple pulse circulations and pronounced decay of the coupled light. We chose the simulation shut-off criteria as when the electric field in the computational space is less than 10^{-5} of the input field and found the results converged well. Several circular resonators in contact position represent various configurations of photonic molecules. Five configurations of photonic molecule were studied, including linear chain of 3 circular resonators (Fig. 2.4(b1)) and 4 circular resonators (Fig. 2.4(c1)), planar quadrumer formed by 4 circular resonators (Fig. 2.4(d1)), cross formed by 5 circular resonators (Fig. 2.4(e1)), and hexamer formed by 6 circular resonators (Fig. 2.4(f1)). In order to find the spectral signature commonly seen in each configuration, the simulations were performed for three different combinations of the structural parameters. The refractive indices (n) and diameters (D) of microspheres are shown in different media (air or water) in three situations illustrated in Figs. 2.4(a2-a4), respectively. Appropriate diameters were chosen for each case to ensure WGMs of first radial order ($q = 1$) are well pronounced while second-order modes are suppressed. This approach enables unambiguous observation of supermodes in the fiber transmission spectrum that arises from inter-resonator coupling of WGMs with the same radial and angular modal numbers.

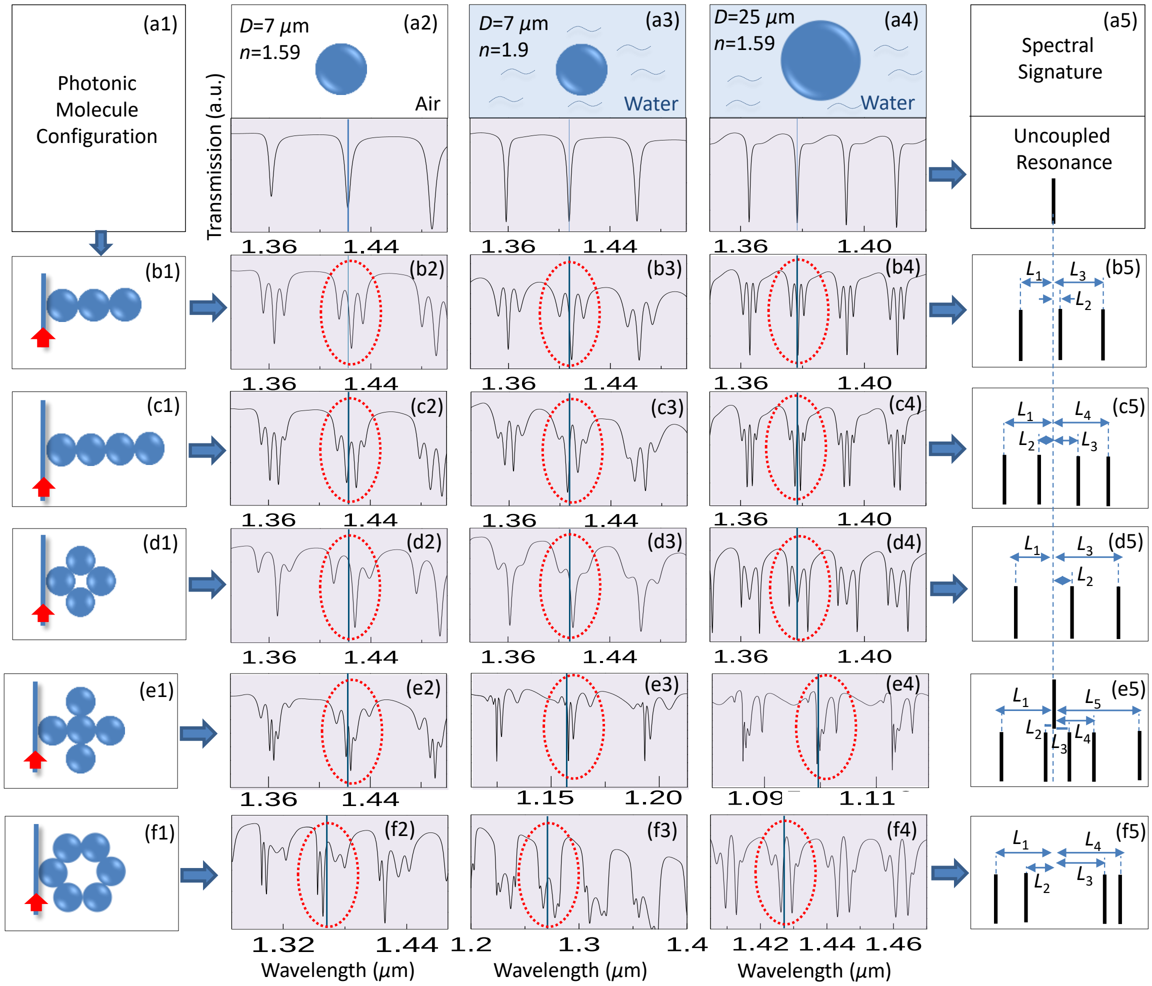

Figure 2. 4: (a1) Molecular configurations including: linear chain of (b1) 3 circular resonators and (c1) 4 circular resonators, and planar (d1) quadrumer, (e1) 5-resonator cross and (f1) hexamer. Simulated transmission spectra of (a2-a4) single resonators and various (b2-b4, c2-c4, d2-d4, and e2-e4) molecule configurations. In these spectra, the column (a2-f2) corresponds to *D*=7 *μ*m with n=1.59 in air, the column (a3-f3) corresponds to *D*=7 *μ*m with n= 1.9 in water and the column (a4-f4) corresponds to *D*=25 *μ*m with *n*=1.59 in water, respectively. (a5-f5) Spectral signatures for corresponding photonic molecules [251].

The transmission spectra of side-coupling to single circular resonators are presented in Figs. 2.4(a2–a4) respectively for these three cases. The spectra show periodic dips due to light coupling to WGMs in circular cavities. The

WGMs of a single resonator are referred to as uncoupled modes here to be distinguished from supermodes in photonic molecules. Simulation results for molecule configurations in Figs. 2.4(b1–f1) are presented in their corresponding rows. Strong coupling and mode splitting are observed in every case. Blue vertical line indicates the wavelength of the uncoupled mode, which helps to compare the relative positions of the split supermodes (in the case of cross-shaped molecule in Figs. 2.4(e3,e4) and in the case of hexamer molecule in Figs. 2.4(f2–f4), the position of the uncoupled mode is shifted compared to other structures). Red ellipse marks a set of supermodes that arises from inter-resonator coupling of one WGM, representing a reproducible unit that periodically appears in the spectrum separated by the free spectral range. As one can see, the splitting patterns of supermodes are quite similar even though the diameter of circular resonators is varied from 7 μm to 25 μm, their index was varied from 1.59 to 1.9, and the medium was changed from air to water. As an example, in Figs. 2.4(b2–b4) the uncoupled WGMs from single resonator are split into three supermodes. These modes are almost equally separated, and the central one has much higher magnitude, as interpreted by the depth of the dip in the transmission spectrum. A slight red shift of the central mode compared to the uncoupled mode is also noticeable in all cases. As a summary of the splitting patterns commonly seen in all three cases, we plotted supermodes' positions relative to the position of uncoupled mode in Fig. 2.4(b5). Relative distance from each supermode to the corresponding uncoupled WGM resonance is shown as LN, where number N represents the order in which a given resonance appears in the transmission spectrum from left to right. We call this stable property represented by the total number of split supermodes and their relative positions to the uncoupled mode as the spectral signature specific to such a photonic molecule.

Spectral signatures summarized for each photonic molecule are presented in Figs. 2.4(b5–f5). In the case of linear chain molecules, the total number of supermodes is equal to the number of constituting atoms. For a linear chain of 3 circular resonators in Figs. 2.4(b2–b4), the position of the central supermode is slightly red shifted (L2) relative to the uncoupled mode [260]. The splitting is almost symmetric with equal separation between adjacent supermodes. These observations are in agreement with Bloch modes formed in a coupled linear structure [182]. For a linear chain of 4 circular resonators in Figs. 2.4(c2–c4), four almost evenly spaced supermodes can be revealed. However, for 2-D molecules with non-straight geometry the symmetric splitting is no longer present. Transmission spectra in Figs. 2.4(d2–d4) show uncoupled mode splitting into three supermodes when a planar quadrumer is formed by 4 circular resonators. In comparison to a 3-sphere chain which also yields three supermodes, the modes in the square molecule (Fig. 2.4(d2–d4)) have wider and uneven splitting (L1+L2 and L3-L2) and larger red shift (L2) for a central supermode. The ratio (L1+L2)/(L3-L2) is found to vary in structures with different index and size of the constituent atoms. It is seen in Fig. 2.4(d4) that this ratio is closer to unity compared to that in Figs. 2.4(d2–d3). The combination of these properties can in principle be used for distinguishing such quadrumer's molecules from linear chains based on the spectral analysis. The cross-shaped molecule formed by 5 circular resonators has a spectral signature with 5 supermodes, where the splitting of central supermodes (L2+L3 and L4 –L3) is smaller than the splitting of outer supermodes (L1-L2 and L5–L4), as shown in Fig. 2.4(e5). In hexamers formed by 6 circular resonators some supermodes are degenerate, so that each uncoupled WGM splits into 4 supermodes, as illustrated in Fig. 2.4(f5). While this ring molecule gives the same number of spectral dips (four) as the linear chain of 4 resonators, the separation between the two central modes (L2+L3) is substantially larger than (L1–L2) and (L4 –L3), thus enabling distinction of the hexamer molecule from other molecules considered in Fig. 2.4. The fact that the degeneracy is not completely lifted in hexamer molecules (resulting in less observed modes than the total number of atoms N) can be viewed as a property of this configuration which can be used for identification purposes. Each photonic molecule with a particular configuration and symmetry has unique resonant properties that give rise to its distinct spectral signature. The spectral signature of quadrumers formed by 4 circular resonators (Fig. 2.4(d5)) is different from that of 4-sphere chains (Fig. 2.4(c5)) and 3-sphere chains (Fig. 2.4 (b5)). Therefore, we are able to identify the molecule configuration based on its spectrum, giving us the ability to potentially utilize such signatures for geometry or position sensing. We also observed that some of the coupled supermodes have much higher Q-factors compared to the uncoupled WGMs, as seen in Figs. 2.4(c4,d4,e4,f2). The Q-factor increase may relate to the symmetry of the molecule configuration that was reported before [261, 262]. Hence, the configuration could be designed for potential applications such as high order filters and multi-wavelength sensors [259]. It should be noted, however, that the optical transport and coupling process is more complicated in large 2-D molecules, which provide multiple propagation paths and coupling possibilities. As a result, the spectral signatures for large molecules can be rather complicated and, in addition, their spectral appearance can vary in different spectral ranges. Generally, the shape of spectral resonances can vary depending on the phase relationships in the system similar to Fano resonances. For these reasons, a reliable interpretation of supermodes requires inspection of the evolution of the spectral signature shape over long spectral ranges.

2.3. Spatial distribution of supermodes in photonic molecules

To better understand the coupling and transport properties of photonic molecules, we first calculated the Electric filed distribution (E-field) of bi-circular photonic molecule as a known case (Fig. 2.5) where two microresonators are in contact, and then for more complicated molecular structures we mapped the spatial distribution of electric field for each supermode, as presented in Fig. 2.6.

The simulations were performed for circular resonators with D = 7 µm and n = 1.59 in air, the same as in Figs. 2.4(a2-e2). The Electric filed maps in Fig. 2.5 for bi-circular resonator illustrate different mode distribution for shorter resonant wavelength (antibonding mode) compare to longer resonant wavelength (bonding mode). In fact, if two photonic atoms are initially far apart, they have identical position of resonant WGMs called uncoupled mode (the black dashed line in Fig. 2.5(a)). However, as the spacing between the two photonic atoms becomes smaller, they resonantly couple, and a typical mode splitting in the transmission spectrum form when photonic atoms combine into photonic molecule [58, 196] The mode splitting can be seen in the spectrum of Fig. 2.5 (a).

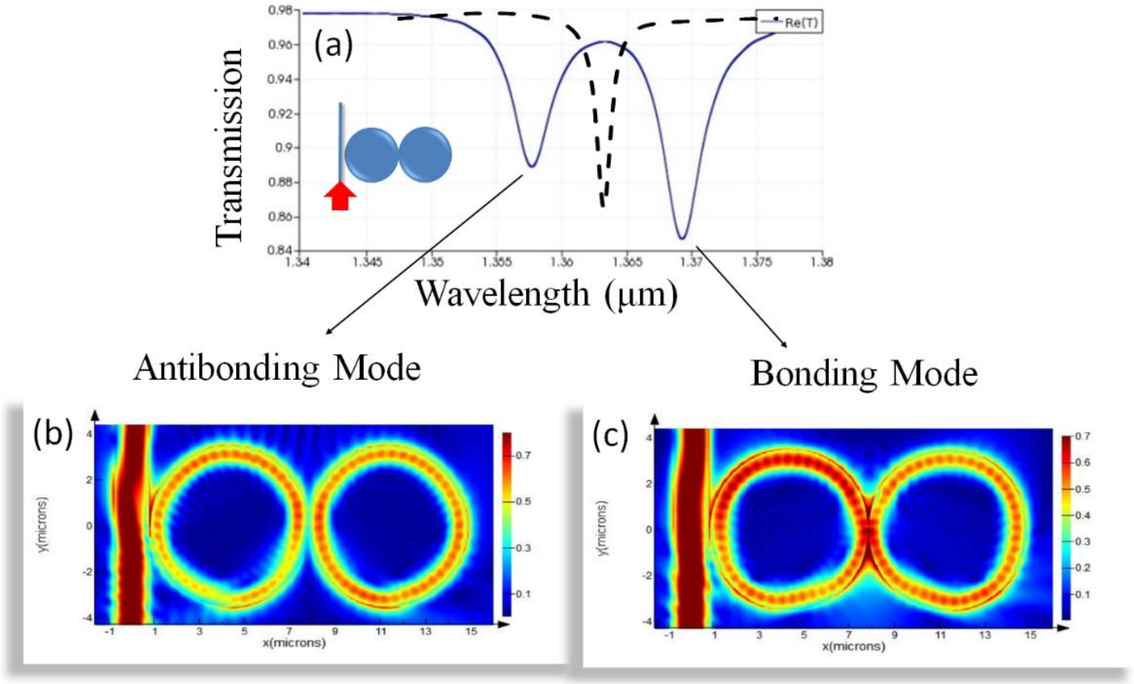

Figure 2. 5: Bi-circular photonic molecule modeling results for two identical 7 μm diameter circular resonator in contact with index of 1.59. (a) Mode splitting in transmission spectrum as two photonic atoms form the molecule. Electric field map corresponds to (b) antibonding and (c) bonding modes.

Antibonding molecular modes are normally higher in energy (shorter wavelength) than bonding molecular orbitals. The E-filed distribution of antibonding mode in Fig. 2.5(b) can be interpreted as a type of resonant mode that weakens the bond between two photonic atoms and helps to raise the energy of the photonic molecule relative to the separated atoms. The energy is determined by the effective index of refraction for a given optical mode. Larger the effective index of refraction smaller the energy is. As an example, in the case of bonding mode formed by two touching photonic atoms with high index of refraction, the electromagnetic field tend to concentrate near the contact region which has high effective index of refraction coming from the materials of photonic atoms. Consequently, the effective index for bonding mode is slightly higher than that uncoupled individual atoms. In contrast, in the case of antibonding mode, the effective index is slightly smaller due to a larger fraction of the mode contained in air. As a result, this mode is slightly shifted to higher energy compared to that in the photonic atoms. The density of E-filed is concentrated outside the bonding region. In contrast, the bonding modes are at a lower energy (longer wavelength) than the antibonding modes and tend to bound two photonic atoms through high concentration of E-filed shown in Fig. 2.5(b) as hot spots in the region between two photonic atoms where they are in touch.

More advanced photonic molecule configurations and their corresponding transmission spectra are shown in Figs. 2.6(a-d), where vertical lines indicate the position of uncoupled WGMs. Spatial E-field distribution was obtained by launching continuous wave (CW) source at each supermode eigen wavelength. Two interesting phenomena can be observed in the E-field map. Based on analogy with the well-known case of two identical strongly coupled circular resonators, the shortest and longest wavelength components can be called antibonding and bonding modes, respectively [58, 262]. For shortest wavelength, antibonding mode (Fig. 2.6(a1-c1)) the electric field appears to be distributed uniformly among all constituent atoms, which is not seen in other modes. The E-field is reduced at the points where the circular resonators touch which means that the coupling at these points is weakened. However, such antibonding modes seem to possess an additional coupling mechanism due to “leaky” modes propagating long distances along the peripheral area of the molecule. This phenomenon is especially noticeable in the hexamer molecule. As shown in Fig. 2.6(c1), the E-field standing waves present in the medium connecting adjacent resonators, constituting a large outer ring. These phenomena are related to the antibonding nature of such modes. The E-field is weak between two neighboring resonators due to their phase mismatch at the contact point, thus the light tunneling is less efficient. In the meanwhile, light scattered into the medium that is incident on the adjacent sphere at a grazing angle can be coupled outside the contact region, which may contribute significantly to the supermode coupling. As a result, relatively large fraction of the mode is present in the external medium leading to a smaller effective index for such antibonding mode, which results in its shortest wavelength position among all split components.

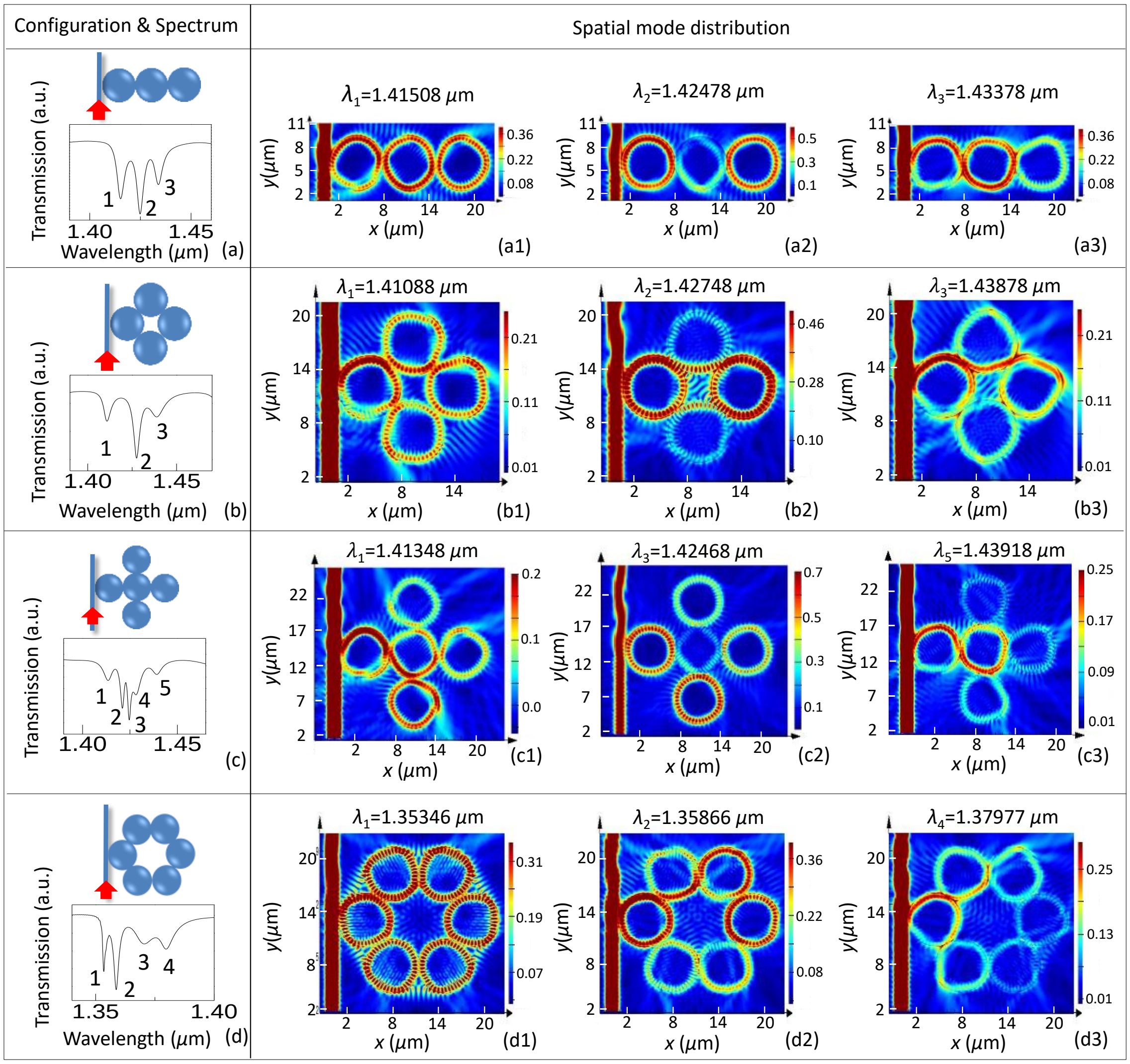

Figure 2. 6: EM field maps calculated for different molecules calculated at different supermodes: (a) linear chain formed by 3 circular resonators, (b) quadrumer, (c) 5-resonator cross and (d) hexamer. Simulated FEM field maps at three different supermode eigen wavelengths are presented for each molecule in (a1-a3), (b1-b3), and (c1-c3), respectively [263].

As seen in Fig. 2.4, this antibonding mode in hexamer molecule (Fig. 2.6(c1)) has much higher Q-factor compared to the uncoupled mode (Q increases from ~300 to ~1000). Similar Q-factor increase for some of the supermodes of symmetric photonic molecules was previously observed and studied as a function of the gaps between coupled resonators [261]. For bonding mode, in contrast, the E-field is better overlapped at the contact region adjacent to the point where two resonators touch due to improved phase matching. This factor provides more efficient evanescent side-coupling for WGMs in neighboring cavities. As one can see in Figs. 2.6(a3-c3), the intensity distribution indicates that light is more likely to tunnel to the adjacent resonator than to stay in the original one and circulate. Therefore, the light propagates through the entire molecule with a snaky path, tunneling at the contact point. The hexamer molecule is likely to operate in the over-coupled regime, due to the fact that bonding mode (Fig. 2.6(c3)) is broader and shallower and has lower Q-factor compared to the antibonding mode illustrated in Fig. 2.6(c1). For photonic molecule supermodes whose eigen wavelengths are close to the WGMs wavelengths of the constituting circular cavities, the E-field patterns inside individual resonators appear more perfect circular-shaped, as seen in Fig. 2.6(a2-c2), similar to the WGMs E-field map inside a single resonator. It is due to the fact that the phase conditions inside individual atoms are closer to their uncoupled WGMs which have perfect circular symmetry. If the supermode eigen wavelength is far away from that of the uncoupled mode, large phase mismatch will create the E-field maps inside such resonators which are far from perfect circles (left resonator in Figs. 2.6(a1,b1)) or distorted uncircular shapes (Figs. 2.6(b3,c3)).

It appears that light is forced to choose an optical path other than the perfect circle in order to maintain the phase matching condition. Previously, a similar effect was observed in size mismatched bi-spheres [180]. Another noticeable point in Figs. 2.6(a2) is that the E-field is concentrated in two side resonators, while the central one is almost dark. For linear chain this can be explained by the Bloch modes formation in the coupled molecule. Ref. [182] proved by calculations and demonstrated experimentally that among the three split modes in a coupled 3-sphere chain, the center mode is dominant for the first and the third resonators while the split-off modes showing more intensities in the central resonator. For 2-D molecules with a configuration different from the linear chain the coupling is more complicated, however, similar effects can be observed in Fig. 2.6(b2). Enhanced E-field is also observed in the central region enclosed by four resonators due to interference. The E-field enhancement seen at the center of quadrumer in Fig. 2.6(b2) and along the peripheral area of hexamer in Fig. 2.6(c1) is advantageous in sensing applications due to strong light-particle interaction in these regions [259], not limited to the surface of the resonator like in typical WGM-based sensors.

2.4: Sensing Single Nanoparticles by Two-Atom Molecules

As we discussed in in Section 2.1, one of the major motivations to study WGM resonators is related to their sensor applications [187-195]. In this work we concentrate on fundamental aspects of WGM hybridization effects in photonic molecules and the sensor applications are, generally, out-side the scope of this work, for more detailed discussion of these applications see reviews [187, 188]. We would like, however, to illustrate the potential advantages of coupled cavities over single resonators using a simplest two-atom photonic molecule. Previously, in Ref. [191] it was shown that by using two measurements of spectral shifts it is possible to discriminate between surface and volume index perturbations. However, it is also well known that the EM field of the bonding modes tends to concentrate in the regions adjacent to the contact points of the neighboring cavities. This means that if a nanoscale gap is created between two cavities, the EM field would be enhanced in this gap. Below we show that single particles placed in this gap can cause significantly larger spectral shifts of the bonding mode com-pared to similar spectral shifts of the uncoupled WGMs in single cavities.

For reference purposes, the single resonator case (D= 3 µm and n = 1.9) is illustrated in Fig. 2.7 for a single surface nanoparticle with the refractive index 1.9 and diameters 50, 75 and 100 nm. It is seen that the spectral shift of WGM resonance is hardly detectable be-cause of the poor overlap of such particles with the WGM evanescent field. In contrast, the same particles placed in the middle of the 100 nm gap separating two identical atoms cause easily measurable long-wavelength shift of the bonding mode, as shown in Fig. 2.8. The antibonding mode practically does not experience any shift because of its expulsion from the nanoscale gap region separating the cavities.

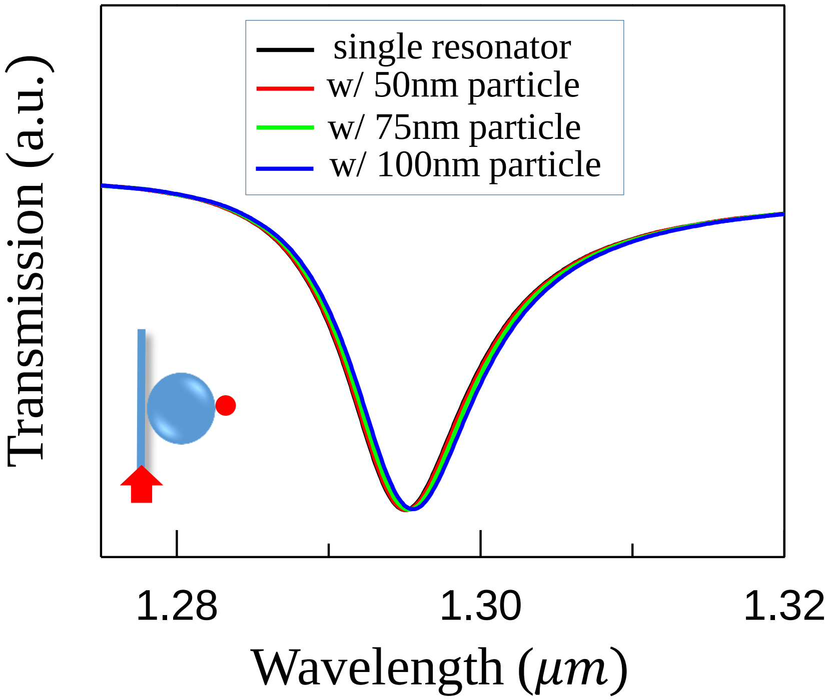

Figure 2. 7: Single nanoparticles with diameters 50, 75 and 100 nm are at the surface of a single resonator with D = 3µm and n = 1.9 [263].

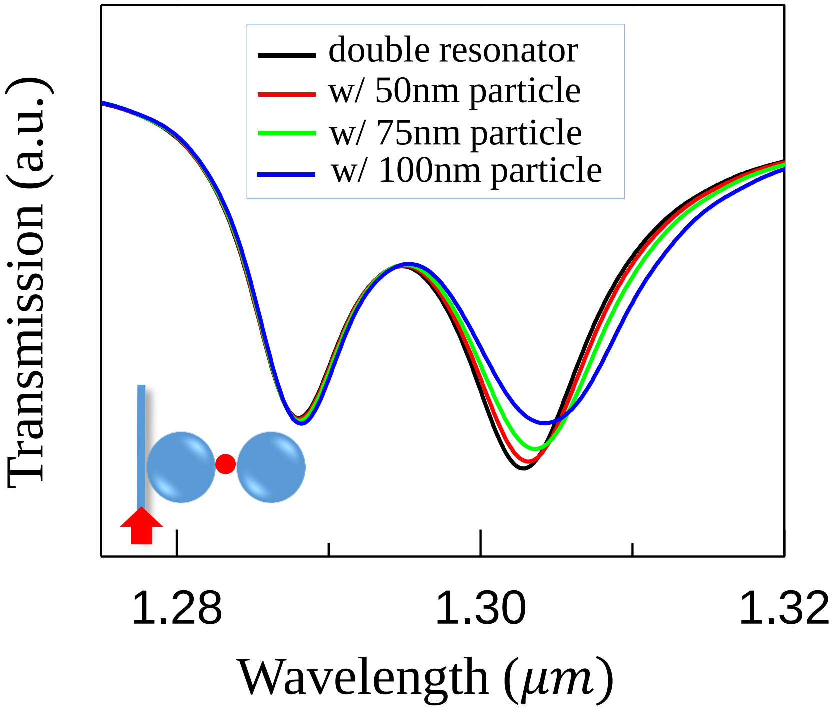

Figure 2. 8: Single nanoparticles with diameters 50, 75and 100 nm are in the middle of 100nm gap separating two identical resonators. The spectral shift of the bonding mode in this case markedly exceeds that in the case of Fig. 2.7 [263].

Another example illustrating the sensing capabilities of photonic molecule are shown in Fig. 2.9 for single resonator and the hexamer photonic molecule where the refractive index of the surrounding medium is varying.

In this example, we calculated the waveguide transmission spectra with the index of the medium increasing by 0.01 increments. The simulation parameters were selected to be exactly same as Fig. 2.7, and Fig.2.8.

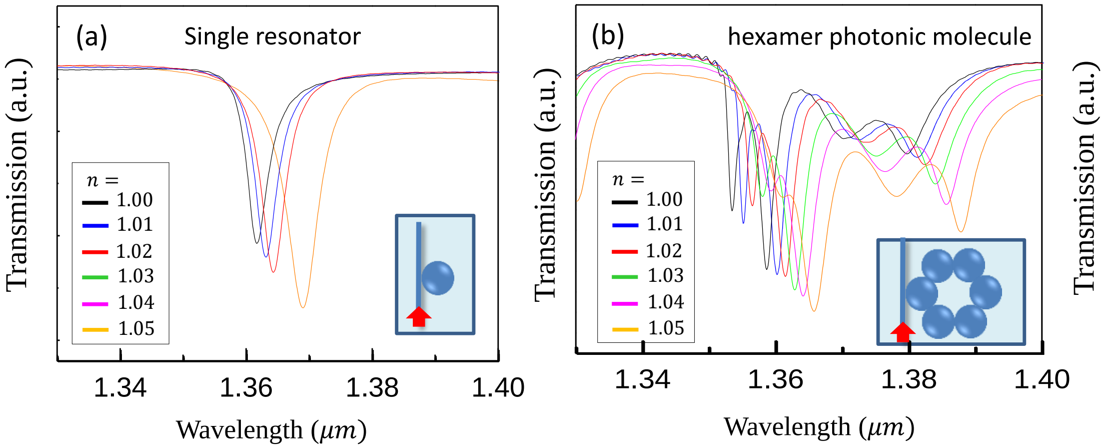

Figure 2. 9: Waveguide transmission spectra for (a) single resonator and (b) hexamer photonic molecule with the change of medium index.

As illustrated in Figs. 2.9 (a,b), the transmission spectra of both the single resonator and the hexamer photonic molecule show noticeable red-shift of the WGMs' dips with increasing medium index, and as a result demonstrating sensing capabilities. We also calculated resonance mode shift for both cases of single resonator and hexamer photonic molecule in Fig. 2.10. While the WG Mode 2 in Fig. 2.10 (c) for hexamer photonic molecule shows similar shift compared to the WGM of the single resonator, however, other WG modes including Mode 1, Mode 3, and Mode 4 in Fig. 2.10 (b), (d) and (e) respectively, display larger shift. The resonant mode shift is specifically pronounced for Mode 4, and it shows ~15% larger shift comparing to the resonant mode shift in single resonator.

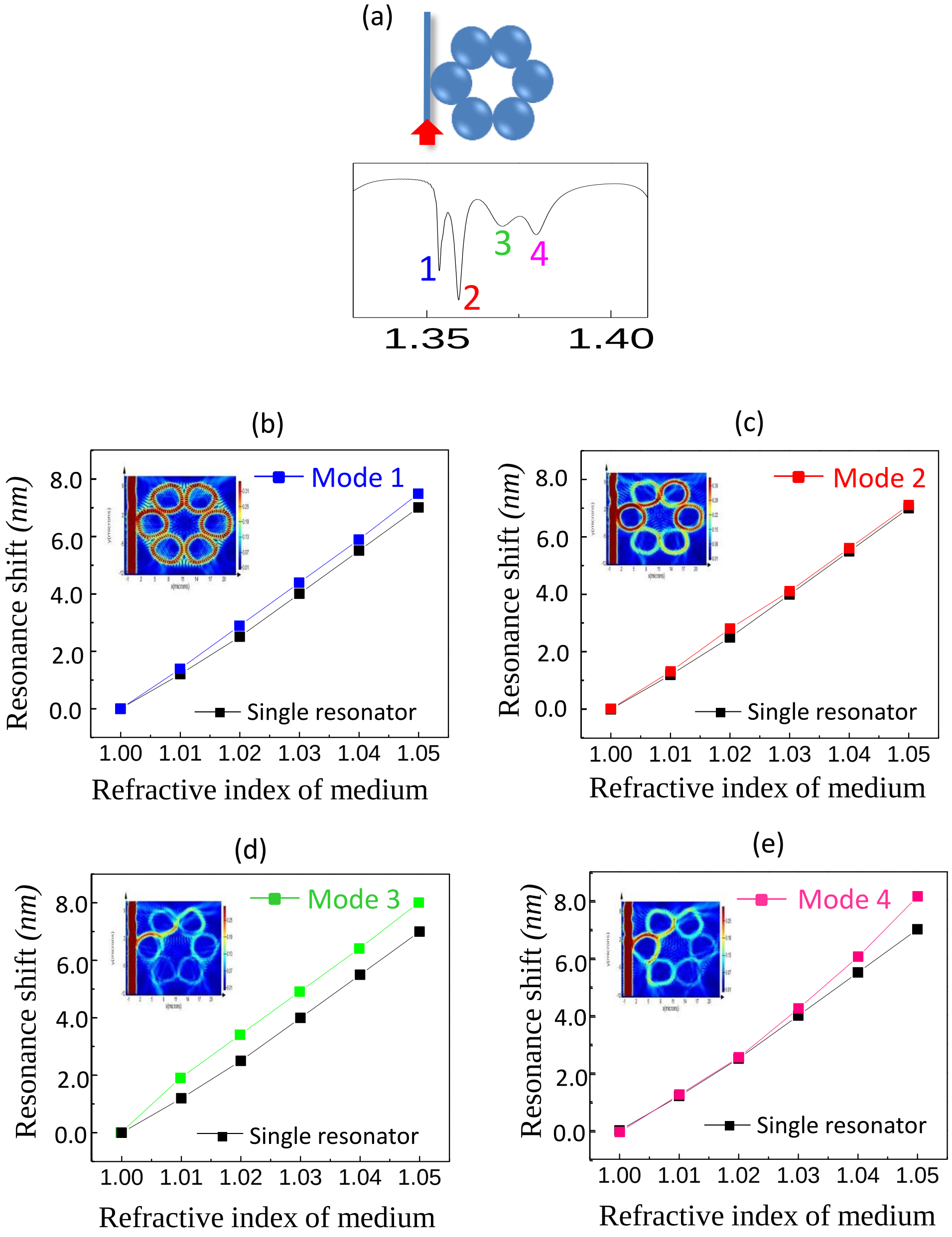

Figure 2. 10: Comparison of the resonance mode shift for the case of single resonator and hexamer photonic molecule with medium index perturbation. (a) geometry and simulated transmission spectra for hexamer molecule. (b-e) Resonant shift comparison for resonant mode in single atom, and supermodes in hexamer photonic molecule.

These examples show a significant potential of photonic molecules cavities for enhancing detectivity of the WGM sensors. However, developing such devices require resonators with identical positions of WGM resonances and sufficiently high Q-factors, typically Q>10^4, which are rather difficult to fabricate by conventional technologies.

2.5: Comparison Between Modeling Results and Experiment

The modeling study of resonant optical properties of photonic molecules in this dissertation was done in parallel with the experimental studies. Those extensive experimental works were included in the Ph.D. theses of Dr. Yangcheng Li, who graduated from Mesophotonics Lab in 2015 [205].

In this Section, we compare the simulation results with experimental results for different configuration of photonic molecules including 3-sphere chain, planar quadrumer, 5-sphere cross, and hexamer molecules, as shown in Figs. 2.11(b-e), respectively. First column (Figs. 2.11(a–e)) shows microscope images for the molecules assembled and brought in contact with the tapered fiber at their equatorial planes. The taper's contact positions were located by carefully adjusting the height while monitoring the spectra to find the largest mode splitting. Experimental fiber transmission spectra with side coupling to a single sphere as well as to various photonic molecules are presented in Figs. 2.11(a1–e1). The measurements were performed by a former Ph.D. student of the Mesophotonics Lab, Dr. Yangcheng Li [118]. It should be noted that in order to reliably determine the spectral signature, it was needed to record the transmission in a relatively wide spectral range.

Since the excitation was provided by unpolarized white light source, both TE and TM WGMs are present in the experimental spectra, as indicated in Fig. 2.11(a1). The full transmission spectrum is a superposition of coupled WGM TE and coupled WGM TM modes in a molecule. Correspondingly, the simulation was performed with both TE and TM polarized light sources and the results were combined, as shown in Figs. 2.11(a2–e2).

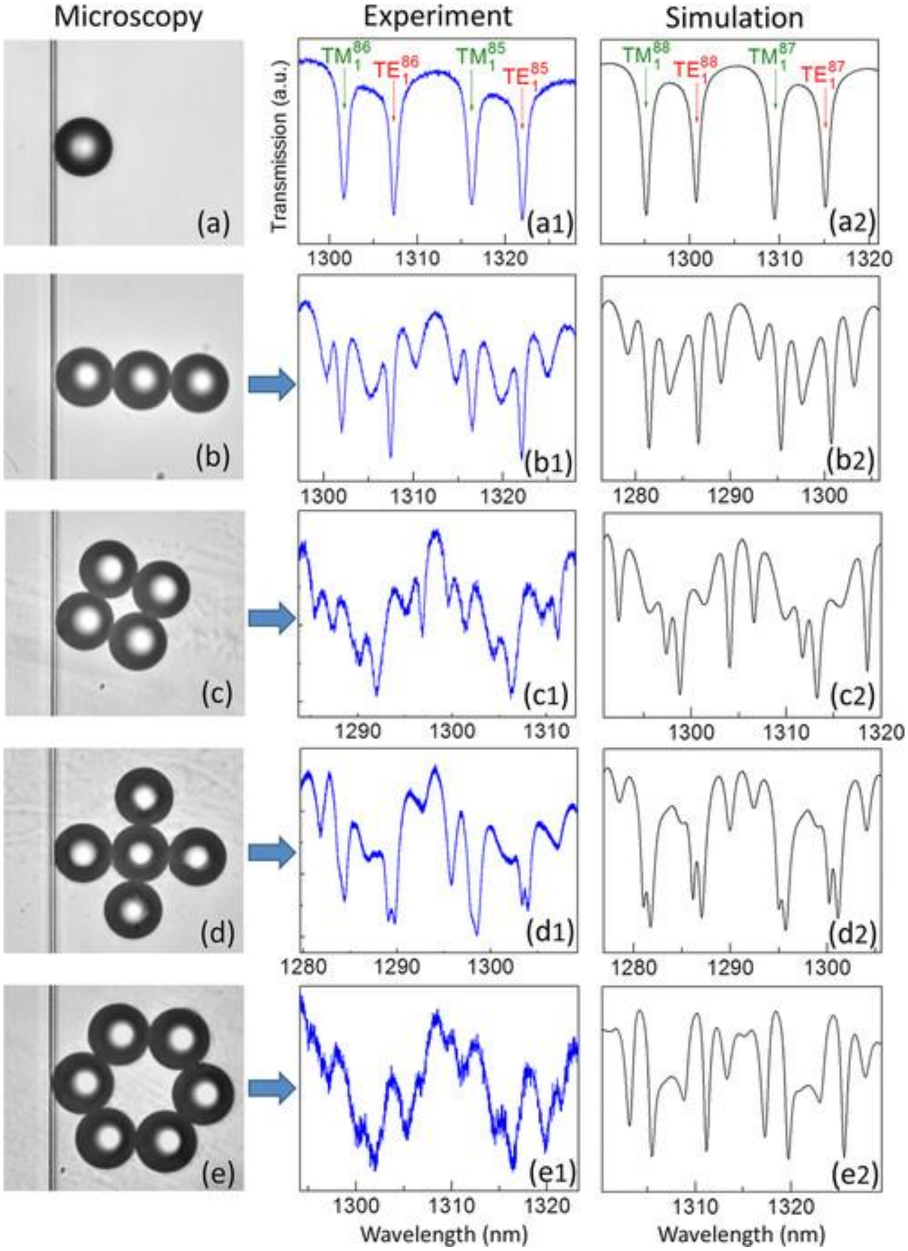

Figure 2. 11: Comparison between FDTD simulated and experimentally measured spectra for both 1-D chain and 2-D planar molecules. We acknowledge a contribution of former Ph.D. student of Mesophotonics Lab, Dr. Yangcheng Li, who performed the experimental measurements [118]. (a-e) Microscope images for various photonic molecules assembled with polystyrene microspheres of 25 μm diameter side-coupled to a tapered fiber with 1.5 μm waist diameter in water. (a1-e1) Measured and (a2-e2) simulated fiber transmission spectra for corresponding molecular configurations [263].

Both simulated and experimental spectra contain periodically repeated spectral signatures formed by TE and TM polarized WGM-defined features near 1300 nm. The results demonstrate very good agreement between experimentally measured and FDTD simulated spectra for both 1-D chain and 2-Dplanar molecules. The numbers of observed supermodes (dips) and their spectral positions match well in all cases. In cases represented in Figs. 2.11(b1–d1) not only the dip positions, but also the whole appearances of the experimental spectra are very similar to the calculations represented in Figs. 2.11(b2–d2), respectively. For hexagonal molecule shown in Fig. 2.9(e) the agreement of experiment (Fig. 2.11(e1)) with modeling (Fig. 2.11(e2)) is far from optimal that can be explained by difficulties of achieving reproducible WGM coupling conditions in more complicated configurations of coupled cavities. (The noise level is higher in this case compared to other cases). Despite the fact that the agreement is not perfect in all cases, the overall conclusion is that in most of the cases we demonstrated almost perfect agreement between measured and calculated fiber-transmission spectra. These results demonstrate experimental feasibility of photonic molecule assembling with high accuracy, and also provide strong support for our proposed concept of spectral signature identification discussed in Section 2.2.

2.6: Conclusion

In this Chapter of dissertation, we theoretically investigated the optical properties of photonic molecules consisting of coupled cavities with homogeneous WGM resonances. The main results and conclusions are listed below:

- The modeling of WGM processes in photonic molecules was developed based on using a commercial FDTD software Lumerical in a simplified 2-D geometry. The simulation was performed for identical circular resonators with identical dimensions and refractive index contrasts similar to that used in the experimental situations.
- The spectral properties of such photonic molecular structures were studied based on calculations of transmission spectra through the stripe waveguide side coupled to one of the resonators comprising a given molecule.
- We proposed the concept of spectral signature as a unique feature associated with each molecular configuration as a relatively stable property which allows distinguishing between different molecules based on their spectra. The number of split supermodes and their spectral positions were studied based on the side-coupled fiber transmission spectra for 1-D and 2-D molecules formed by multiple photonic atoms. Since we used the numerical methods we cannot claim that these “spectral features” or “spectral signatures” are universal characteristics of the given

molecules, but we tested that these features persist in their spectra in a certain relativity broad range of variation of parameters. Moreover, we demonstrated good agreement between the FDTD simulated and experimentally measured spectra for both 1-D chain and 2-D planar molecules.

- The spatial distribution of electromagnetic fields was calculated by selecting the resonant wavelengths or super modes excited such structures. It is shown that each such spatial configuration result in fiber transmission spectra which have a series of resonant features determined by the symmetry and the number of the constituting atoms. Interesting coupling and transport phenomena such as Bloch mode formation, non-circular field pattern formation, long-range coupling of WGMs confined in circular resonators through surrounding medium, and the features of resonant optical tunneling through coupled cavities were observed and discussed. Further fundamental study of phase matching and coupling properties may be required to give more rigorous explanations. In particular, the spectroscopic states of atoms and molecules corresponding to different symmetry functions are described by a part of the group theory known as a representation theory [264]. The lifting of degeneracy in different molecules with various symmetry properties can be explained from the point of view of representation theory, however this discussion goes beyond the scope of this Chapter.

- Along with the spectral signatures of photonic molecules, we study numerically the sensor capability of such structures and showed that they have an improved sensitivity compared to single photonic atoms in few certain carefully designed situations. The modeling indicated a tremendous potential of photonic molecules for developing sensor devices with improved sensitivity and functionality. In general, the E-field enhancement in the medium surrounding certain molecular configurations provides larger detecting volume and higher sensitivity comparing to typical WGM-based sensors of a single cavity. The functionality of WGM sensor devices can be extended in coupled-cavity structures. Some of these ideas have been expressed for weakly [189, 190] and strongly [191] coupled cavities. Photonic molecules also showed Q-factor enhancement for some of the antibonding modes and the mini-band formed by a series of overlapped supermodes. Therefore, the spectrum of the molecule can be engineered, providing additional freedom in design of lasing devices, narrow-line filters, delay lines and multi-wavelength sensors.

CHAPTER 3: RESONANT ROUTING AND ASYMMETRIC TRANSMISSION PROPERTIES OF COUPLED-CAVITY STRUCTURES: DESIGN AND ANALYSIS

3.1: Introduction to the optical transport properties of coupled-cavity structures

Compact integrated optical microresonator devices can be viewed as one of the most versatile platform for applications such as optical modulation, switching, and routing of a signal, and so for wavelength division multiplexing and unidirectional transmission functionalities. Description of such microresonator coupled to waveguides as well as coupled resonators of photonic molecules can be explained often based on the simplistic approximation of single mode phase matched excitation of whispering gallery modes (WGMs) and *k*-vector conservation with an optimal coupling efficiency [65, 73, 265, 266]. In this approach, it is assumed there is only traveling single modes in different components of the structure which are coupled via phenomenological coupling coefficients and the power flows continuously in only one direction inside the microresonator [218, 219, 261, 267]. The general justification for this approach is that the effective length of couplers should be many wavelengths long in order to have efficient coupling [72, 266]. In this regard, the coupling spatially decreases with Gaussian dependency away from the minimum separation point along the length of couplers, and drops off exponentially with the square of difference in propagation constant between the stripe-waveguide and microresonator modes [72].

Stripe-waveguides allow single mode phase matched excitation of WGMs with a high coupling efficiency to be formed and provide the excitation of traveling clockwise or counter clockwise of WGMs in circular microresonator. Likewise, in multi-port structures, the ports can be connected in a certain way determined by the direction of circulation based on a simple coupled mode theory for a modal coupling in circular cavities [268-271].

In this Chapter of dissertation, we study transmission properties of side-coupled cavity systems in the case of high refractive components where all circular resonators are much more compact, and the effective length of coupler became comparable with the wavelength of light (λ). This is in contrast with the well-known case of large microresonators with modest refractive contrast, and long effective length of coupler (several wavelengths).

3.1.1. Coupling properties of compact high-index microresonators as opposed to large low-index resonators

In this introductory Section 3.1, we first illustrate a qualitatively different behavior of high- contrast couplers from their low-contrast counterparts using a simplest example of a single circular microresonator placed between two stripe-waveguides, as it illustrated in Fig. 3.1. In this example, we also would like to illustrate an important role played by asymmetric gaps between the stripe-waveguides and circular resonator in the asymmetric optical transmission properties of such systems related to their mode conversion properties.

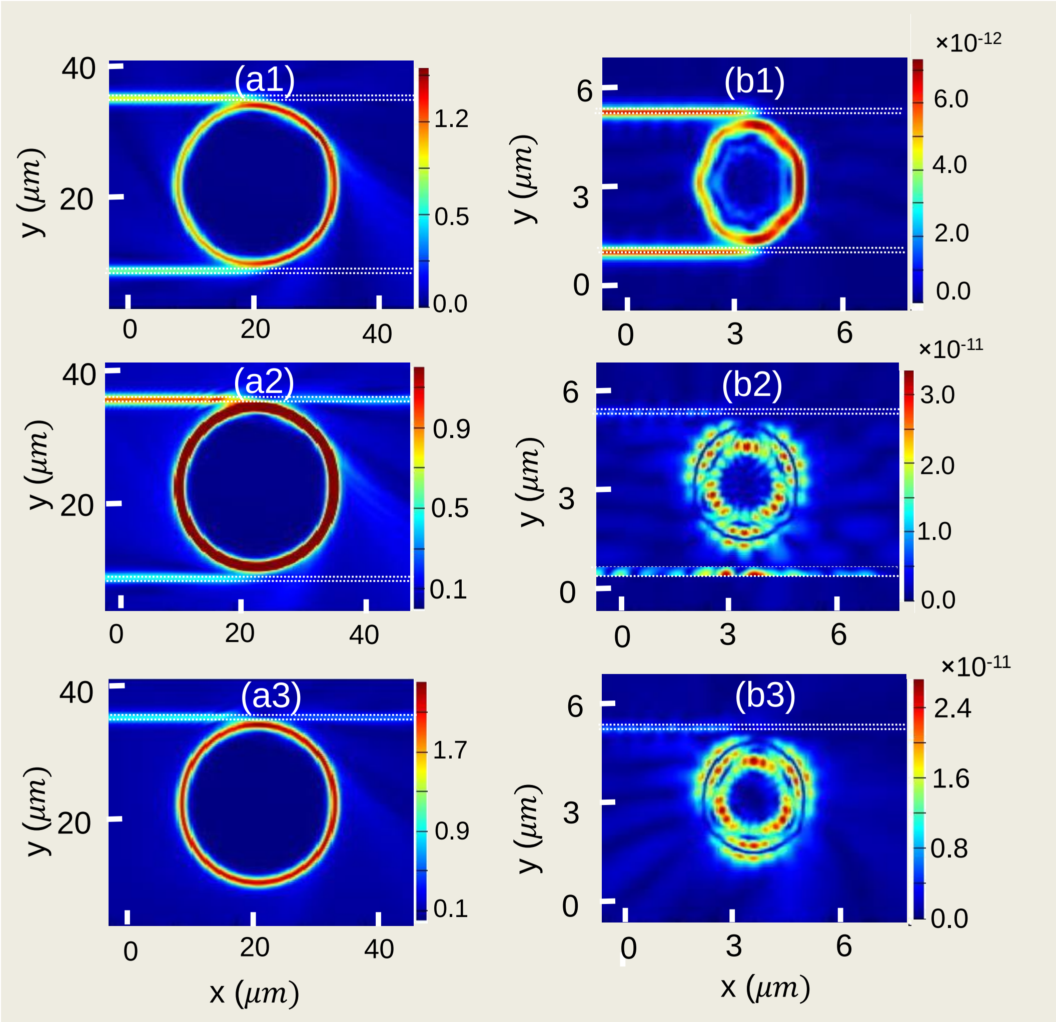

Figure3. 1Figure 3.1: Electric field distribution for the circular microresonator of (a) 25 μm with refractive index of n=1.59 immersed in water and, (b) 3 μm high refract n=3.4 in air. The indices 1, 2 and 3 in each case represent $g_2 = g_1$, $g_2 > g_1$ and, $g_2 = \infty$ respectively.

The right column in Fig. 3.1 shows the modeling results for spatial distribution of electric field (E-field) at the resonance wavelength (around λ= 1.45 μm) for the case of 25 μm circular microresonator with refractive index of n=1.59 immersed in water which is side coupled with two stripe-waveguides with separations g_1 and g_2. We also introduced the spatial asymmetry by increasing g_2, and keeping g_1 in Figs. 3.1a-3.1c. The single mode approximation can be applied in this case leading to formation of WGM circulating in one direction. The single mode in the upper waveguide is coupled to the circular resonator, circulates and then coupled to the lower waveguide. Since, the electric field map shown in this figure represents a steady state response of the system in the frequency domain. This steady state field map obtained because of time averaging displays a uniform red color in the right part of the ring representing traveling wave (Fig 3.1(a1)). Excitation of traveling wave is also predictable for the case of $g_2 > g_1$ in Fig. 3.1(a2); There is less fraction of power coupled in the lower Stripe waveguide because of the larger gap, g_2. In the last case, Fig. 3.1(a3), g_2 become infinite which means the absence of lower stripe-waveguide. Not surprisingly, the field map still shows the presence of traveling wave in the system in this case. However, in contrast to the traveling wave patterns observed for big 25 μm circular microresonator, the field maps for small (3 μm) microresonators in Figs. 3.1(b2-b3) show a standing wave resonance field inside the cavity. In this case, in order to keep the same quality factor as one in Figs. 3.1(a1-a3), we increased the refractive index contrast of microresonator (n=3.4 in air) as well. From the first sight, the electric field map for the small microresonator demonstrates very similar behavior of traveling wave as the right column but just for the symmetric case when $g_2 = g_1$in Fig. 3.1(b1). However, for the asymmetric structures in Figs. 3.1(b2, b3), the electric field map shows pronounce maxima and minima representing standing wave. Most interestingly, the direction of the electromagnetic flux in the receiving stripe waveguide does not follow a simple k-vector conservation rule. Depending on the parameters of the system it can be coupled to left or right port in the receiving waveguide. This opens a possibility for developing a connectivity between ports which is not dictated by the k-vector conservation law.

In fact, the single mode approximation Ref. [272-274] cannot be applied to sufficiently high refractive index small microresonators. In these compact structures, the effective length of coupler became comparable with wavelength. High degree of localization in space means a delocalization in *k*-space, which means that the *k*-vector conservation law requirements are relieved in such structures with compact high-index microresonators. In this situation, both clock wise and counter clock wise modes can be excited inside the micro resonator which leads to formation of standing wave mode pattern, as illustrated in Figs. 3.1(b2-b3).

3.1.2. Role of mode conversion and connection to non-reciprocal and unidirectional optical transport properties

Another area where similar processes have been studied is related to very popular field of non-reciprocity and unidirectional optical transport in coupled-cavity structures. The test of reciprocity is based on switching the input and output; however, it should be noted that it is important to trace in a backward direction the same mode which reached the output port of the system in a forward direction. This is an especially important for structures which provide the conversion of the modes. In Fig. 3.2, this situation is exemplified by a structure containing: a) converter from asymmetric (A) to symmetric (S) mode and b) mirror for the asymmetric (A) mode which is perfectly transmitting for a symmetric (S) mode [275, 276]. As schematically illustrated in Fig. 3.2(a), an antisymmetric (A) mode launched in the system from left to right is converted into a symmetric (S) mode and it is transmitted through the mirror. At the same time, an A-mode incident on the mirror from the right is reflected. The first impression is that this structure operates as an "optical diode". However, tracing in a backward direction the same mode (S) which reached the output port in the forward direction (Fig. 3.2(c)), shows that this mode propagates in a backward direction which follows the general theorem of reciprocity known in optoelectronics for linear systems [277]. For such systems, the matrix of reflection and transmission (R-T) coefficients for properly normalized amplitudes is symmetric that conform to power conservation and time reversibility for wave fields. At the same time, this example shows that for the same mode in forward and backward direction (as an example, launching A-mode from left to right and the same A-mode from right to left) the systems with mode conversion properties can display asymmetric transmission properties. Such asymmetric transmission can be used in a various applications based on their different transmission properties for modes with various symmetry properties [278, 279].

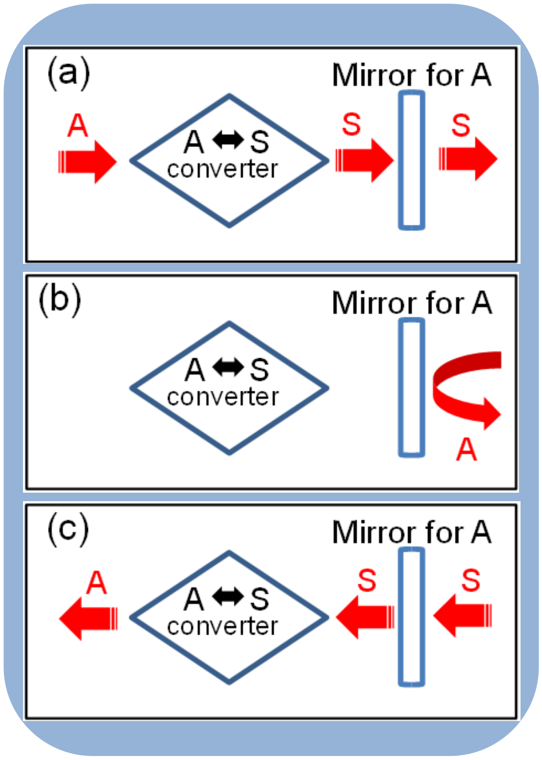

Figure3. 2: Example of a structure containing asymmetric (A) to symmetric (S) mode converter and a mirror for A mode [275]. (a) The structure transmits A-mode incident from the left, (b) reflects A-mode incident from the right, and (c) transmits S-mode incident from the right.

Thus, this example shows that in structures with mode conversion the optical asymmetry can be easily obtained if exactly the same mode (A in this example) is coupled in forward and backward direction. However, this does not mean that such structures possess the optical non-reciprocity. The structures considered in this Chapter possess strong mode conversion properties. It is seen in Figs. 3.1(b2,b3) that the single-mode input and output waveguides are coupled to standing WGMs in circular resonator which have the radial number equal to two – two maxima along radial direction can be seen. Thus, the asymmetric transmission properties between any two ports in such structures can be expected, but it does not mean that these structures are non-reciprocal.

The design of such structures can be additionally complicated by introducing the optical losses. In Ref. [280] the role of losses has been demonstrated for microcavity polaritons confined in planar semiconductor microcavities coupled through the central Bragg mirror. The absorption of light was provided by the quantum wells which were grown in only one cavity that resulted in strongly asymmetric resonant transmission properties for two opposite directions of light propagation [280].

To keep our discussion on more general level, we would like to note that the true non-reciprocity can be achieved in the Faraday isolators [83, 97, 281, 282] and in the nonlinear devices [106, 283]. Another approach is based on parity-time (PT) symmetry breaking in coupled resonator structures [250, 284, 285] due to a complicated interplay between the loss and gain in such structures. In systems represented by symmetric scattering matrix, the reciprocity is preserved in the presence of linear dissipation [275].

3.2. Parameters describing routing of light between in coupled-cavity structures

In this chapter, we provide a qualitative picture of this essential physics process and study transmission properties of very compact high refractive side-coupled cavity systems where we deliberately introduce the spatial asymmetry by using different separations g_1 and g_2 between the stripe-waveguides (WG) and circular resonator. The system incorporates four ports represented by the terminations of two side-coupled stripe-waveguides. Such systems can be viewed as another example of structures with the mode converting properties since the optical connectivity between the ports is provided due to a coupling from a single-mode stripe-WG to standing WGMs in a circular resonator, and to another single-mode stripe-WG. In addition, the structure is strongly asymmetric and lossy that can contribute to asymmetric transmission properties.

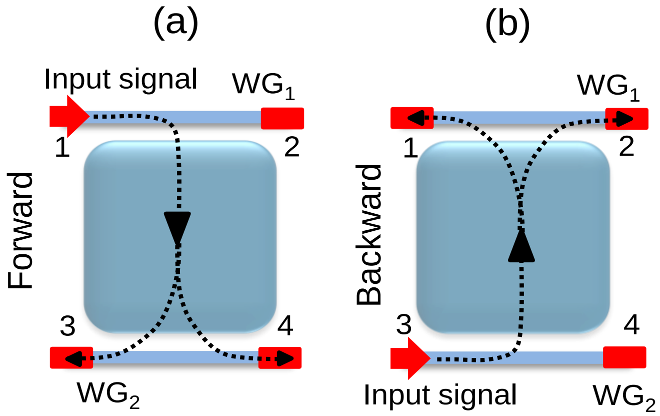

Figure3. 3: Schematic representation of 4-port optical system with asymmetric transmission properties. The light can be coupled into the optical system through two stripe-waveguides WG_1 and WG_2. Dashed lines indicate schematically the light propagation directions. The input and output ports are shown as a red arrow and red blocks respectively. For the forward direction in (a), Port 1 is considered as an input port to couple the light into the system. The propagation can be provided into Ports 2, 3 and 4. For the backward direction in (b), Port 3 is considered as an input port, and Ports 1, 2 and 4 are the output ports.

The modeling is performed for two-dimensional (2-D) systems that allow simplifying the calculations and retaining the essential physical properties. Our preliminary results can be found in Ref [109, 286, 287]. The strength of coupling depends on the separations, g_1 and g_2, and on the spatial overlap of the modes in stripe-WG and in circular resonator. The situation becomes especially interesting if instead of a single resonator we use two or more side-coupled circular resonators forming so-called photonic molecules [58, 288]. The coupled WGMs in photonic molecules form hybridized modes with various spatial distribution, so-called bonding and antibonding coupled modes. These modes have different spatial overlap with the modes in stripe-WGs. A combination of mode conversion properties with the strong asymmetry and strong losses gives rise to asymmetric transmission properties.

The asymmetry of the optical transport between any two ports *i* and *j* in such system (Fig. 3.3) is characterized with an isolation ratio (IR), which is defined using Eq. (1) below, where T_{ij}, and T_{ji} are normalized transmitted signals in the forward and backward directions between ports *i* and *j*. In Eq. (1) we assumed that the same mode is launched if forward and backward directions. In forward direction, we couple the input signal through Port 1 and detect the transmitted signals in Ports 2, 3 and 4, as illustrated in Fig. 3.3(a). Of particular interest for us is a ratio of the intensities (T_{13}/T_{14}) of the transmitted peaks in the left (Port 3) and right (Port 4) ports. The corresponding ratio measured in dB is represented by Eq. (2). In the backward direction, we determine the ratio of the intensities (T_{13}/T_{14}) of the transmitted peaks in the left (Port 1) and right (Port 2) ports.

$$IR(\lambda) = 10 \times log_{10}\left(\frac{T_{ij}(\lambda)}{T_{ji}(\lambda)}\right) \tag{1}$$

$$PR(\lambda) = 10 \times log_{10}\left(\frac{T_{13}(\lambda)}{T_{14}(\lambda)}\right) \tag{2}$$

The isolation ratio, generally, characterizes the asymmetry of the optical transmission in the system along a given path. The path ratio represents different efficiencies of various paths in such coupled-cavity networks. We begin with the case of a single microresonator. Using typical parameters of semiconductor structures, we show that the asymmetrical gaps with g_2/g_1=6 can result in IR~9 dB. After that, we switch to a double microresonator case and show that the same gaps ratio can result in IR of ~22 dB and ~11 dB for bonding and antibonding modes, respectively, which shows that much stronger IR factors can be achieved in photonic molecules compared to the case of single resonator. We also show that different wavelengths can be resonantly routed to different ports in the former (photonic molecules) case. Our results show that the path ratio difference around 12 dB can be realized between bonding and antibonding modes in optimized configuration. To analyze the underlying electromagnetic coupling properties for the asymmetric photonic molecule, we also calculated the spatial distribution of electric field (E-field) for each coupled mode in the case of double microresonator. Furthermore, we verified the asymmetric optical transmission and routing properties in our side-coupled-cavity structures by studying the dependence of these properties on the gap ratio (g_2/g_1) for different materials as well as for different sizes of microresonators in both cases of single and double resonator structures.

3.3: Single microcavity router

To demonstrate the asymmetric transmission properties, we modeled a single circular microresonator, MR_1, with the refractive index (n=3.18) matching that for indium phosphide (InP) and diameter (D=3 μm). We used two side-coupled waveguides, WG_1 and WG_2, with the 200 nm width and the same refractive index of microresonator (n=3.18). As illustrated in the insets of the Fig. 3.4, they were separated from the circular microresonator with uneven gaps, g_1=100 nm and g_2=600 nm, respectively. The numerical simulation was performed by finite-difference time-domain (FDTD) method with commercial software by Lumerical. A Gaussian modulated pulse of ~10 femtoseconds width with the 1450 nm center wavelength was launched into Port 1 for "forward" (T_{13}) and into Port 3 for "backward" (T_{31}) propagation directions. The electric vector of electromagnetic waves was linearly polarized in the plane of schematic drawings in the insets of Fig. 3.4 that corresponds to a TM polarization of a single-mode WG in the wavelength range of 1.4-1.5 μm [5]. The E-field transmitted through different ports was calculated as a function of time, and the broadband transmission spectra were obtained using Fourier transform. A computational grid with the maximum mesh element size of $\lambda/24$ is used to cover the entire simulation region.

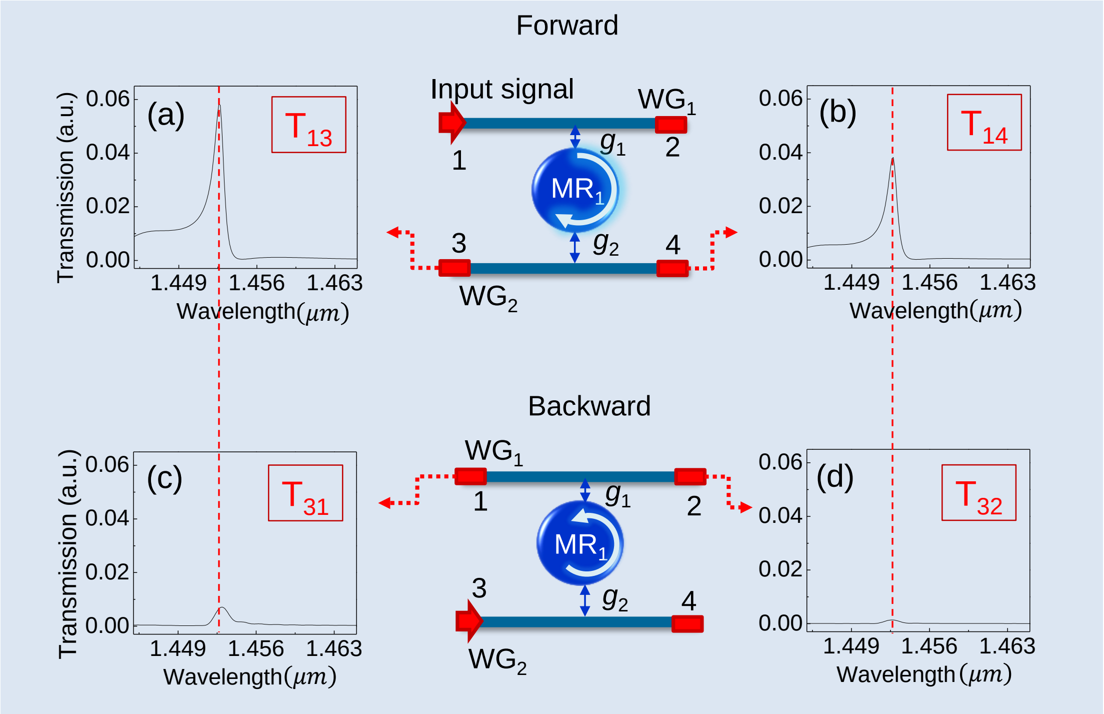

Figure3. 4: Insets illustrate a single microresonator, MR$_1$, with refractive index of n=3.18 (corresponding to indium phosphide) and 3 μm diameter. The side-coupling to WGMs in the micro-resonator is provided through the Stripe waveguides WG$_1$ and WG$_2$. The gaps g_1 and g_2 between the micro-resonator and the waveguides are 100 nm and 600 nm, respectively ($g_2/g_1 = 6$). The propagation paths in a forward direction are from Port 1 to Ports 3 and 4. The propagation paths in a backward direction are from Port 3 to Ports 1 and 2. (a,b) Normalized transmission spectra calculated in the forward direction from Port 1 to Port 3 (T_3) and Port 4 (T_4), respectively. (c,d) Normalized transmission spectra calculated in backward direction from Port 3 to Port 1 (T_1) and Port 2 (T_2), respectively. The calculation shows the isolation ratio around 9 dB at the WGM wavelength λ=1.4526 μm between Ports 3 and 1: $IR(\lambda) = 10 \times log_{10}\left(\frac{T_3}{T_1}\right) \sim 9\, dB$.

We should comment from the beginning that due to high index and compact size of our resonator, the effective length of the coupling regions between the circular resonator and stripe-waveguides is rather short in geometries considered in this work. This results in a significant backscattering, so that not only clockwise, but also anticlockwise WGMs are formed. At the same time, the optical coupling losses can be significant. A resonant buildup of standing WGMs shows that the light coupled though Port 1 can reach both Ports 3 and 4 under resonant conditions. The transmission spectra presented in Fig. 3.4 show that the path ratio (between T_{13} andT_{14}) is rather close to unity at the peak of transmitted power, λ=1.4526 μm, in the forward direction, $PR(\lambda)$ ~1.7 dB. However, the optical transport in backward direction, T_{31} and $T_{32,}$ under resonant condition, has significantly higher path ratio T_{31}/T_{32} A likely explanation of this behavior is related to more efficient excitation of counterclockwise WGM compared to its clockwise counterpart as a result of coupling through significantly larger gap g_2=600 nm. Comparison of magnitudes of resonant transmission peaks in Figs. 3.4(c) and 3.4(d) shows that the path ratio increases to ~6.5 dB. However, the magnitudes of the transmission peaks are found to be reduced in a backward direction compared to that in the forward direction. We compared the transmissions in forward and backward directions along different paths. We found that IR parameters significantly vary along different paths. For the path from Port 1 to Port 4, IR~15 dB, whereas for the path from Port 1 to Port 3, IR~9 dB.

To better understand the temporal behavior of the transmitted signals, we calculated the E-field amplitude transmitted in forward and backward directions as a function of time. Such comparison in presented in Figs. 3.5(a) and 5(b) for E-field transmitted from Port 1 to Port 3 in a forward (E_{13}) and backward (E_{31}) directions, respectively. The input pulse shown in red has the peak amplitude of 1 V/m. The transmitted pulse train with decaying amplitude is shown using blue color. The pulse train takes place due to trapping light in MR$_1$ leading to periodical coupling into the output WG. The amplitudes of the transmitted signals are significantly smaller than the amplitude of the incident pulse. Comparing the E-field transmitted in the forward direction (E_{13}) and backward (E_{31}) directions in Figs. 3.4(e) and 4(f), respectively, one can see that $\left(\frac{E_{13}}{E_{31}}\right)^2 \sim \frac{T_{13}}{T_{31}} \sim 9$ at the resonance wavelength λ=1.4526 μm, which agrees well with IR~9 dB calculated due to comparing corresponding transmission spectral peaks in Figs. 3.4(a) and 3.4(c).

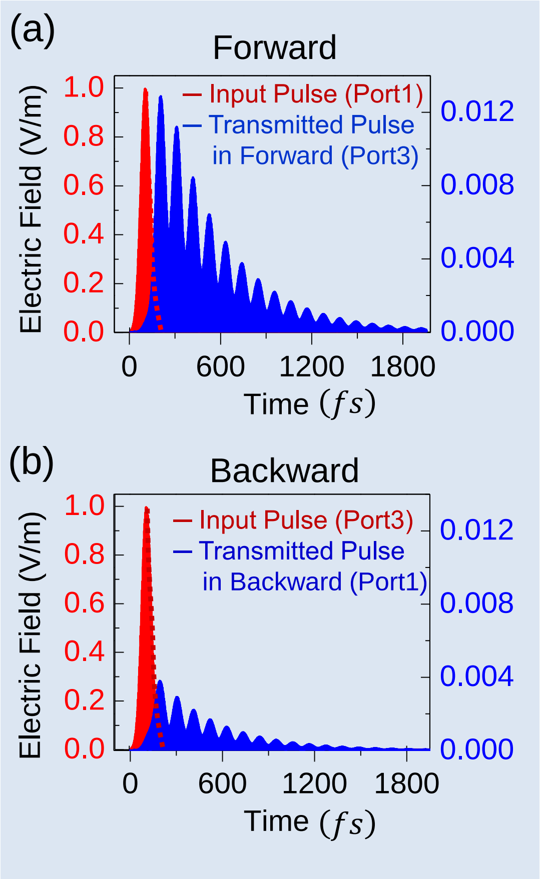

Figure3. 5: E-field vs. time for the single input pulse (red area) and transmitted pulse train with gradually decaying amplitude (blue area). The amplitudes of the transmitted signals are significantly smaller than the amplitude of the incident pulse and they can be read along the right vertical axis.

3.4: Double microcavity router

The functionality and performance of similar structures can be significantly extended by using multiple coupled resonators between two stripe-WGs. We modeled a system of two identical 3 μm diameter coupled circular microresonators, MR_1 and MR_2, as illustrated in the insets of Fig. 3.6. We kept the same gap ratio of $g_2/g_1 = 6$ controlling a degree of spatial asymmetry as in the case of single microresonator presented in Fig. 3.4.

Additional parameter, the gap (g) between the two circular microresonators was selected to be 100 nm. This is a small separation which results in formation of hybridized molecular states termed bonding (B) and antibonding (A) modes due to strong coupling between WGMs in adjacent resonators. These modes can be identified in the transmission spectra (T_{12}) in the forward direction due to two narrow dips illustrated in Fig. 3.6(a). (In the case of single microcavity router in Fig. 3.4, the corresponding spectrum at Port 2 contains a single dip. This case is not illustrated in Fig. 3.4.) The strong coupling regime is evident from the amount of splitting about 4.7 nm in Fig. 3.6(a) which exceeds the characteristic widths of individual WGM resonances by almost an order of magnitude. The choice of gap g_1=100 nm between the upper WG_1 and the edge of the photonic molecule is determined by the fact that it results in deep spectral dips in Fig. 3.6(a) due to critical coupling between WG_1 and photonic molecule at the supermodes' (B and A) wavelengths. The gap g_2=600 nm between the bottom tip of photonic molecule and lower WG_2 resulted in their under-coupling at the supermodes' wavelengths.

We checked that the splitting of the B and A states can be reduced by increasing the inter-resonator gap g, however this splitting as well as the positions and widths of the WGM-defined peaks are not strongly dependent on the gap sizes g_1 and g_2 separating the photonic molecule from the stripe-WGs in the limit of g_1, g_2 ≥100 nm. The behavior of two identical coupled resonators can be viewed in terms of avoiding crossing of their levels and exceptional points associated with symmetry breaking for PT-symmetric Hamiltonians [289], where a great number of experiments have been performed, particularly in optics [250, 284, 285]. If two microresonators are not identical, the coupling of modes with avoided frequency crossing scenario makes possible switching of electromagnetic (EM) field intensity between two circular microresonators [290]. To realize such switching in practice, carrier-induced refractive index tuning of one of the microresonators induced by non-uniform pumping can be used. These possibilities show a tremendous potential of such structures for achieving an ultrafast switching, routing and wavelength demultiplexing based on the design principles proposed in this chapter of dissertation. However, we will limit our consideration with identical microresonators, MR_1 and MR_2. We will show that the influence of the spatial configuration of EM fields inside the photonic molecule can be quite dramatic for the connectivity of different ports in 4-port systems considered in this work.

As illustrated in Figs. 3.6(b) and 3.6(c), the propagation in a forward direction from Port 1 is characterized with a marked path ratio favoring coupling to Port 3 (T_{13}) at the wavelength of B mode (1457.8 nm) and to Port 4 (T_{14}) at the wavelength of A mode (1453.2 nm). Using Eq. (2), PR at the wavelength of A mode (T_{13} /T_{14}) can be estimated as ~ -5 dB, whereas PR at the wavelength of B mode is about 7 dB, both in forward direction.

As illustrated in Figs. 3.6(e) and 3.6(f), the propagation in the backward direction (T$_{41}$ and T$_{42}$) from Port 4 strongly favors coupling to Port 1 (compared to Port 2) at the wavelength of A mode with the corresponding PR~14 dB. The efficiency of the optical transport in a backward direction is greatly reduced at the wavelength of B mode.

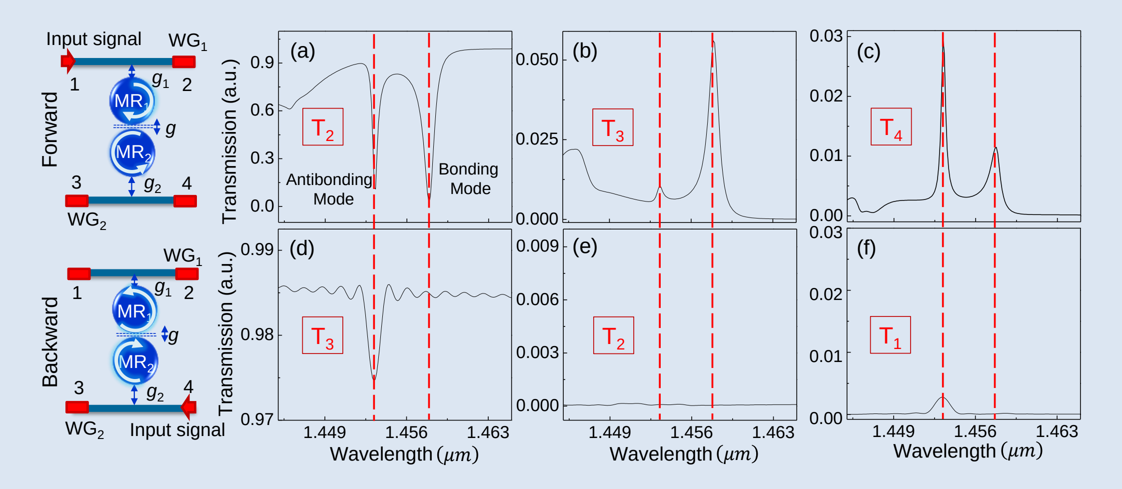

Figure3. 6: Insets illustrate double microresonator, MR$_1$ and MR$_2$, with the same index of n=3.18 (corresponding to indium phosphide) and 3 μm diameter. The side-coupling to WGMs in the micro-resonator is provided through the Stripe-waveguides WG$_1$ and WG$_2$. The gaps g_1 and g_2 between the microresonator and the waveguides are 100 nm and 600 nm, respectively ($g_2/g_1 = 6$). The gap g between the circular resonators is 100 nm resulting in a strong coupling between WGMs. This leads to a formation of bonding and antibonding photonic molecular modes. The forward direction is from Port 1 to Ports 3 and 4. The backward direction is from Port 4 to Ports 1 and 2. (a,b,c) Normalized transmission spectra calculated in forward direction from Port 1 to Port 2 (T_2), Port 3 (T_3), and Port 4 (T_4), respectively. (d,e,f) Normalized transmission spectra calculated in backward direction from Port 4 to Port 3 (T_3), Port 1 (T_1), and Port 2 (T_2), respectively.

In double microcavity the isolation ratio depends not only on the path, but also on the specific resonant wavelength corresponding to B or A resonant modes. The results presented in Fig. 3.6 are obtained for the same gap ratio, $g_2/g_1 = 6$, as in the case of a single microresonator represented in Fig. 3.4. For the path from Port 1 to Port 4, we estimate IR~22 dB at the wavelength of B mode, and IR~11 dB at the wavelength of A mode, which are significantly larger ratios compared to that in the single resonator case. This result is explained by stronger suppression of the optical transport in a backward direction in the double microresonator compared to single resonator case.

An interesting feature is that B and A modes tend to select different paths in our 4-port structure. This can be seen in the forward direction where the B mode tends to be more efficiently coupled into Port 3 (Fig. 3.6(b)), while the A mode tends to be more efficiently coupled into Port 4 (Fig. 3.6(c)). In this situation, the system operates similar to an optical demultiplexer [291, 292].

3.5: Asymmetric transmission as a function of the spatial asymmetry ($g_2/g_1>1$)

Different peak intensities of pulses transmitted in forward and backward directions along the same path were observed in a situation with strongly asymmetric gaps, $g_2/g_1 = 6$. Various efficiencies of different paths were also studied for the same situation. It is interesting to study how these properties depend on the parameter g_2/g_1 determining the asymmetry of the coupling constants and coupling losses in such structures.

The role of parameter g_2/g_1 can be studied in a broad range of indices and diameters of microresonators. Below, we consider two representative cases with different n and D, but similar and modest quality factors (Q~10^3-10^4) of loaded WGM resonances. These cases can be used for practical realization of such structures in different material systems. The entire range of variation of parameters n and D available in practice is rather broad. Particularly interesting cases are represented by ultrahigh Q-factors ($>10^6$) which can be realized in larger resonators; however, these cases are outside the scope of this chapter.

The first case is represented by the combination of n=3.18 and D=3 μm considered in our previous studies. As stated earlier, it describes semiconductor (such as InP) microrings or disks in near-IR spectral range. The second case represents a high-index glass implementation with n=1.9 and D=7 μm which can be realized using barium titanate glass (BTG) microrings, disks or microspheres also in near-IR spectral range. In the latter case, we used side-coupled WG_1 and WG_2 with refractive index of 1.44 matching the index of silica.

The asymmetric optical transmission properties along certain path are compared for single and double microcavity routers in Figs. 3.7(a) and 3.7(b) for these two implementations, respectively. This study is performed as a function of the spatial asymmetry of the structures represented by the parameter g_2/g_1 plotted along abscissa in these plots. In both cases, T_{13} and T_{31} are calculated for forward and backward directions respectively. In the case of single microresonator, the IR parameter was calculated at the wavelength resonant with WGM in a single circular resonator similar to how it was introduced in the discussion of Fig. 3.4. In the case of double microresonator, the IR parameter was calculated at the wavelength resonant with the bonding mode in photonic molecule similar to how it was introduced in the discussion of Fig. 3.6. Similar analysis can be performed at the wavelength of the antibonding mode, but it is not included in this work.

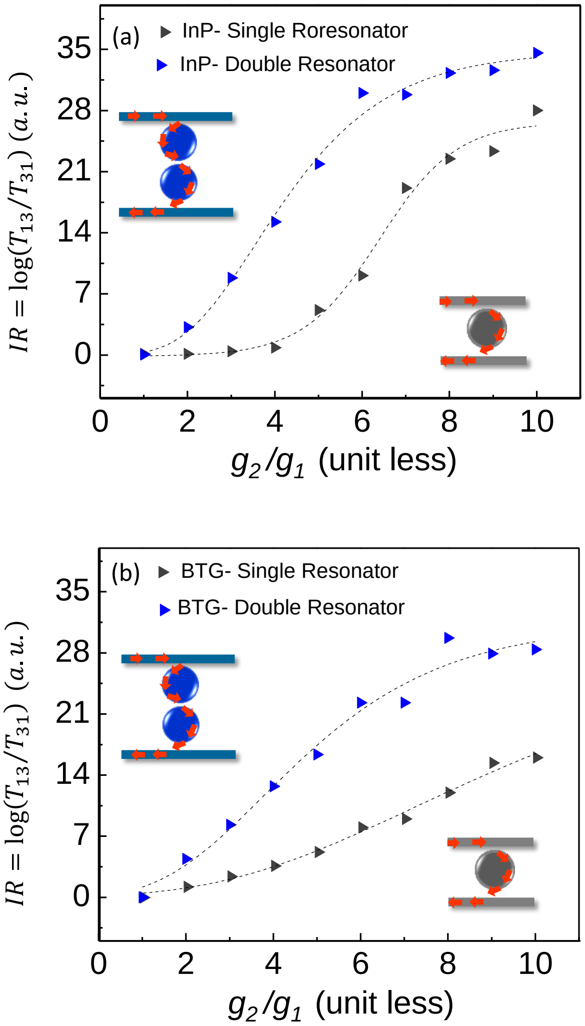

Figure3. 7: Comparison of the $IR = log(T_{13}/T_{31})$ for a single microresonator (gray color) with double microresonator router (blue color) for resonators with (a) n=3.18, D=3 μm (semiconductor case of InP) and (b) n=1.9, D=7 μm (barium titanate glass (BTG) case). T. For single microresonator, the IR parameter is calculated at the WGM wavelength, whereas for double microresonator, the IR parameter is calculated at the wavelength of B mode of photonic molecule. It is seen that IR=0 dB for symmetric structure with g_2/g_1=1. The parameter IR increases with the structural asymmetry represented by the parameter g_2/g_1, reaching values 20-30 dB for g_2/g_1~10. Generally, the optical losses are also increasing in structures with strong asymmetry. In both cases (a) and (b), double microresonator router shows a significant enhancement of the IR factor compared to the single resonator.

The results presented in Fig. 3.7 allow making several conclusions about the asymmetry of the optical transport along selected paths. First, as expected, the optical asymmetry represented by the parameter IR is rooted in the asymmetric coupling constants and coupling losses represented by the parameter g_2/g_1. For even gaps, g_2/g_1=1, IR=0 dB indicating the same transmission in both directions. With increasing gap ratio, the parameter IR increases for both single and double microring structures reaching the values 20-30 dB for g_2/g_1~10. It should be noted that the intensities of the transmitted peaks are significantly reduced compared to that in the input pulses since the structure is inherently lossy. Second, the double microcavity structure possesses significantly larger IR values compared to the single microcavity case. In a single microcavity case, achieving IR>20 dB requires gap ratios g_2/g_1>7 (Fig. 3.7(a)), whereas in the double microcavity it can be achieved with g_2/g_1>5 (Fig. 3.7(a)). Third, these conclusions generally hold for both semiconductor- and glass-based designs displayed in Figs. 3.7(a) and 3.7(b), respectively. Although the diameters and indices of resonators are significantly different in these two cases, the WGM Q-factors are comparable that results in similar dependencies of IR on g_2/g_1. In principle, such structures and devices can be designed for a broad range of parameters of microresonators in various material systems, however this task goes beyond the scope of this chapter.

3.6: Routing properties as a function of the spatial asymmetry ($g_2/g_1>1$)

We turn now to study of the routing properties of such structures as a function of their asymmetry. The basic understanding of the routing properties can be obtained for large circular resonators separated by large symmetric gaps. These conditions mean that the microcylinders are weakly coupled and that the coupling between the stripe WGs and microcylinders is also weak. Based on k-vector conservation, as we mentioned in the introduction, one would expect excitation of clockwise WGMs in the single microresonator and excitation of two oppositely circulating WGMs (clockwise in the upper and anticlockwise in the lower microresonator) in the double microresonator case. It means that in the single microresonator case Port 1 is expected to be coupled to Port 3 whereas in the double microresonator case it would be coupled to Port 4.

For our sufficiently high-index and compact microresonators the effective length of the couplers from stripe waveguides to circular microresonators is too short which means that the application of k-vector conservation is not straightforward. In addition, in the double microresonator case the coupling between two circular resonators is realized in the strong coupling regime that results in formation of supermodes with standing patterns of electromagnetic fields. These factors seriously complicate the coupling scenario and such analysis requires numerical solution of the Maxwell's equations.

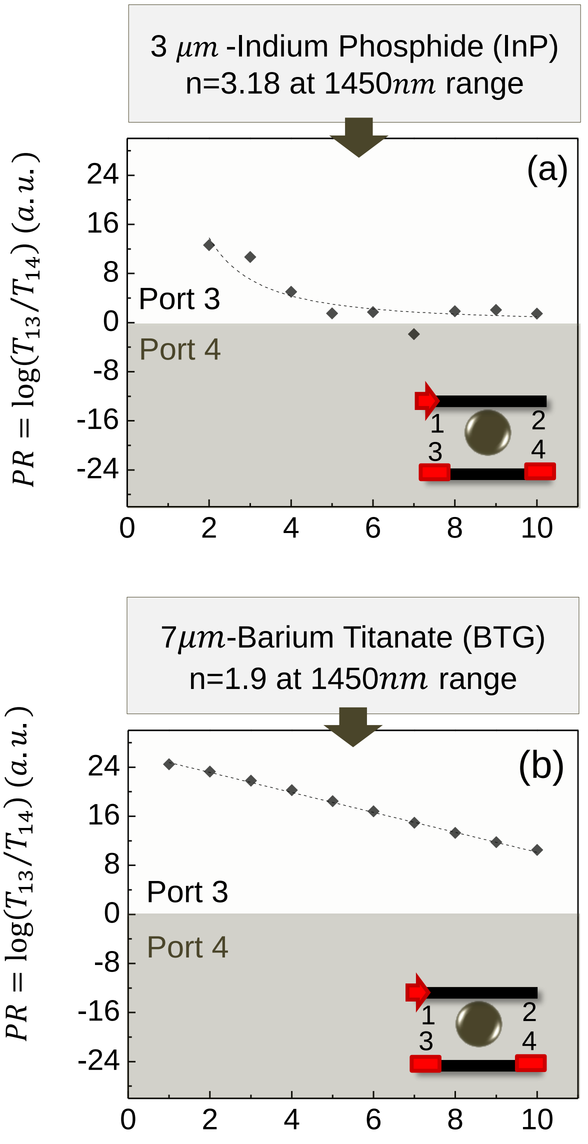

Figure3. 8: Path ratio as a function of gap ratio (g_2/g_1) for single resonator in two cases of InP and BTG as a material for microresonators. In (a,b), the signal detected in Port 3 is stronger than in Port 4 since PR>0 dB. The PR value is found to decrease with g_2/g_1.

We begin with the single microresonator case presented in Figs. 3.8(a) and 3.8(b) for high-index semiconductor and glass microresonator, respectively.

The PR parameter was calculated at the wavelength resonant with WGMs in a single resonator similar to how it was discussed in the description of Fig. 3.4. It is seen that in the case of symmetric gaps (g_2/g_1~1), the PR factor is positive and large (>13 dB in Fig. 3.8(a) and 24 dB in Fig. 3.8(b)). The corresponding points are located in the top half of the graph (pink background). This means that Port 1 is coupled predominantly to Port 3 as expected according to *k*-vector conservation. With the increase of the g_2/g_1ratio, however, the value of PR factor is reduced indicating that for large coupling gaps g_2 the signal is coupled to both Ports 3 and 4. This effect of reduction of PR with $g_2/g_1$is more pronounced in Fig. 3.8(a) compared to that in Fig. 3.8(b). It can be explained by the fact that much smaller resonator with much higher refractive index cannot be viewed as a linear coupler (with *k*-vector conservation) for sufficiently large gaps and that it provides equal signals at Ports 3 and 4 (PR asymptotically approaching 0 dB for g_2/g_1~10).

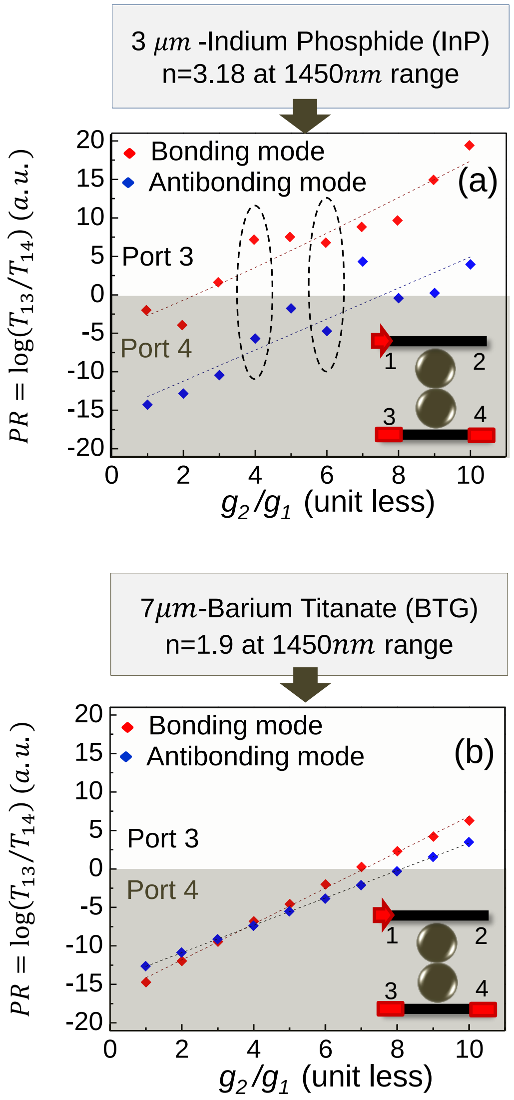

Figure3. 9: Path ratio as a function of gap ratio (g_2/g_1) for double circular resonators. The PR values are calculated for both B and A modes. At g_2/g_1~1, the transport at the wavelengths of both B and A modes is more efficiently coupled to Port 4 resulting in PR<0 dB (blue background). However, with increasing g_2/g_1 the values of PR increase and become positive that indicates more efficient coupling to Port 3. In (a), for InP microresonators, the PR factors for g_2/g_1= 4 and 6 (dashed ellipses) are positive for B mode and negative for A mode indicating that the corresponding wavelengths are coupled predominantly to Ports 3 and 4. This effect, however, is not observed for BTG resonators in (b) with larger D and smaller n.

The case of double microcavity is much more complicated because coupling is provided separately at the wavelengths of bonding and antibonding supermodes, as illustrated in Figs. 3.9(a) and 3.9(b) for high-index semiconductor and glass microresonators, respectively. Beginning with the case of symmetric gaps (g_2/g_1~1), it is seen that for both B and A modes the PR factors are negative. The corresponding points are located in the bottom half of the graph (blue background). This means that Port 1 is coupled predominantly to Port 4 as expected according to k-vector conservation. The behavior of the PR factor with the increase of the g_2/g_1 factor is, however, different from single microresonator since the corresponding dependence is not simply approaching zero, but moving into positive (pink background) top half of the graph which means that for large coupling gaps g_2 the input signal is coupled predominantly to Port 3. As a guide for eye, we showed the corresponding dependences for B and A modes using dashed red and blue straight lines, respectively.

For compact high-index semiconductor double microresonators illustrated in Fig. 3.9(a) the PR factors calculated for B modes are systematically larger than the corresponding PR factors for A modes by ~11-12 dB. Both dependencies have nearly the same slope which means that at some intermediate values of gap ratio, $4 < g_2/g_1 < 6$, the PR factor is negative for A mode (~ -5 dB) and positive (~7 dB) for B mode. These cases are marked by dashed ellipses in Fig. 3.9(b). Such situations are of interest for developing novel wavelength demultiplexors. They mean that connectivity to different ports can be provided at different wavelengths via coupling to different supermodes of photonic molecule. The example in Fig. 3.9(a) represents the simplest case of two-atom photonic molecule. However, similar ideas can be used to connect different ports at various wavelengths in more complicated photonic molecules. It seems that the key to this very interesting behavior is represented by the use of compact high-index microresonators with stronger confinement of corresponding WGMs. As an example, the corresponding dependences for B and A modes as a function of g_2/g_1 are not well separated in Fig. 3.9(b) which shows that design of such wavelength demultiplexors is not possible for larger microresonators with smaller index of refraction.

3.7: Double microresonator structure illustrated by the field maps

In order to provide a direct evidence for wavelength demultiplexing in high-index semiconductor double microresonator structure, we calculated electromagnetic field maps for B and A modes at the gap ratio, g_2/g_1 =6. This case is represented by right ellipse in Fig. 3.9(a). Spatial E-field maps were obtained using a frequency domain monitor in FDTD solver offered by Lumerical that represents the impulse response of the system and collect the steady state EM field data at each mode's eigen-wavelength.

A couple of phenomena can be interpreted using E-field maps. In forward direction (Figs. 3.10 (a,b)), there is an efficient coupling between WG_1 and

MR_1 due to the very small gap, $g_1(100\,nm)$, and light can be strongly coupled into the system. For short wavelength antibonding mode in Fig 3.10(a), the E-field is "repulsive" between two microresonators due to their phase mismatch at the contact point, thus the E-field intensity is reduced at this region. However, light scattered into the medium can be coupled outside the contact region, which can contribute significantly to the antibonding coupling into the MR_2. At the lower side of the photonic molecule, there is a week coupling between MR_2 and WG_2 because of the very large gap g_2 (600 nm). Even scattered light cannot find an easy way to tunnel into WG_2. It leads to resonant electromagnetic buildup in MR_2. This can explain why MR_2 is brighter when compared to MR_1 in Fig. 3.10(a) for antibonding mode field distribution.

For bonding mode, in contrast, the E-field is better overlapped at the contact region due to improved phase matching and more efficient evanescent side-coupling for WGMs. This can be seen through Fig. 3.10(b) as "hot spots" at the region where two microresonators touch. Since the coupling between microresonators is very strong, the intensity distribution indicates that light tends to propagate at both constituent microresonators in similar fashion rather than to stay in MR_1 and circulate. Meanwhile, because of weak coupling between MR_2 and WG_2, similar to the case of antibonding mode, light buildups in the molecule but this time in both coupled microresonators. The light is then weakly coupled to WG_2. The overall view of field maps for both bonding and antibonding modes in forward direction verifies that routing at the wavelength of antibonding mode drives the signal mainly toward port 4 (Fig. 3.10(a)), while bonding mode is strongly observed at port 3 in Fig. 3.10(b). This is inconsistent with the $PR = \log(T_{13}/T_{14})$ calculations showing mode de-multiplexing described in Fig. 3.9(a) for g_2/g_1= 6.

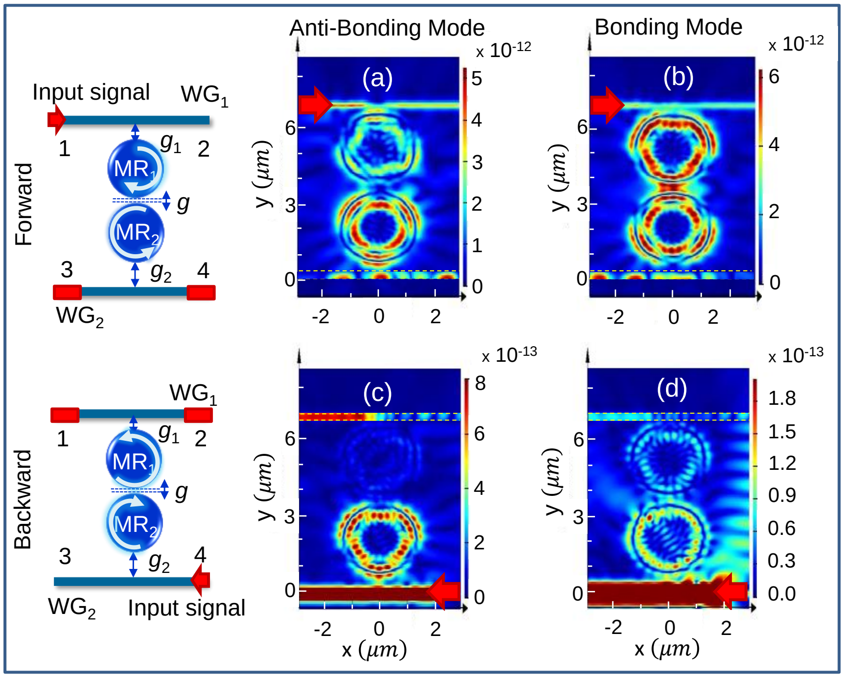

Figure3. 10: Calculated E-field map for each supermodes (bonding and antibonding modes) in the case of 3 μm InP double microresonator where $g_2/g_1 = 6$. (a, c) show E-field map for antibonding mode in forward and backward directions respectively. Weak filed distribution due to phase mismatch can be seen in microresonators contact point, while for bonding mode in (b, d) the phase matching can be seen as "hot spots" where two microresonators were brought together .The overview of the file map at (a, b), shows the detection of an antibonding mode at port 4 in forward direction, and a bonding mode at port 3, which displays the mode demultiplexing in our designed optical system.

A similar explanation can be applied for WGMs transmission in a backward direction; because of the very large gap between MR_2 and WG_2, for both bonding and antibonding modes in Figs. 3.10 (c,d) the light would be weakly coupled to MR_2. The weakly coupled light then distributes among the resonators corresponding to the attractive and repulsive nature of bonding and antibonding modes respectively. On the other hand, due to the strong coupling between MR_1 and WG_1, the light will not circulate on the photonic molecule long enough and will be efficiently coupled to WG_1. This can explain why $MR_{1,}$ for both cases of bonding and antibonding modes in Figs. 3.10 (c,d), lacks intensity while a measurable field intensity can be seen at WG_1-Port 1. This is in well agreement with the calculated transmitted spectra for bonding and antibonding mode in Fig. 3.6 for asymmetric double microresonator structure, where the coupled bonding and antibonding modes in port 2 are too weak (Fig. 3.6(e)) while antibonding mode in port 1 can be detectable (Fig. 3.6(f)).

3.8: Pulse enhanced optical unidirectional system using gain element

It was shown in previous sections that our engineered photonic molecule clearly demonstrates noticeable isolation ratio specially in the case of double resonator, however because of weak coupling between MR_2 and WG_2, and also dissipative scattering or curvature leakage of passive circular resonators, the pulse amplitude at output ports drops to a great extent. It is desirable to design a system with asymmetric transmission properties which would have a reasonably high transmission (in one direction) comparable to the signal in the input port. To address this requirement, instead of passive resonator, we re-design our system with active resonator. We used red color to indicate the location of the active resonators in Figs. 3.11 and 3.12. The goal is to recover the normalized transmitted spectra for forward direction up to 1, and still preserve the high isolation ratio. To provide gain in the microresonator, we need a material with a negative imaginary index over the frequency range of interest. In the modeling, this can be achieved with a Lorentz gain model when the Lorentz permittivity is negative. In this model, Lorentz resonance (gain at center frequency) could be set exactly on the resonance frequency in the transmitted spectra where it needs to be amplified. We put the Lorentz resonance on 1420 nm, which is the center wavelength of coupled mode for single resonator, with 400 nm Lorentz linewidth. The linewidth is set broad enough to cover at least entire one free spectral range. The dashed curve in Figs. 3.11 and 3.12 indicates the spectral behavior of the gain. Moreover, using gain material model makes our system unstable since the gain would eventually lead to lasing in the corresponding physical system. However, describing such lasing would introduce many other effects such as gain saturation that goes far beyond the scope of this Chapter. For this reason, we used linear Lorentz model and simply considered an initial stage of the signal amplification and stopped the calculation at different times to illustrate the increase of the transmission due to the gain without attempting to describe the steady state of the system. For this reason, we defined an auto shut-off parameter in our modeling to stop simulation when we achieved normalized transmission of interested frequency up to 1.

In Fig. 3.11, transmitted spectra for the gap ratio of g_2/g_1= 8 in BTG single microresonator is compared for both case of passive and active resonator. It can be seen from Fig. 3.11(b) that transmitted spectra for coupled mode is recovered up to 1. Calculation for single active resonator shows the isolation ratio around IR= 9 dB, which is dropped compare to the passive case (~3 dB), but still we have reasonable amount for the IR factor.

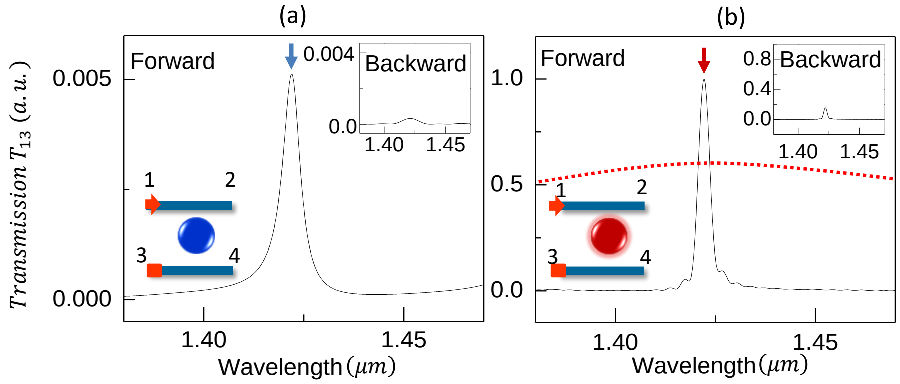

Figure3. 11: Transmitted spectra (T_{13}) comparison between the case of (a) passive (blue), and (b) active resonator (red) for 7μm BTG. For both case the transmission spectrum in backward shown as an inset figure at top right corner. The gap ratio is selected g_2⁄g_1 =8 which give IR factor ~12 dB for the passive case. The Lorentz Resonance and Lorentz Linewidth in the case of active resonator are set on 11420 nm, and 400 nm, respectively which causes the coupled mode recovery up to 1. The red dashed curve shows the spectral behavior of the gain. The isolation ratio for the case of active resonator is calculated around 9 dB.

The results for double resonator with the same material and gap ratio similar to the single case are illustrated in Fig. 3.12. We just targeted the transmitted spectra of bonding mode to recover up to 1, therefore the transmitted spectra for antibonding mode can be less or more than 1 in different cases. Figs. 3.12(a) and 3.12(b) show the transmission spectrum when the two microresonators are either passive or active. In this case both bonding and antibonding modes were amplified with the same ratio. Also, backward transmitted pulse is weakly amplified, in contrast to the single active resonator in Fig. 3.11(b), therefore the isolation ratio factor is kept same as the passive case around IR=29 dB (for bonding mode) while the coupled modes are amplified. This gives us clear advantages of using double active microresonator compare to single one since it manifests itself on better isolation ratio for recovered transmitted mode, as strongly diminished backward transmitted signal.

Another point which is worth to mention is that double-microresonator isolator system can filter out resonant modes for amplification. In Fig. 3.12(c), we put gain on MR_1, and left MR_2 to be passive, while in Fig. 3.12(d), this state is inverted; MR_1 is active and MR_2 is passive. Under this condition, bonding and antibonding modes will not be amplified with the same ratio. Rather, bonding mode would be more amplified when the first resonator is active and antibonding mode when the second one is active. It can be qualitatively explained based on calculated EM maps in Fig. 3.10. When the first resonator is active, for the antibonding mode there is not enough energy build up on MR_1 (Fig. 3.10(a)), therefore putting gain on MR_1 cannot amplify the antibonding mode noticeably, while for bonding mode because of uniformly distribution of energy among both microresonators for this resonant mode, the signal for bonding mode would be amplify which can be seen in Fig. 3.12(b). The similar explanation can be applied when the second resonator is active, and the first resonator is passive. For this case there is more energy build up for antibonding mode in MR_2 compare to MR_1, and for bonding mode although the field is distributed between MR_2 and MR_1, however in a defined time interval the antibonding mode energy has more chance to build up in MR2 since it is the active resonator, and hence antibonding mode grows up faster compare to bonding mode. As a result, for this case in Fig. 3.12(d) we would have much more amplified signal for antibonding mode compare to bonding mode. In the case where both resonators are active in Fig. 3.12(c), the signal ratio of amplified bonding and antibonding modes is similar to signal ratio of modes for passive case where both MR_1 and MR_2 has no gain. In each case the isolation ratio is preserved same as for the passive double-microresonator (~29 dB), while the normalized transmitted signal is enhanced up to 1 for bonding mode.

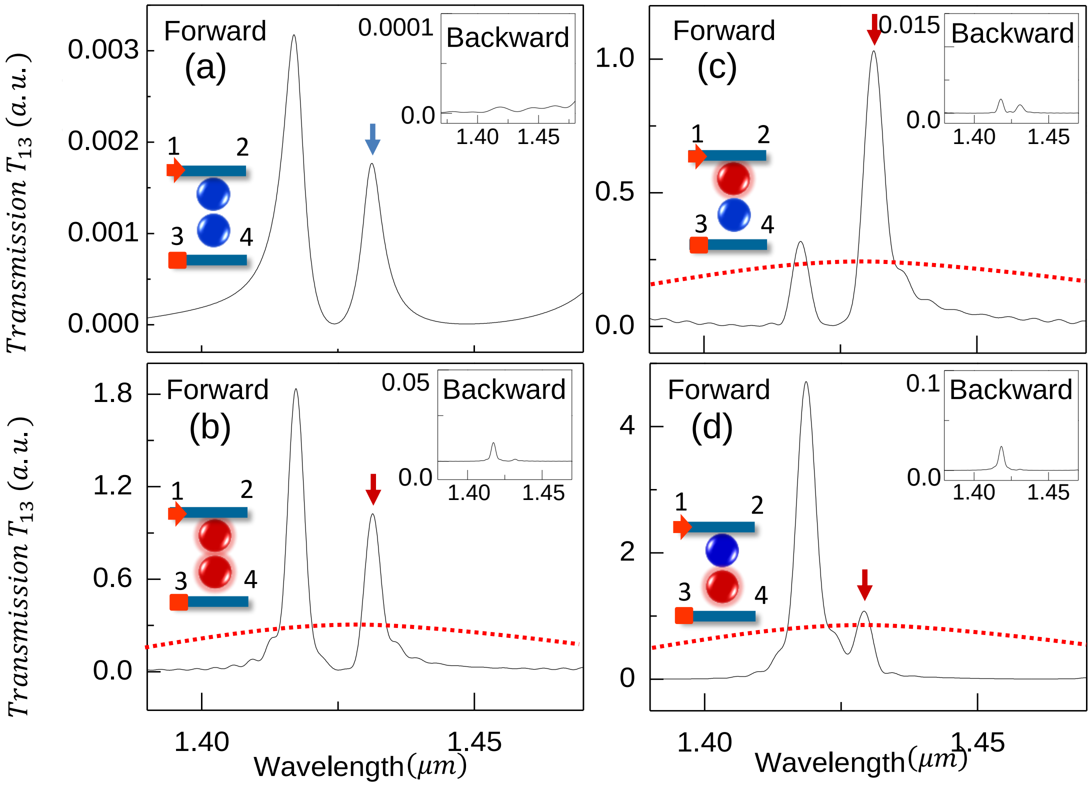

Figure3. 12: Transmitted spectra comparison for double microresonator with introduced linear gain. Blue and red color resemble passive and active resonator respectively. For all cases, just the transmitted spectrum for bonding mode is targeted to be recovered up to1. Comparison between cases when both resonators are passive (a) or active (b) shows both bonding and antibonding mode amplified with same rate, therefore IR factors for each mode remain similar compare to the passive case. In contrast when gain is only introduced in one resonator (c, d) the amplification rate would not be analogous for both modes any more. Introducing gain for MR_1 (c) causes stronger amplified signal for bonding mode while putting gain on MR_2 (d) noticeably amplifies antibonding mode.

3.9: Conclusion

In this Chapter of dissertation, we provided some detailed considerations for the transmission and routing properties of side-coupled circular cavity systems based on two-dimensional finite-difference time domain modeling. The main results and conclusions are listed below:

- In this study, we investigated the directional properties of the optical transport in an on-chip dissipative system of passive circular microresonators side-coupled to stripe-waveguides. These structures can be viewed as 4-port routers where different ports are connected due resonant coupling between the guided modes in stripe-waveguides and whispering gallery modes in circle resonators.
- A spatial asymmetry was introduced in such systems in a form of uneven gaps separating circular resonators from the stripe-waveguides. It was demonstrated that spatially asymmetric and lossy systems have asymmetric optical transmission properties for the waves propagating in forward and backward directions between the ports.
- We demonstrated for non-optimized single microcavity structures that introducing the spatial asymmetry results in isolation ratios (the ratio of transmission in forward and backward directions between the same ports) on the order of 10 dB for wavelengths resonant with WGMs.
- We study the optical connectivity between different ports in more complicated structures where two identical circular resonators are strongly

coupled resulting in formation of bonding and antibonding molecular modes. It is shown that at the wavelengths resonant with hybridized molecular modes the isolation ratios can be increased beyond 20 dB.

- Our calculation for E-filed distribution of resonant bonding and antibonding modes in double resonators structure shows the possibility of controlling the path of different modes, in such a way that different wavelengths can be preferentially coupled to different ports. Therefore, the direction of optical coupling between the ports become frequency dependent. This opens principle possibilities to design a structure with wavelength demultiplexing functionality, and we demonstrated bigger that 10 dB path ratio difference for resonant routing between different ports in such structures.
- From the first sight, the optical losses in such structures can be viewed as being extensive; however, the signal can be recovered using elements with the gain. In principle, the realization of such structures is possible on a semiconductor platform using a combination of lithographic and etching techniques. In such semiconductor structures as coupled microdisks, the gain can be added directly on a chip by doping microrings with the active ions. In this regard, for our modeling study, introducing linear gain to the compact circular resonators exhibited remarkable isolation performance with restored forward transmitted signal in contrast with sufficiently weak backward transmitted one. Also, our modeling shows that the double-microresonator

photonic molecule is capable of selectively amplifying different modes with significant IR factor.

- Another limitation for the proposed structures and devices come from the fact that the individual microresonators constituting the photonic molecules were considered to be completely identical, whereas in fact inevitable fabrication imperfections lead to a random variation of their dimensions and even shapes. On a semiconductor platform, the individual resonances can be tuned using local heating effects produced by the focused laser beams, or local micro-heaters integrated on chip. An alternative approach to creating such structures is based on using dielectric microspheres as building blocks. The spheres with the same resonant positions of WGM peaks can be optically sorted using effects of resonant radiative pressure [201, 202, 204, 207, 293]. Such identical microspheres can be assembled in different configurations to form "photonic molecules" [58, 256, 288] or 3D crystal-like structures with coupled WGMs [181]. Such coupled microresonator structures can be used as novel sensors [216, 259] and as the resonant unidirectional [280, 294], routing, optical demultiplexing, and switching [290] devices discussed in the present study. The optical properties of photonic molecules can be studied using tapered fibers [213, 295] or Stripe waveguides evanescently coupled to such structures.
- The structures considered in this chapter of dissertation do not possess nonreciprocity in a true sense; However, the structures do have a

combination of routing, wavelength demultiplexing, and asymmetric optical transport properties which can be very useful for developing chip-scale telecom and sensor devices. The ports in such structures can be connected in narrow spectral ranges and in only one direction or in both directions. As it mentioned above, fundamentally, this is determined by many factors such as the mode conversion and coupling through asymmetric gaps, strong asymmetric losses, and a few-mode input.

CHAPTER 4: MODELING STUDY OF PHOTONIC JETS FOR HIGHLY EFFICIENT MID-IR FOCAL PLANE ARRAYS WITH LARGE ANGLE-OF-VIEW

4.1: Introduction to Modeling of Photonic Jets

Dielectric microspherical structures along with their resonant properties discussed in Chapter 2 and Chapter 3 also have the ability to produce extraordinarily tightly focused beams termed "photonic nanojet" through non-resonant mechanisms as it mentioned the introduction Chapter. Using this unique property of microspherical structures for extremely sharp focusing of light opens a promising way to increase the efficiency of mid-wave infrared (MWIR) focal plane arrays (FPAs) detectors. Photonic jets produced by microspheres have narrow (down to $\sim\lambda/3$) and elongated (length $\sim 2\lambda$) waists which allows efficient coupling of light incident on microspheres into photodetector mesas with subwavelength diameters ($d<\lambda$). The advantage of photonic jets for concentrating of electromagnetic power by $\sim 10^2$-10^3 times in very small excitation volumes was theoretically predicted for Ge photodiodes [119].

Previous work in Mesophotonics Lab revealed some advantages of microspheres for collecting light from broader areas and focusing it down to small mesa size. Compared to the case of wide-field plane-wave illumination, integration with microspheres with diameter $D>d$ can increase the sensitivity of individual photodetectors by a factor of $\sim(D/d)^2$. Experimentally, the sensitivity increase by up to 100 times was demonstrated for InAs/InAsSb type-II strained-layer superlattice (SLS) detectors at 80K [120, 296]. This has been achieved in collaboration with Air Force Research Laboratory, Sensors/ Materials and Manufacturing Directorates where the FPA structures were fabricated. These structures were passed to UNCC where the microspheres were micromanipulated to mesas by the previous student of the Mesophotonics Lab, Dr. Kenneth Allen as illustrated in Figure 4.1. In this setup, in order to provide efficient coupling of the photonic jet into the photosensitive region, microsphere was aligned with the device mesas by controlling the virtual imaging through the spheres used as contact microlenses [120].

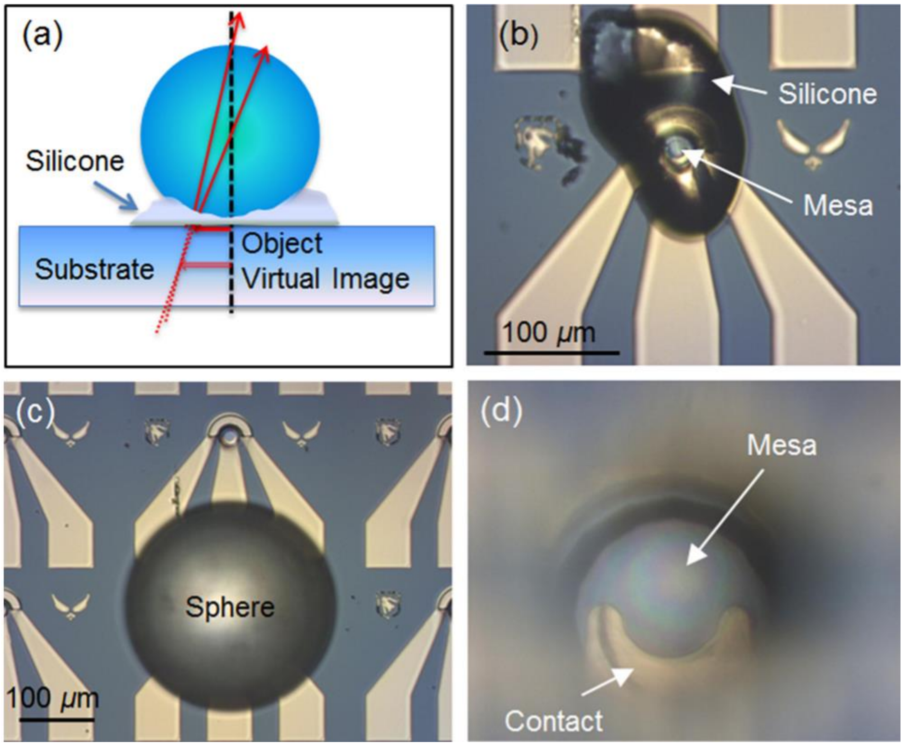

Figure 4. 1: Microsphere integration with the photodetector mesa using silicon adhesive layer. (a) Virtual imaging formation (b) using silicone to integrate the microsphere to the photosensitive mesa, (c) microsphere correctly aligned at the top of the mesa, (d) virtual image of the photodetector mesa through the sphere [120].

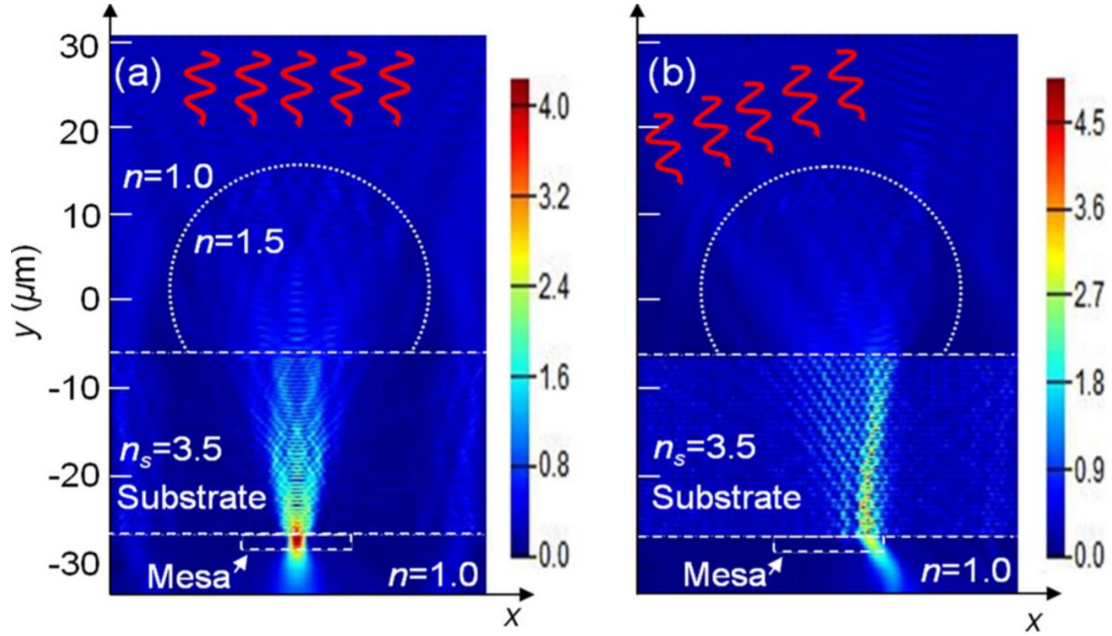

Figure 4. 2: 2D EM field maps calculated at λ=3 μm for back-illuminated FPA with the 20 μm substrate, D= 30 μm cylinder truncated by 10.5 μm, and d=12 μm mesa size (a) Sharp focusing on the back surface of the substrate at normal incidence case (b) Incidence at AOV= 20°showing that the focused beam is still located within detector mesa [120].

In next steps, to quantitatively understand the angular acceptance properties of these structures, I performed numerical modeling of such microspherical lenses as light collection system integrated with FPA structure. In my modeling studies, I used FDTD code developed by Lumerical. The first trial tests went successfully, and I estimated the angular acceptance of the structures fabricated at that time experimentally based on individual micromanipulation with several microspheres. The result of the modeling is shown in Fig. 4.2 (a,b) for back-illuminated FPA, where the substrate with index n_s= 3.5 is polished to 20 μm thickness. To simplify calculations, the numerical simulation was performed in the 2-D cylindrical geometry which has all essential features of 3-D case. The field map presented in Fig. 4.2 for D=30 μm, and n-1.5 cylinder truncated by 10.5 μm shows that such structure has an AOVs ~ 20° for relatively small size of the detector mesa (d=12 μm) at λ=3 μm wavelength.

Although the first results of this study were promising however, the questions about the optimal design of such structures still required further investigation. In particular, it was not clear what is the optical size and index of the microspheres for this application, how to fix of microspheres in an optimal position in terms of using additional layers in the structure such as photoresists or epoxies. Most importantly, what should be the design guidelines, or in more general terms, what are the main basic principles of optimization of such structures. Often, optimization of one parameter in device design for achieving maximal performance can have some tradeoffs, so that the other parameters can become suboptimal for other achieving other performance characteristics of the device. As an example, increasing the size of the spheres increases the collection of photons and corresponding enhancement factor, but it also increases the size of the FPA pitch. At some point, the pitch can become too large for developing practical applications. Similarly, to provide large enhancement factors, it is important to reduce the size of the photodetector mesa, however too small mesas can block the transmission of light to the detector even despite the focusing provided by the microspheres. Understanding these tradeoffs was one of the tasks of the

Chapter. However, in order to tackle these problems, first of all, we had to develop the guidelines for modeling. Using these principles, we can then consider performance of these structures with various parameters of spheres and structural layers, which, in its turn, would help us to optimize these structures.

In addition to the main subject of this Chapter on FDTD modeling for enhancement of FPA using photonic nanojet, I also performed a modeling study of focusing properties of microspheres in a different type of structures represented by linear chains of touching dielectric microspheres. This is clearly a different geometry compared to FPAs where the spheres are assembled as a single monolayer. However, the linear chains of microspheres are interesting because of their periodical focusing properties which can be used for laser scalpel and other applications [Astratov et al, SPIE Newsroom and other publications]. Computationally, these studies were performed by FEM method as opposed to FDTD method used for FPA modeling. However, we decided to combine these results in Chapter 4 because they are devoted to essentially similar light focusing properties of microspheres. The content of this Chapter is the following. In Section 4.2 we consider modeling of periodically focused beams in microsphere chain waveguides (MCW). In Section 4.3 we present modeling results, including the design guidelines (Section 4.4.1), properties of commercial microlens arrays (Section 4.4.2), and properties of the back-illuminated (Sections 4.4.3 and 4.4.4) and front-illuminated (Section 4.4.5) FPAs integrated with microspheres. We optimized our designs for achieving collection of light with maximal AOV using microspheres with various index of refraction and diameters in the 30-60 µm range. We show that microspheres provide an order of magnitude higher AOVs compared to commercial microlens arrays.

4.2 Periodically Focused Beams in Microsphere Chain Waveguides

Previously there were performed extensive experimental studies in Mesophotonics Lab directing on the focusing and transport properties of spheres chain with size variation from geometrical scale to mesoscale as well as different refractive index [179, 209, 210, 215, 217, 297-301]. It was shown microsphere-chain waveguides (MCWs) formed by mesoscale spheres ($4 \leq D/\lambda \leq 10$, where D is the sphere diameter and λ is the wavelength of light), coupled to a multimodal source, gradually filter periodically focused multimodal beam and dramatically reduce the beam waists with the diffraction-limited size with extremely small propagation losses. In fact, in a series of periodically coupled microlenses, each microsphere produces a subwavelength focused spot or photonic nanojet which result in nanojet-induced modes. The result is applicable for developing waveguiding structures with focusing capabilities, which can be used as local microprobes, ultraprecise laser scalpels [297, 302], and polarization filters for non-trivial states (e.g., radially polarized cylindrical vector beams, longitudinal polarization, etc.) [211].

In order to get more insight on optical transport and focusing results in MCWs, I modeled beam tapering properties for 2-D mesoscale chain of cylinders using COMSOL Multiphysics. The simulation was performed in frequency domain by FEM method as illustrated in Fig. 4.3 for touching dielectric cylinders with diameters of 5 μm, and index of 1.6. A triangular adaptive FEM mesh with minimal $\lambda/180$ and maximal $\lambda/18$ sizes was selected to cover the simulation region where λ= 0.53 μm. In order to mimic a multimodal incoherent source in the experimental studies (fluorescent dye-doped spheres), I used a S-cylinder containing 1400 dipole emitters randomly placed along several radial lines with different oscillation directions along y-axis, z-axis, 45° and $-45^{\circ}$with z-axis. As an example, Fig. 4.3(b) represents distribution of dipoles (red regions) oscillating along y-axis inside S-cylinder. Also, in order to reduce any WGM coupling effect between the source S and the first microcylinder, the dipoles were positioned inside the S-cylinder with 0.5 μm gap from the cylinder border. Two monitors, after the first and last cylinders are defined to record transverse irradiance profile as the light propagate through the chain. It should be noted in spite of randomly distribution of dipoles with different polarizations, a pronounce interference effect in the irradiance profiles was inevitable. This effect can be seen in the irradiance profiles in Figs. 4.3(c) and 4.3(d) for two dipole distributions (solid and dotted curves). It can be explained based on a fixed phase difference between dipoles due to the optical path difference separating them and make them like coherent sources. However, the envelopes averaged over many different source configurations with different polarization (red dashed line in Figs. 4.3(c) and 4.3(d)) can be representative of the beam profiles expected from dye-doped spheres as multimodal incoherent source. Considering this fact, transition from wide envelope irradiance peak in Fig. 4.3(c) with FWHM ~1.4 μm after the first cylinder, to a narrower envelope irradiance peak in Fig. 4.3(d) with FWHM ~0.7 μm after six cylinders can be clearly observed. In fact, propagation of light through cylinder chain waveguide can be viewed as a mode filtering process, resulting in formation of very narrow and tightly focused beam waist. Accordingly, this modeling confirms that in mesoscale MCWs, the photonic nanojets can be periodically reproduced along the chain, giving rise beam tapering effect. Such a focused beam as it mentioned above could be useful for laser surgery, high-density optical-data storage, and photo-induced patterning of thin films.

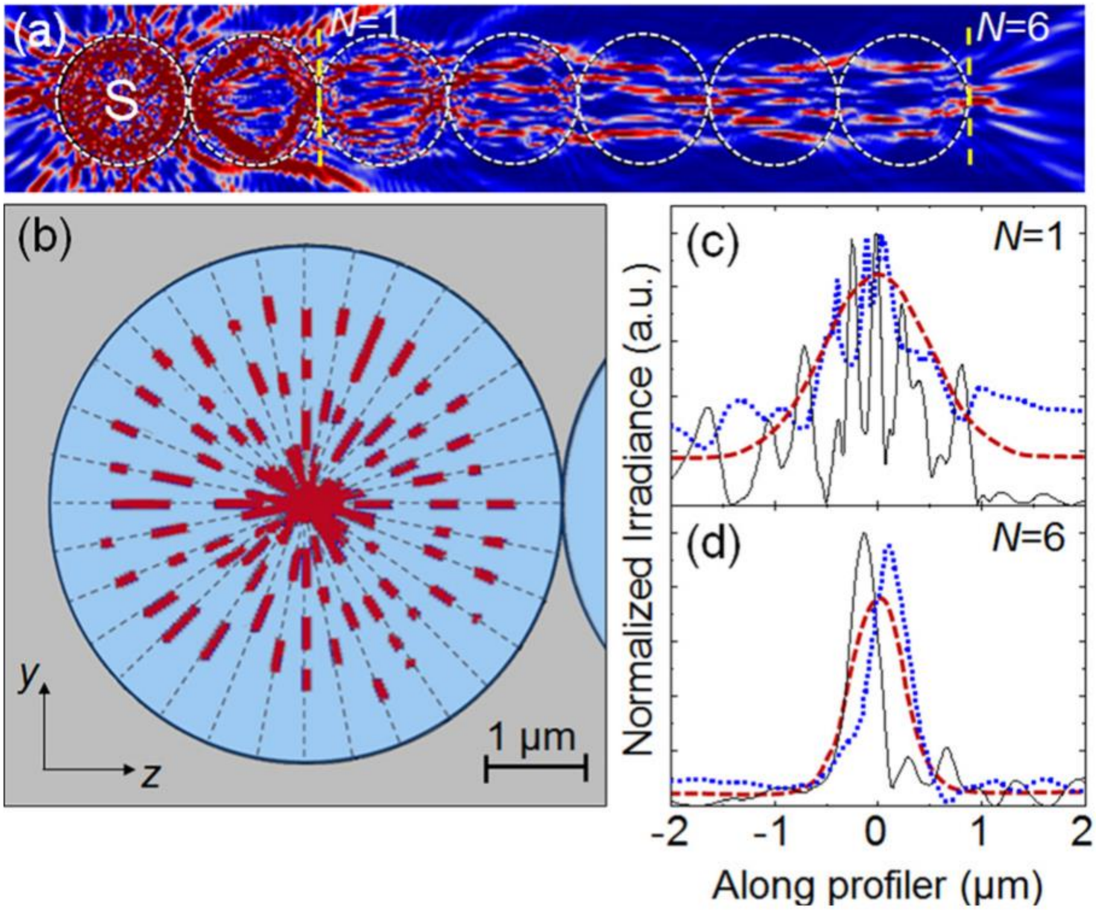

Figure 4. 3: (a) 2D irradiance map for MCW using FEM modeling. (b) distribution of dipoles (red dots) inside S-cylinder polarized along y-axis. (c) and (d) irradiance profiles calculated for two different dipole distributions (solid and dotted curves) after the first (N =1) and the sixth (N = 6) cylinder, respectively [210].

The modeling study for nanojet-induced modes and transport properties of MCWs was an example of simulation work that I performed in frequency domain using FEM method, however the main subject for this Chapter of dissertation focused on FDTD modeling study on photonic nanojet for mid-IR FPAs that continues in the following sections.

4.3: Design and Optimization of Focal Plane Arrays Integrated with Dielectric Microspheres

MWIR FPAs operating in a range of wavelengths (λ) from 3 to 5 μm are the main tools for thermal imaging [116]. The imaging systems based on MWIR FPAs benefit from the atmospheric transparency window and from reduced scattering compared to shorter wavelength systems. It should be noted that MWIR FPAs are the natural candidates for imaging in smog and turbid media. For example, firefighters use MWIR FPAs to see through smoke, find people and locate hotspots. Another important area of applications is connected with imaging and sensing the objects through the fog, mist, rain, snow, and sand in the marine and *terrestrial environments.* The cryogenically cooled thermal cameras provide the best quality MWIR imaging with sufficiently high signal-to-noise ratio [303]; however they are bulky, slow and expensive. In contrast, the uncooled thermal imagers are compact and inexpensive; however, they suffer from the thermal noise and other factors limiting the sensitivity, resolution, contrast, and AOV of MWIR cameras.

A natural way of increasing the resolution, decreasing the thermal noise, and, potentially, increasing the operation temperature of MWIR imagers is connected with the reduction of the diameter (d) of individual photodetector pixels [304]. This approach is currently limited at d~2λ~10 μm which is determined by the diffraction of light and small fractional area occupied by compact photodetector mesas on the FPA chip. At first sight, the photon collection efficiency can be regained by using the commercial microlens arrays which allow collection of light from the entire area of the array followed by focusing light into compact photodetector mesas in such a way that each microlens is optically coupled to an individual pixel. However, commercial microlens arrays contain lenses with long focal distances (f~200 μm) [118], so that a small change of angle of incidence causes the shift of the focused spot away from the compact photodetector mesa. This limits AOV=2arctan($d/2f$) at about 1-2 degrees, that is acceptable in astronomical imaging, but does not allow to develop other applications such as applications in surveillance cameras, motion trackers and many other imaging sensors.

It should be noted that in recent years the performance of FPAs was enhanced due to photon trap structures such as photonic crystals [305], textured surfaces with pyramidal relief features [306], and curved FPAs [307]. The spectral response of pixels was enhanced due to plasmonic gratings [308-312], nanoparticles [313], nano-antennas [314], subwavelength hole arrays [315], and microstructure surfaces [316, 317]. Although the absorptivity and spectral response of individual pixels can be enhanced by using these structures, the enhanced performance usually takes place in a relatively narrow range of wavelengths and AOV of such structures is also relatively narrow.

A combination of enhanced sensitivity with large AOVs makes integration with microspheres very attractive for developing next generation FPAs [318, 319], however it requires several conditions. First, a technology of massive-scale, defect-free assembly of microspheres needs to be developed. Second, the array of microspheres needs to be transferred at the FPA surface (if it was assembled on a separate substrate). The alignment of microspheres with individual pixels needs to be achieved with a micron-scale accuracy. Third, the methods of affixing the microspheres at the FPA surface need to be developed. Finally, the parameters of the FPA structures need to be optimized through numerical design to take under account the microsphere assembly and corresponding electromagnetic field focusing.

In this Chapter, we comprehensively address the last issue. In Section 4.3 we present modeling results, including the design guidelines (Section 4.3.1), properties of commercial microlens arrays (Section 4.3.2), and design of the back-illuminated (Sections 4.3.3 and 4.3.4) and front-illuminated (Section 4.3.5) FPAs. We optimized our designs for microspheres with different diameters in the 30-60 μm range, as well as with various indices of refraction. We show that microspheres allow the same light collection efficiency as commercial microlens arrays, but with an order of magnitude higher AOVs.

4.4: Modeling results

4.4.1: Design guidelines

In the limit of large microspheres (D>>10λ) the focusing effects can be described in the paraxial approximation by the geometrical optics. In FPA structures, however, the spherical aberrations cannot be ignored. In addition, the optical properties need to be determined: i) assuming different microsphere sizes and indices of refraction, and specific thicknesses and indices of all the layers comprising the structure for both back- and front-illuminated structures and ii) assuming cases where the microspheres are partly immersed in a photoresist or truncated. For these reasons, we used the numerical modeling techniques.

FPA optimization is based on the following design guidelines: (i) The narrowest waist of the focused beam should be achieved at the photodetector's mesa plane. The idea is that at normal incidence the focused beam should be coupled through the mesa with the minimal optical losses. (ii) The waist of the focused beam should be smaller than the mesa diameter. In the practical device structure, the photodetector mesa can be defined by the semi-circular metallic electrodes terminating the aperture of the incident focused beam [120]. (iii) The affixed microspheres with the diameters in the 30-60 μm range close to typical pitches of MWIR FPAs and with the refractive indices in the 1.4-1.8 range have rather short focal distances that make it implausible to fabricate extremely thin substrates required for the back-illuminated structures. The solution comes from the fact that the refractive capability of microspheres can be reduced by partly-immersing them in a photoresist or by truncating them. Thus, by controlling the amount of immersion or truncation the structure satisfying guidelines (i-ii) can be designed. (iv) The way of increasing AOV is connected with reducing the focal distance of the microlens. The limitation of AOV comes from the fact that increase of the angle of incidence causes the shift of the photonic jet away from the corresponding photodetector mesa. The amount of shift is proportional to the effective focal length of the microspheres.

In our designs, we used the full wave FDTD modeling for microspheres with diameters in a 30-60 μm range. Such microspheres can be packed in close-packed arrays with the pitch and pattern matching that for photodetector arrays, so that the individual photodetectors are located just below each microsphere. We consider the period of arrays in the 30-60 μm range since it is close to typical distance between the pixels in mid-IR FPAs. To simplify calculations, we used a two-dimensional (2-D) cylindrical geometry which has all essential features of 3-D case. The numerical simulation was performed by finite difference time-domain (FDTD) method with the commercial software by Lumerical Solutions Inc. We selected photodetector mesa (pixel) diameter d=10 μm which corresponds to minimal sizes used in practice in mid-IR FPAs. For standard microlens array (Section 4.3.2), we considered dome-shaped microlenses fabricated at the top of the plastic layer with the refractive index n=1.44 and the thickness 165 μm. This plastic coverslip layer is supposed to be mounted at the front surface of FPA. We show that this combination of parameters results in focusing of the incident plane waves at the plane of photodetector array; however, the large focal distances result in AOV~1°. For back-illuminated structures enhanced with microspheres we considered two cases differing by parameters of microspheres and layer thicknesses. In Section 3.3, we consider microspheres with index, n=1.46, and with diameter, D=60 μm, semi-immersed in a layer of photoresist and demonstrate AOV of 5°. In Section 3.4, we consider slightly truncated microspheres with higher index n=1.56 (polystyrene) and diameter D=60 μm and show that it leads to AOV of 8°. For front-illuminated structures (Section 4.3.5) the thickness of the semiconductor slab is not a relevant parameter. In the latter case, we consider high-index (n=1.8) microspheres with D=30 μm and show that it results in AOV of 20°. The illumination was provided by plane waves at λ=4.0 μm; however, the investigated optical properties are not strongly wavelength dependent, and the results are generally applicable in the mid-IR range 3-5 μm. Thus, we demonstrate the increase of AOV by more than order of magnitude compared to commercial microlens arrays as a result of integration of FPAs with microspheres.

4.4.2: Standard microlens array

To show that conventional microlens arrays fabricated on a planar substrate (shown in Fig. 4.4) inherently limit AOVs of FPAs, we consider a plastic moldable material with reasonable optical transmission properties in MWIR range. In our design we did not specify the material and simply assumed that it has the index of refraction 1.44 at λ=4.0 μm. In practice, it can be polydimethylsiloxane (PDMS) or polymethyl methacrylate (PMMA) or other similar material. Silica can be also used, but it is absorptive in MWIR range. All these materials have the index of refraction which is sufficiently close to 1.44 which means that the conclusions of our consideration are generally applicable to all these materials. Alternatively, the MWIR FPAs can be fabricated from high index materials such as Si or Ge. It should be noted, however, that Si is fragile and hard to machine. In addition, the radius of curvature of Si lenses is usually large which results in sufficiently long focal distances [118] comparable to that obtained with plastic lenses which have larger curvature. Germanium has similar properties to Si but is also much rarer. Since AOV is largely defined by the effective focal distances, all microlens arrays designs including low-index plastics and high-index semiconductor materials have very limited AOVs. Below we illustrate this problem for a low-index (n=1.44) material.

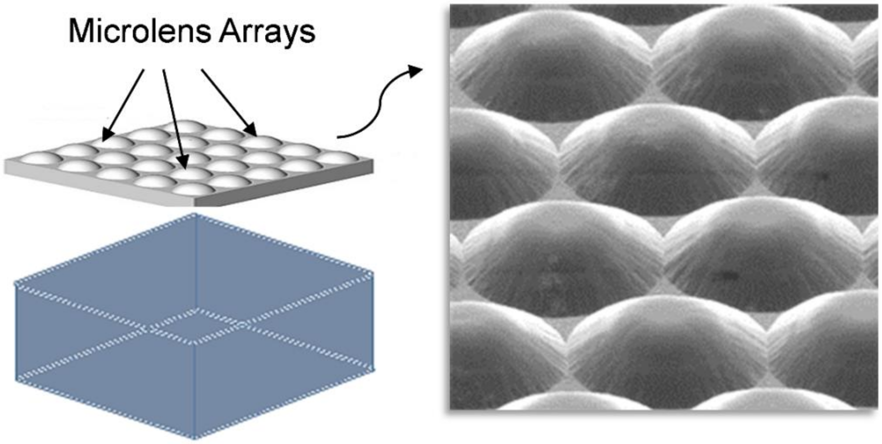

Figure 4. 4: Schematic presentation [320] and SEM image [321] of the microlens array integrated with the back-illuminated optical detector FPA.

As illustrated in Figs. 4.5 (a,b), we assumed that the microlenses have the radius curvature of R_c=72 μm and the lens has a dome shape with the base diameter of 57 μm. It was assumed that such dome-shaped lenses are fabricated at the surface of a slab with the thickness of 165 μm. The electric vector of input (from left to right) electromagnetic plane waves was linearly polarized in the *xy* plane.

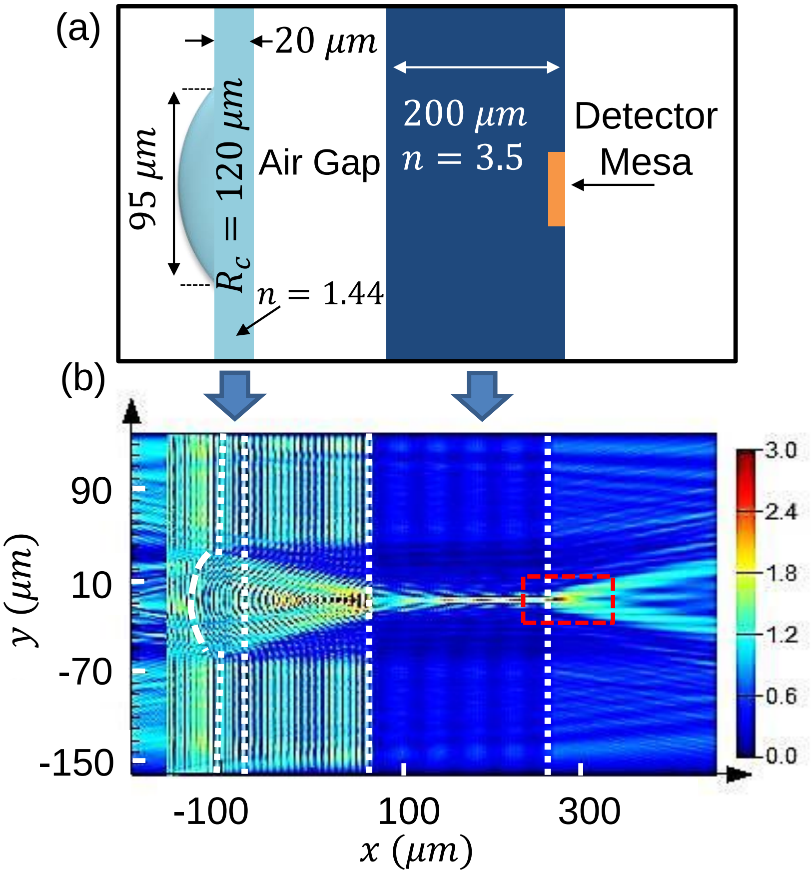

Figure 4. 5: (a) Schematic of the microlens array integrated with the back-illuminated optical detector FPA with 200 μm thickness of the substrate. (b) Electric field map calculated by FDTD simulation at λ=4.0 μm. The position of microlens, substrate and detector are shown with dashed black lines [320].

The incident beam had a Gaussian temporal modulation with 50 fs pulse duration and λ=4.0 μm central wavelength. The location of microlens, substrate and detector are shown by dashed lines in the calculated EM maps in Fig. 4.5 (b). The calculated EM map is for amplitude of electric field which contains all E-field components. The position of the optical components indicated by dashed lines in Fig. 4.5 (b) corresponds to that in Fig. 4.5(a). We considered a back-illuminated structure with the 200 μm thick semiconductor substrate. The refractive index of the semiconductor substrate was 3.5. The mesh size in calculations was $\lambda/(22n)$, where n is the index in the corresponding optical components. The plastic slab with microlenses is supposed to be attached to the front surface of a semiconductor slab.

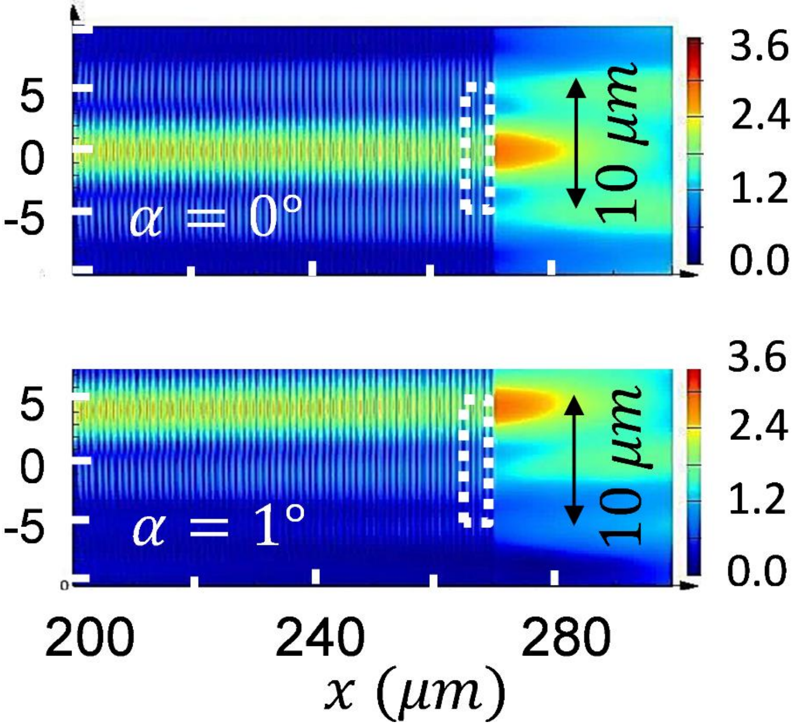

Figure 4. 6: Electric field map correspond to the configuration shown in Fig. 4.5 calculated at λ=4.0 μm for α=0° (top image), and α=1° (bottom image). In the latter case, it can be seen that the focused light beam hits the edge of the detector [320].

As shown in the lower image of Fig. 4.6, for the angle of incidence α=1° the focused beam shifts away from the mesa's center and reaches its edge. For angles of incidence beyond α=1°, the beam is blocked by the edge of the mesa, which means that AOV is close to 1° in this case. It is seen that such array provides efficient collection of light only in extremely narrow cone around the normal direction which can be a limiting factor for some applications.

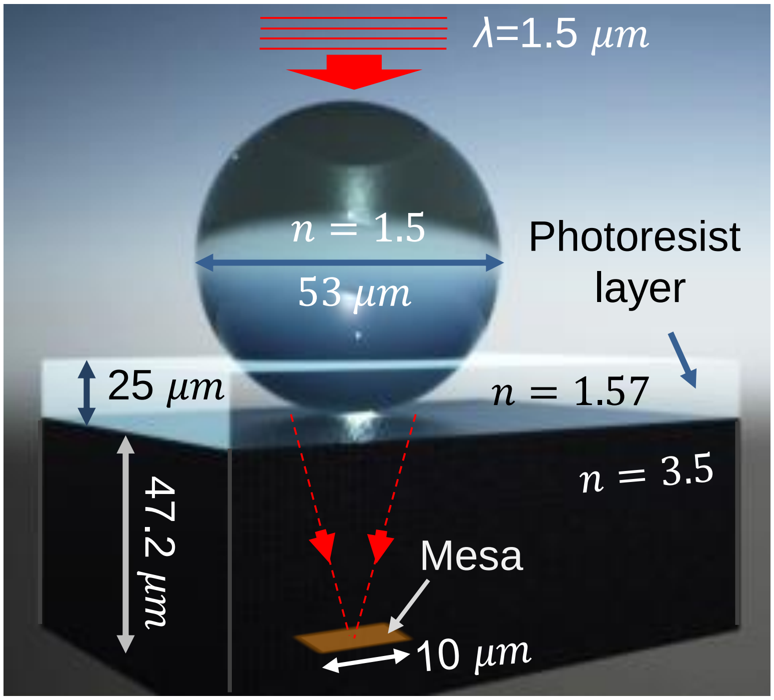

Figure 4. 7: Schematic of 53 μm soda-lime glass microsphere immersed in a 25 μm photoresist adhesive layer at the back-illuminated FPA structure. The thickness of the detector substrate is 47.2 μm [320].

4.4.3: Back-illuminated structure with microspheres partly immersed in a photoresist

The typical structure of FPA integrated with microspheres is illustrated in Fig. 4.7. The diameter of the microspheres is determined by the pitch of FPAs. In order to provide a surface coverage by microspheres with large areal fill factor required for efficient collection of light, the microsphere diameter should be close to the FPA pitch. In the example presented in Fig. 4.7, we considered microspheres with a 60 μm diameter and n=1.46 refractive index (for soda-lime glass as an assigned material). As an example, such microspheres can be used in FPAs with 60 μm pitch. Similar to the previous Section, the structure is back-illuminated, however, the completed microsphere has much shorter focal distance which requires much thinner substrate for focusing light at the photodetector mesa. We assumed that the microsphere was partly immersed in a 25 μm photoresist layer with a refractive index of 1.57. The photoresist layer played a double function in our design. First, it can be solidified to permanently fix the microspheres. Second, it increases the effective focal distance of such lenses which means that the thicker substrates (compared to the case without the photoresist) can be used to provide sharp focusing at the plane of photodetector mesas. Our calculations showed that such structures require a substrate thickness around 47.2 μm. It can be realized in practice by polishing the semiconductor substrate. The alignment of microspheres with photodetectors can be achieved by using fiducial markers or by maximizing the optical signals from the detectors in the course of alignment. As it is shown in Fig. 4.8(b), such structure with reduced effective focal distance has AOV on the order of α=5°, which shows 5-times improvement compared to the standard microlens arrays.

It should be noted that much smaller, subwavelength microspheres assembled as a monolayer can trap the incident light due to periodic diffraction effects leading to formation of 2-D photonic band structure [322, 323]. These effects should not be present in microspherical arrays with the characteristic spheres' dimensions D>10λ considered in this Chapter.

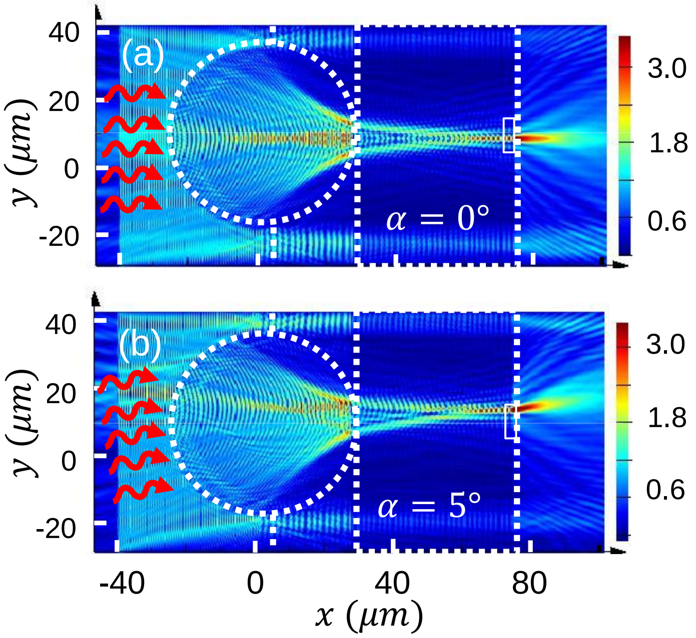

Figure 4. 8: (a,b) Electric field maps correspond to the configuration shown in Fig. 4.7 calculated at λ=4.0 μm for angles of incidence α=0° and α=5°, respectively [320].

4.4.4: Back-illuminated structure with slightly truncated microspheres

The effective focal distance of dielectric microspheres can be further reduced by increasing their index of refraction. Another powerful resource for controlling the effective focal distance is offered by truncation of microspheres as opposed to its partial immersion in a photoresist. The FPA structure based on polystyrene or plastic microspheres with index n=1.56 in mid-IR spectral range is illustrated in Fig. 4.9. This microsphere has the same diameter 60 μm as that illustrated in Fig. 4.7.

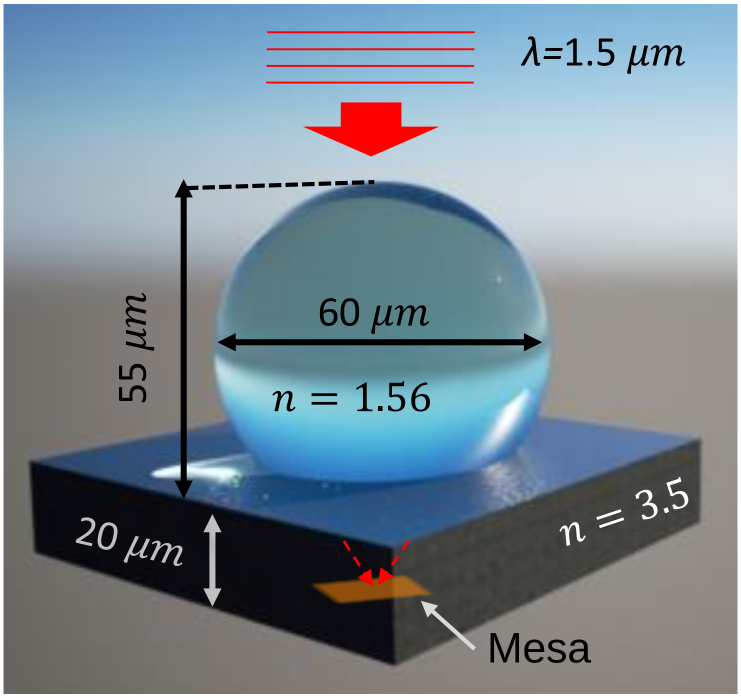

Figure 4. 9: Schematic of 60 µm polystyrene microsphere truncated at a 5 µm depth in contact with a 20 µm substrate in the back-illuminated FPA [320].

It is known that the polystyrene of plastic microspheres can be slightly melted in a region where they contact the heated substrate [324-326]. This leads to a slightly truncated shape of microsphere illustrated in Fig. 4.9. It should be noted that such thermal treatment can be quite convenient in practice since it provides permanent attachment of the microsphere to the semiconductor substrate without using any kind of epoxy or photoresist. In Fig. 4.9 we assumed a truncation of microspheres by 5 μm due to removing of the corresponding polystyrene or plastic material. In practice the amount of truncation can be precisely controlled by the temperature of the substrate and duration of the thermal treatment. Controllable melting of the microspheres can lead to more complicated deformations of their shapes due to a material reflow. The truncation model illustrated in Fig. 4.9 can be considered only as a rough approximation to the real characteristic changes in the shape of the microsphere. As a result of this procedure, the microspheres can be permanently fixed in the optimal positions just above the photodetector mesas.

The combined effect of larger index of refraction and truncation leads to thinner substrates required for focusing incident plane waves at the back surface of the substrate. The results presented in Fig. 4.10 show that such focusing can be achieved with ~20 μm thickness of the polished substrate. In this case, comparison of the EM map in Fig. 4.10 (a) calculated at normal incidence α=0° with the corresponding map in Fig. 4.10(b) calculated at α=8° shows that in the latter case the focused beam reaches the edge of the mesa indicating AOV=8°. Such AOV exceeds that provided by a standard microlens array by almost an order of magnitude.

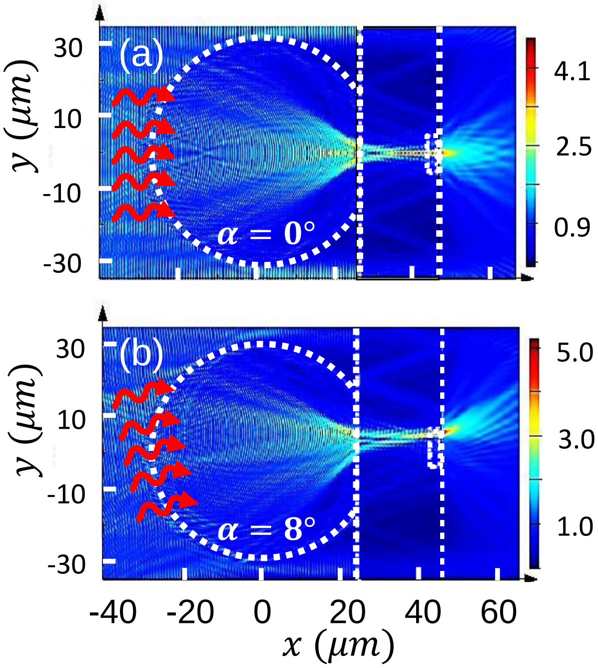

Figure 4. 10: (a,b) Electric field maps correspond to the configuration shown in Fig. 4.9 calculated at λ=4.0 μm for α=0° and α=8°, respectively [320].

4.4.5: Front –Illuminated structure

The maximal increase of AOV can be achieved in the front-illuminated structure where the microspheres are positioned directly above the mesas of the photodetector array, as schematically illustrated in Fig. 4.11. Experimentally, this situation can be realized using barium-titanate glass (BTG) microspheres. According to a manufacturer, Mo-Sci Corporation, these microspheres have index ~1.9 in the red part of visible spectrum. The refractive index is not precisely defined for these microspheres. However, taking into account typical dispersion of the refractive index in high-index glasses, one can assume that their index should be close to ~1.8 in mid-IR spectral range. In addition, in our numerical design we assumed that these microspheres have smaller diameter D=30 μm. Such microspheres focus plane waves close to their backside (not illuminated) surface and they can be used for enhancing front-illuminated FPAs. We assumed that fixing these microspheres can be achieved using a layer of photoresist with 10 μm thickness deposited by spin coating. After transferring the microspherical array and alignment of individual microspheres with the photodetector mesas, the photoresist layer can be solidified by the UV illumination. This combination of properties, refractive index, size of microspheres and their slight immersion in the photoresist, leads to formation of photonic jets at the plane of photodetector array.

The case of front-illuminated FPAs is special because it maximizes the advantages of integration with microspheres. This is determined by the shortest focal distance which can be realized in FPAs integrated with microspheres which translates into maximal AOVs. The calculated EM map in Fig. 4.12(b) shows that for incident angle α=20° the focused beam still hits the edge of the detector mesa, which means that AOV~20° in this case. Further increase of the refractive index of microspheres would result in focusing of light inside the microspheres which leads to the optical coupling losses in FPAs.

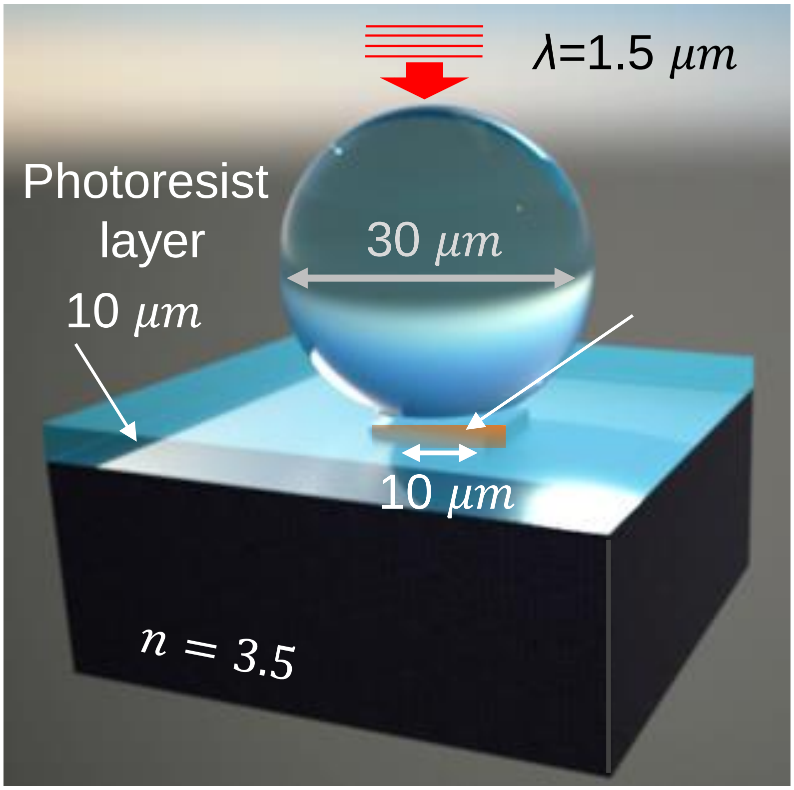

Figure 4. 11: Schematic of a front-illuminated FPA with a 30 μm barium titanate microsphere placed in contact with the 10 μm detector mesa [320].

On the other hand, the case of front-illuminated structures is also special because the same microspheres can be used for super-resolution imaging of the photodetector mesas located just below them [120, 296]. Such imaging termed microspherical nanoscopy attracted a significant interest in recent years due to the fact that it allows overcoming the standard far-field resolution limit, as it is described by the Abbe's formula [154, 157-159, 211, 327-330]. The resolution advantage of this method comes from the fact that the virtual image of the surface produced by microspheres is magnified by a factor between 2 and 5 and it is formed with participation of the object's evanescent fields which carry high spatial frequencies offering more information about the object. From the point of view of technology of integration of microspheres with FPAs, the imaging through microspheres opens a method of alignment of microspheres with the individual photodetector mesas based on direct visualization. If the microsphere is centered with the mesa, the latter appears with a non-distorted circular shape [120]. The fact that the optical imaging can be performed with an order of magnitude better resolution (at least ~$\lambda_i/2$ or better, where λ_i is the illumination wavelength used in the microscope system) than the typical MWIR wavelengths provides a sufficient accuracy for the alignment process.

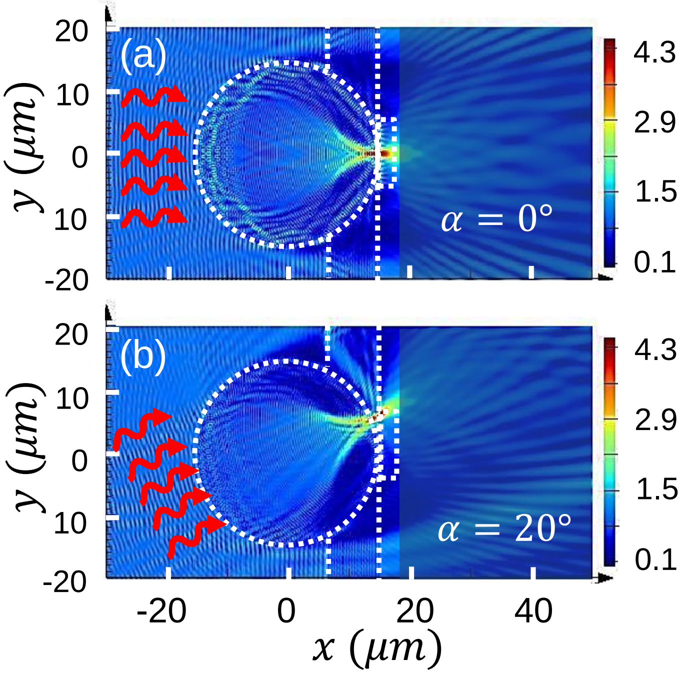

Figure 4. 12: (a,b) Electric field maps correspond to the configuration shown in Fig. 4.11 calculated at λ=4.0 μm for incidence angles α=0° and α=20°, respectively [320].

4.5: Conclusion

In this Chapter of dissertation, we propose to use photonic jets produced by the dielectric microspheres for focusing and highly efficient coupling light into individual photodetector mesas. The tasks consist in developing designs of corresponding structures based on two-dimensional finite-difference time domain modeling. We optimized the designs of such FPAs integrated with microspheres for achieving maximal angle of view (AOV) as a function of the index of refraction and diameter of the microspheres. The main results and conclusions are listed below:

- Using simplified two-dimensional finite difference time domain (FDTD) modeling we designed structures where the microspheres are partly-immersed in a layer of photoresist or slightly truncated by using controllable temperature melting effects.
- Using numerical modeling, we optimized our designs for achieving maximal AOVs for microspheres with different diameters in the 30-60 μm range, as well as various indices of refraction. It should be noted that the standard solution of the light collection efficiency problem is offered by the commercial microlens arrays. This solution, however, comes at a price of very narrow AOV~1-2° of the resulting mid-IR imaging system. We show that the microspheres allow combining high light collection efficiencies with larger AOVs

- We also designed MWIR FPAs for different geometrical and structural parameters of spheres, substrates and additional layers. The designs are aimed at progressively larger AOVs which can be achieved by reducing the effective focal distance of the microspheres. The designs are developed for both back- and front-illuminated FPAs.
- We demonstrate that by increasing the refractive index of microspheres, the AOV can be increased from 5° and 8° in back-illuminated designs to 20° in front-illuminated structures.
- Different techniques of fixing microspheres such as their partial immersion in photoresist or their slight deliberate truncation due to temperature treatment are considered in our designs. In all cases, the addition of microspheres should result in FPAs with increased SNR for the same aperture size and detector pitch.
- Our designs allow decreasing the sizes of photosensitive mesas down to wavelength-scale dimensions determined by the minimal waists of the focused beams produced by the dielectric microspheres, so-called photonic jets. This opens a principle possibility to reduce the dark current and increase the operating temperature of MWIR FPAs.

CHAPTER 5: LOCALAZED NANOPLASMONIC CONTRIBUTION TO SUPER RESOLUTION IMAGING BY DIELECTRIC MICROSPHERE

5.1: Introduction on Microspherical nanoscopy

Microspherical nanoscopy emerged in 2011 as a simple method of imaging nanoscale structures with a resolution which was shown to exceed the classical diffraction limit [154]. From the very beginning, the most crucial question underplaying this area was related to mechanisms of imaging through microspheres with resolution, which was shown to reach $\lambda/7$, where λ is the observation wavelength. Initially, it was proposed that the superrsolution imaging stems from the ultra-sharp focusing properties of dielectric microspheres, introduced in 2004 as so-called "photonic nanojet" [2]. Although this concept became popular among the researchers in this area, the size of the photonic nanojects is limited at $\lambda/3$ [2], where λ is the observation wavelength. In fact, in practical situations the calculated width of nanojets is larger than $\lambda/2$, and, consequently, this concept cannot explain such experimental resolution values as $\sim\lambda/7$. In addition, an analogy between the imaging and focusing properties of dielectric microspheres holds on a reciprocity principle in optics which stands only for the same modes propagating in forward and backward directions [331], whereas the modes involved in virtual imaging and focusing are significantly different.

The maximal far-field resolution can be estimated within a solid immersion lens (SIL) concept [121] as $\sim\lambda/(2\text{NA})$, where numerical aperture, $\text{NA}=n_0 \sin\theta$, is determined by the index of object-space (n_o) and the collection angle θ. In the case of silica microspheres (n_{sp}=1.46) in air considered in this work, this approach allows explaining resolution values up to ~λ/3.

It should be noted that in many cases where the superresolution was reported, the imaging was performed using nanostructured metallic objects such as circles, dimers, arrays of circles, or holes in metallic thin films [155, 167-169, 332]. In such objects, the optical near-fields can be resonantly enhanced at the wavelengths of localized surface plasmon resonances (LSPRs). In periodical arrays, the plasmonic dispersions can be back into the escape cone leading to the presence of high spatial frequencies in the escape cone [333]. In general, these conditions can be viewed as a precursor for achieving optical folded superresolution in a spirit of structured illumination microscopy (SIM) [334, 335]. It should be noted, however, that in contrast to SIM or LPSIM [168, 169, 336] where the high spatial frequency information about the object is usually obtained as a result of rather complicated postimaging processing, superresolution imaging of nanoplasmonic arrays through microspheres can be achieved without such processing. The theoretical mechanisms of such imaging are debated in the literature on this subject. Along with the abovementioned meachanisms, the resolution can be also enhanced due to a coherent imaging contributions which can take place under oblique incidence illumination [337, 338].

In this work, instead of using nanoplasmonic objects directly, we imaged dye-doped, fluorescent (FL) nanospheres placed at the top of periodic nanoplasmonic arrays. Due to a possibility to control the spectral overlap between the emission properties (the nanospheres were visible due their FL properties) and the resonant band of the array, we were able to test the hypotheses about the role of plasmonic properties in achieving the superresolution imaging of FL nanospheres. The emission band was controlled by selecting green or blue FL nanospheres. The resonant properties of the array were controlled by choosing nanoplasmonic structures made from different metals such as gold (Au) and aluminum (Al). Another feature of our experiments was that we tested arrays formed by the nanoplasmonic disks with different diameters, edge-to-edge separations, and periods. We directly prove that superresolution imaging requires a spectral overlap between the FL band of nanospheres and LSPRs peak position in nanoplasmonic arrays. We also show that the superresolution imaging is possible only for arrays with smallest characteristic dimensions (periods <150 nm).

5.2: Superresolution imaging experimental setup and samples

The geometry of our experiments is illustrated in Fig. 5.1 As objects for imaging, we used 100 nm polystyrene nanospheres which were either undoped or doped by incorporating dye molecules into polymer matrix (not surface dyed). The excitation/emission wavelengths of such FL nanospheres were 410 nm/455nm and 411 nm/510 nm with stokes shifts of 99 nm and 45 nm for the green and blue dyes respectively [339, 340]. The scanning electron microscopy (SEM) image of such particles self-assembled in a hexagonal array is illustrated in Fig. 5.2 (a).

The FL nanospheres were placed directly on top of the array, which consisted of Au or Al nanoplasmonic cylinders with 17 nm heights fabricated at the top of 3 nm Ti adhesive layer. The fabrication of nanoplasmonic arrays was performed at the Air Force Research Laboratory (AFRL) on a sapphire wafer using an electron beam lithography, metal evaporation, and e-beam photoresist lift-off process [159]. The diameter of Au or Al cylinders varied in different arrays between 60 nm<D<100 nm with the edge-to-edge separation of 0<g<50 nm. An array with the feature sizes, D = 60 nm and = 20 nm , is shown in Fig. 5.2 (b).

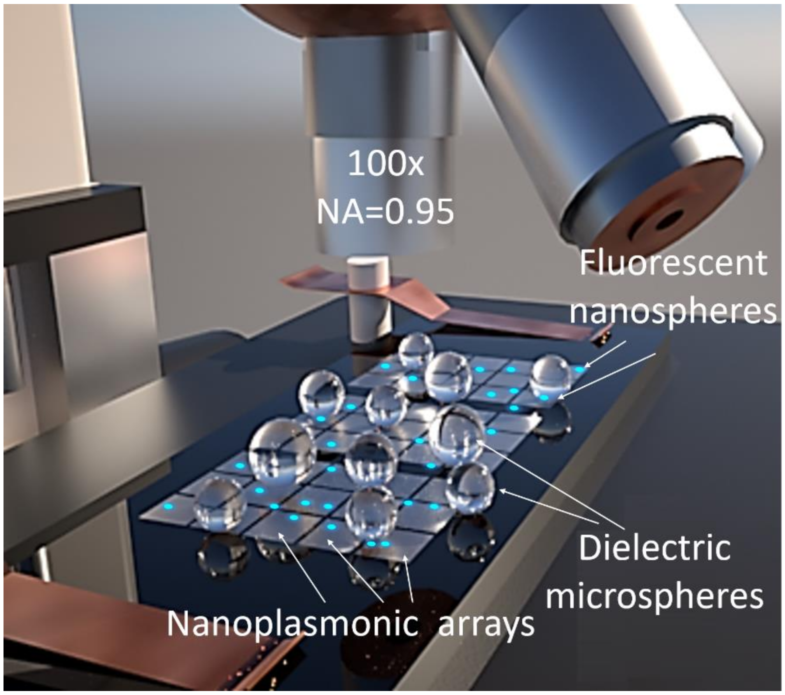

Figure 5. 1: Schematic of the experimental setup

As shown in Fig. 5.2 (c), the virtual image was created by borosilicate microspheres (n_{sph}~1.52) with diameters from 9 μm to 15 μm diameters placed in contact with the nanospheres. The virtual image can be seen at some depth into the substrate [154, 157, 159, 327, 341-347].

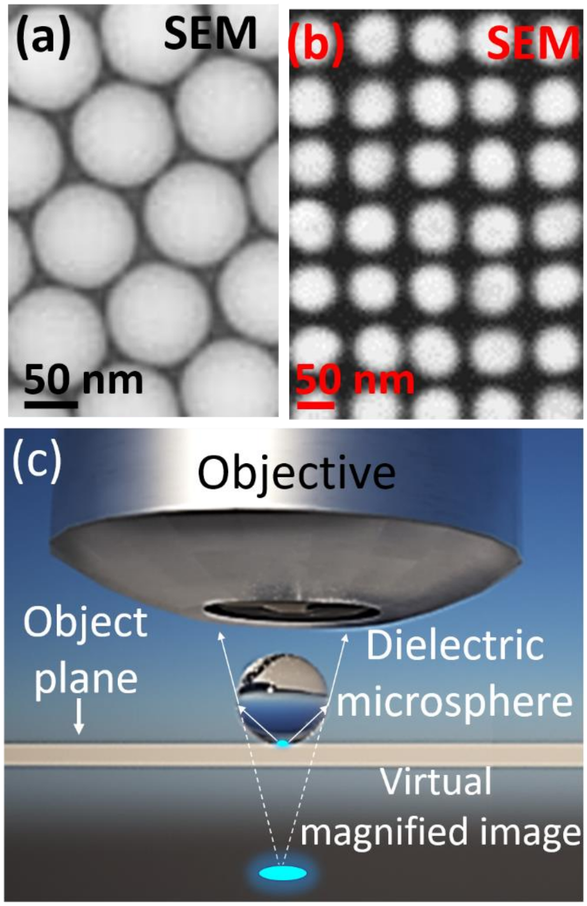

Figure 5. 2: SEM image of (a) 100 nm polystyrene nanosphere and (b) Au nanocylinder arrays with D= 60 nm and g=20 nm. (c) Virtual image formation.

Imaging was performed by a scanning laser confocal microscope Olympus LEXT-OLS4000. The nanospheres were visible due to their FL excited by the focused laser with the wavelength $\lambda = 405$ nm matching the absorption bands of dye molecules for both green and blue FL nanospheres. Imaging in air (outside microspheres) has a diffraction-limited resolution ~λ/2 determined by the microscope objective, 100 × (NA = 0.95).

5.3: Experimental definition of super-resolution

The virtual images of blue FL nanospheres obtained through borosicate microspheres with 9-15 μm diameters (Fig. 5.3 (a)) are illustrated in Fig. 5.3 (b). According to Houston criterion [348], the resolution was determined as a result of fitting the width of the Gaussian point-spread function (PSF) providing the best agreement of the calculated images with the experiment. Images (*I*) were calculated as a convolution of the two-dimensional (2-D) circular object (*O*) shown in Fig. 5.3 (c) with the 2-D PSF where we took into account the magnification (*M*) of the virtual image:

$$I(x,y) = \iint_{-\infty}^{+\infty} O(u,v)\, PSF\left(u - \frac{x}{M}, v - \frac{y}{M}\right) du\, dv. \qquad \mathbf{(1)}$$

The magnification can be estimated using geometrical optics [157] as $M(\acute{n},r,g) = \acute{n}/\{2(\acute{n}-1)(g/r) - \acute{n}\} \sim 3$, where we used $\acute{n} = n_{sp}/n_0 \sim 1.52$, as refractive index contrast between the sphere and the object space, $g = 0$ as the gap between the microsphere and the object, and $r = 7.5\ \mu m$ as microsphere radius. A typical example of comparison calculated (Fig. 5.3 (d)) and measured (Fig. 5.3 (e)) irradiance profiles is presented in Fig. 5.3 (f). The best fit corresponds to the PSF's full width at half maximum FWHM = $\lambda/5.7$ corresponding to the super-resolution of $d \sim 82\ nm$ according to the Houston's criterion [348].

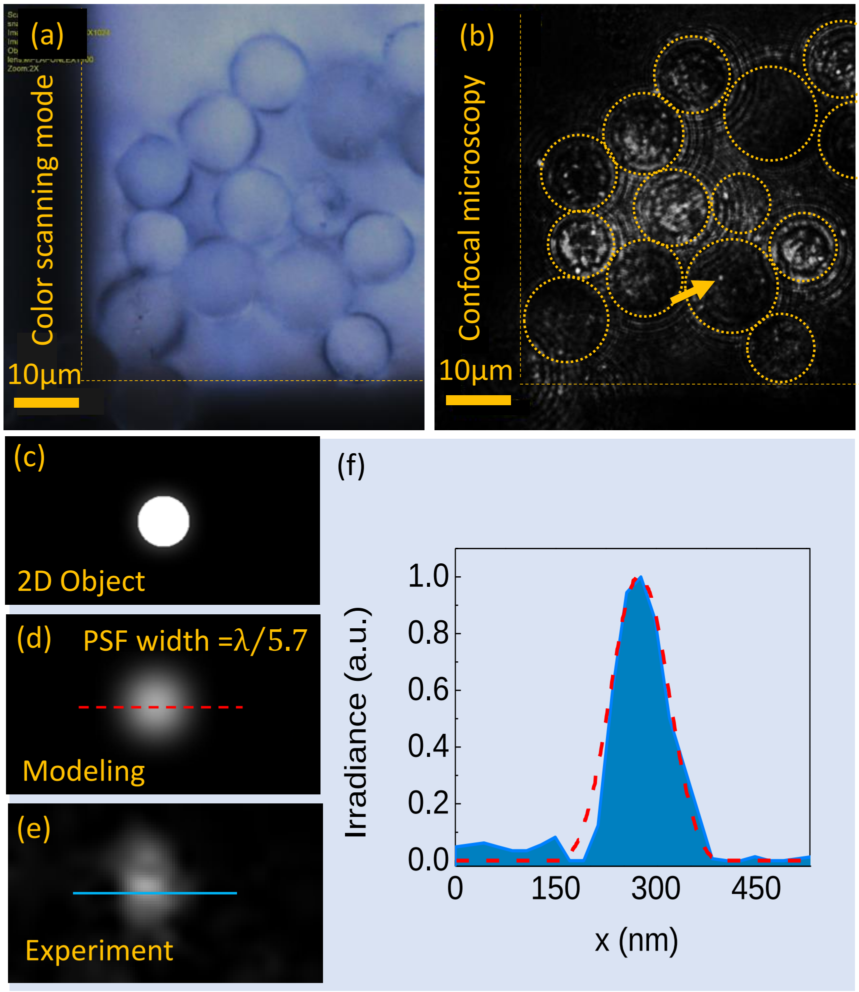

Figure 5. 3: (a) Image of the 9-15 µm borosilicate microspheres on top of the Al nanoplasmonic arrays. (b,e) Confocal virtual images of 100 nm blue FL nanospheres. (c) Circular 2-D object with 100 nm diameter and (d) its convolution with a 2-D PSF with FWHM of λ/5.7. (f) Comparison of the experimentally measured (blue background) and calculated (dashed red curve) irradiance profiles.

5.4: Experimental results and discussions

The inverse resolution (*λ*/*d*) is presented in Fig. 5.4 for blue, green, and undoped nanospheres placed on Au and Al arrays. Since the resolution values vary in different experiments due to use of different microspheres, difficulties of precise focusing at the plane of virtual image, and many other factors, it is seen that, generally, there is ~10% experimental error of determination resolution. At the same time, Fig. 5.4 shows some systematic trends with are reliably and systematically reproduced in our measurements. To begin our analyses, the resolution of dye-doped FL and undoped nanospheres placed on a sapphire substrate without metallic layer and observed through the borosilicate microspheres is found to be in a good agreement with the top estimates based on the SIL concept ($\sim\lambda/3$). Similar (or incrementally higher) resolution was found for all types of nanospheres on top of uniform Au layer, as seen in Fig. 5.4 (b). Patterning of both Au and Al arrays with sufficiently large periods (D=100 nm) and edge-to-edge separations ($g = 50\,nm$) does not result in a marked increase of the resolution compared to pure dielectric or uniform thin metal layer cases.

Here we reached the most interesting results observed with reduction of the characteristic feature sizes and periods of nanoplasmonic arrays. First of all, it is seen that obtaining the superresolution, which can be defined as increase of the height of the vertical bars over the level $\sim\lambda/3$ shown by dashed horizontal line, requires smaller feature sizes than D=100 nm and $g = 50\,nm$. This is especially clearly seen in the case of reducing characteristic dimensions of Al arrays in Fig. 5.4 (a) which shows that the resolution markedly exceeds the SIL limit already for D=80 nm and $g = 20\,nm$.

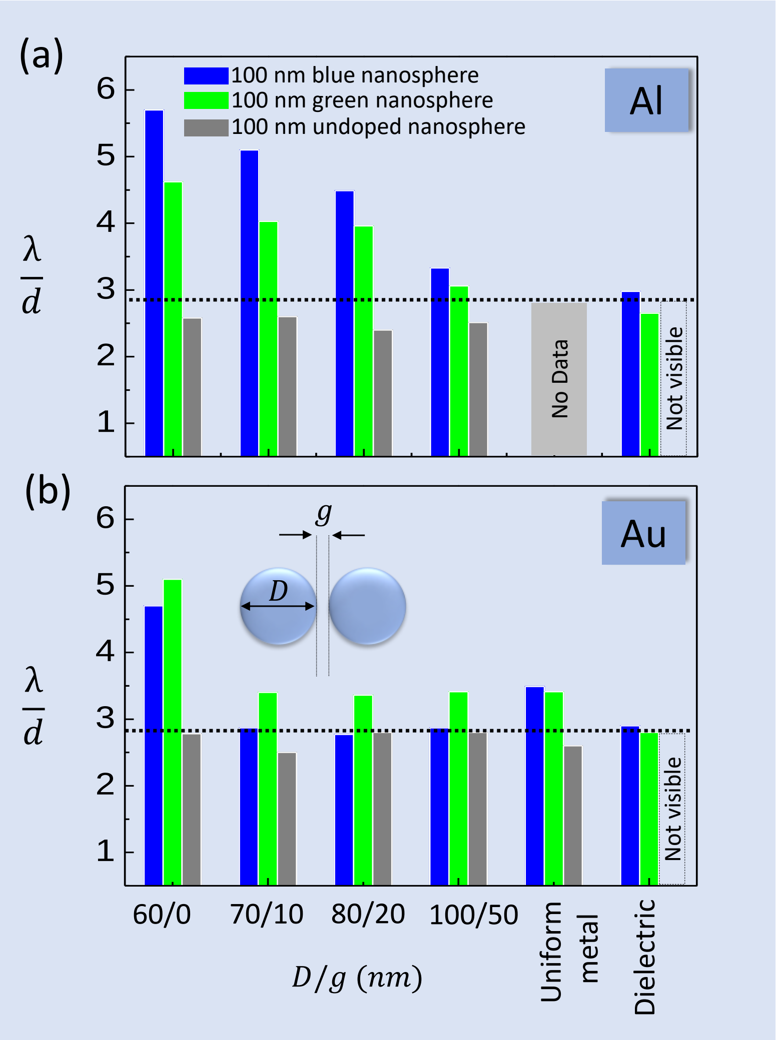

Figure 5. 4: Resolution comparison for green, blue, and undoped nanospheres on top of (a) Al and (b) Au arrays. Blue, green and gray bars represent blue FL, green FL and undoped nanospheres, respectively. The horizontal dashed line in each graph shows the resolution limited by the solid immersion lens concept $\sim\lambda/3$. The horizontal axis shows the variation in D and g for nanocylinder arrays. The cases of the uniform thin (17 nm) metal layer and pure sapphire substrate are also represented.

Further reduction of parameters D and g leads to reproducible and monotonous increase of the resolution far beyond the SIL limit of $\sim\lambda/3$. For the case of smallest feature sizes of D=60 nm with zero edge-to-edge separations, the resolution practically doubles compared to the SIL limit. The same tendency is seen for Au arrays in Fig. 5.4 (b), however, the significant increase of the resolution was detected only for the smallest feature sizes of D=60 nm with zero edge-to-edge separations. It should be noted that increase of the resolution takes place only for dye-dope nanospheres (blue and green bars), where emission is strongly coupled to the band-structure of the nanoplasmonic arrays. For undoped nanospheres (grey bars), the confocal image is obtained due to scattering of the focused laser at the excitation wavelength λ = 405 nm. One can assume that this type of imaging is outcoupled from the band-structure of the nanoplasmonic array since the resolution does not depend on the geometrical array parameters in this case.

Another and even more intriguing tendency is observed by comparing the resolution values as a function of the spectral overlap between the FL band of nanospheres with the plasmonic resonance properties of Au and Al arrays. Due to nanoscale diameters D of disks (with 17 nm height), we should speak about localized surface plasmon resonances (LSPR) rather than about propagating plasmons. The LSPR peaks are rather broad (with the typical widths ~20-40 nm) and they are dependent on the size quantization effects in such structures [177, 349]. However, in a simplified way, one can say that Au arrays tend to resonate in red-green region of visible, while Al arrays tend to resonate in blue.

This means that our resolution data summarized in Fig. 3 allows studying the role of spectral overlap between the FL and LSPR almost instantaneously. As it is seen in Fig. 5.4 (a), for Al arrays resonating in blue, all blue bars representing resolution of blue FL nanospheres are higher than the green bars. In contrast, as it is seen in Fig. 5.4 (b), for Au arrays resonating in green, almost all green bars representing resolution of green FL nanospheres are higher than the blue bars. Thus, this comparison provides a direct experimental evidence that coupling to nanoplasmonic is a key condition for achieving optical superresolution imaging through the dielectric microspheres.

The physical explanation of the mechanism of the observed superresolution can be related to efficient coupling of the nanospheres' emission to the diffraction orders of the nanoplasmonic array. Such coupling manifest itself due to directional emission and it is generally well known effect for such structures [333]. In this regard, this mechanism resembles the basic physics of localized plasmonic SIM and far-field superlens [350] due to the k-vector shift by $2\pi/a$, where a=D+ g is the array period. The difference with classical SIM [334] or localized plasmonic SIM [168, 169, 336] is that neither post-imaging processing nor additional optical components are required in our approach. It can be explained by the fact that FL is initially redirected into the diffraction orders in our case. With the reducing array feature sizes and reduced period, the statistically averaged distance between the emitter and the neighboring "plasmonic atoms" of the array gets smaller which increases the strength of coupling with the folded plasmonic dispersions. Under these conditions, the moiré' effect transferring information from higher spatial frequencies into the escape cone [333] becomes very pronounced and higher spatial frequencies can be accessed by focusing at the narrowest waist of the point-like objects. For this reason, building a complicated post-imaging processing for revealing such high spatial frequency information is not required in our case.

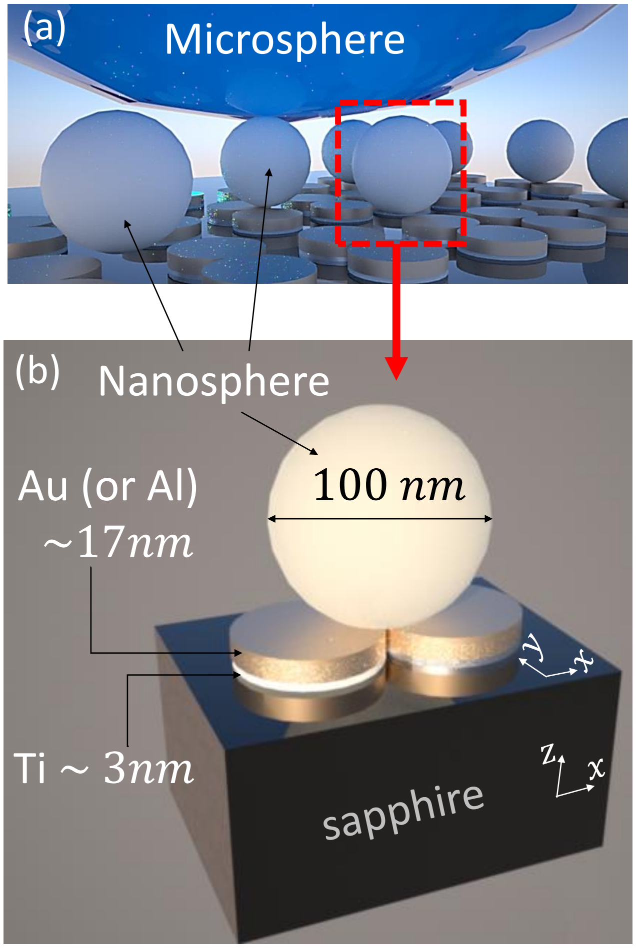

Figure 5. 5: (a,b) Schematic images showing metallic cylinders, nanospheres and microsphere

5.5: Modeling results for mapping of plasmonic near-fields

In the end of this work, in Fig. 5.5 we present results of a numerical modeling of Au and Al nanocylinder arrays which provides more precise description of their resonant properties generally consistent with a simplified qualitative picture presented above. In these calculations, we did not put a task of calculating any images, but simply estimated the magnitude of "hot spots" excited in two closely spaced Au (or Al) nanocylinders as a function of the excitation wavelength for the geometrical parameters corresponding to our experiments (D=60 nm, $g = 0\,nm$), see Figs. 5.5 (a) and 5.5 (b). The excitation of such coupled nanocylinders is provided by focusing incident plane waves at $\lambda = 405\,nm$ through very compact 100 nm microsphere into the region where two cylinders almost touch [349, 351, 352], [353]. The modeling is performed by a 3-D finite difference time domain modeling (FDTD) using Lumerical's "FDTD solutions" software. A range of 0.5 nm to 50 nm spatial Cartesian mesh size has been used at the nanometric gap to the bulk material to have sufficiently accurate filed calculation.

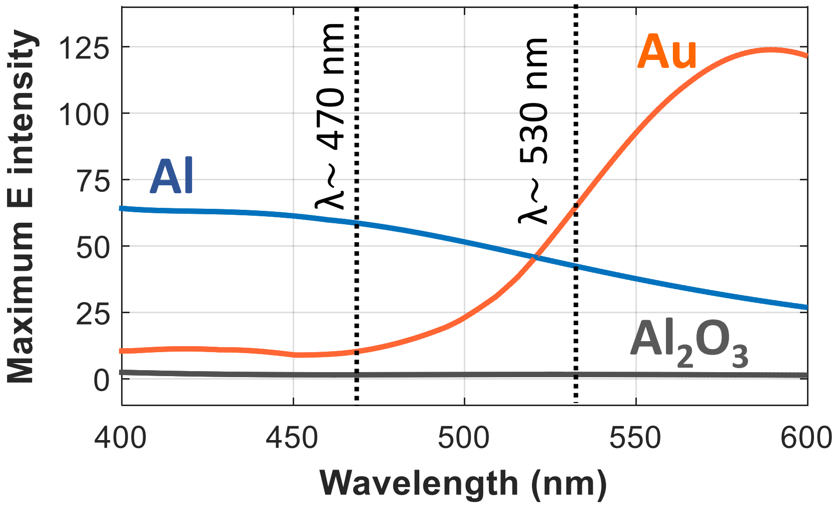

Figure 5. 6: Maximum electric field intensity calculated in the middle of the gap between the nanocylinders (n=1.6, k=0, D=100nm) made from Al, Au, and Al_2O_3.

In Fig. 5.6 we presented our simulation results for the near-filed generated by a nondispersive and nonabsorbing dielectric nanosphere (n = 1.6 and κ = 0) placed with 1 nm gap above two cylinders made from AL or Au corresponds to the Palik's material database. The normalized maximum electric field (E) distributions for a wavelength range of 400-600 nm were taken in the middle of the gap between the nanosphere and metallic nanoplasmonic arrays in x-y plane (Figs. 5.7 (a1-a6)) as well as in the cross section of the structure in x-z plane (Figs. 5.7 (b1-b4)).

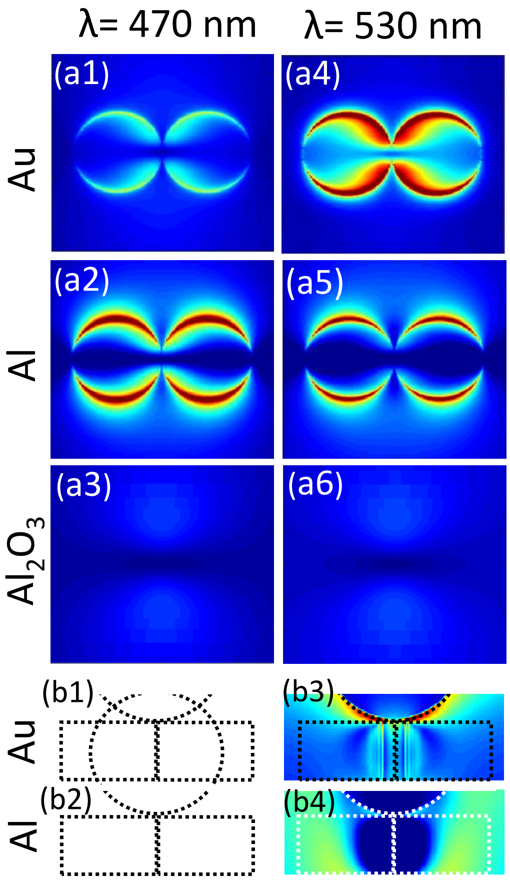

Figure 5. 7: Spatial filed distribution calculated (a_1-a_6) in the middle of the gap in x-y plane and (b_1-b_4) in the cross section of the structure in x-z plane.

As it was discussed previously, the calculated results show a good spectral overlap between the emission of blue (green) FL microspheres and LSPR in Al (Au) nanoplasmonic arrays.

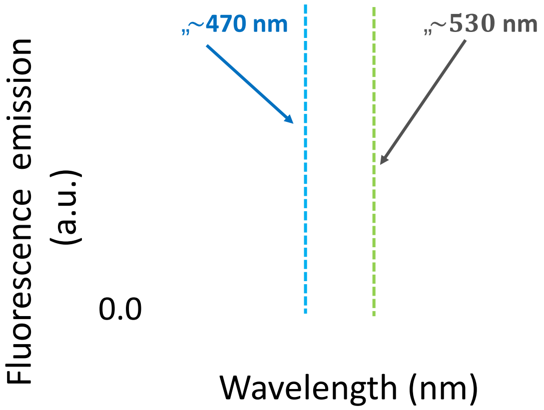

Figure 5. 8: The emission spectra for blue and green FL nanospheres. The blue and green vertical dashed lines in each spectrum represent the central wavelength (same area under the curve from the left and right side of the vertical line).

As it can be seen in Fig. 5.8, the emission spectra of the dyes are not symmetric around their maxima, therefore we found the effective wavelengths representing each case which turn to be 470 nm and 530 nm for blue and green dyes respectively. These are the wavelengths which we used to analyze the image resolution of fluorescent nanospheres. In Fig. 5.6, the maximum E in the middle of gap between the nanosphere and the substrate is compared for Al, Au, and Sapphire. It can be seen at λ= 470 nm the maximum E intensity is higher for Al compare to other cases, while at λ= 530 nm, Au overtakes in maximum E intensity.

As expected, the spatial distributions of electric filed in the middle of gap in Figs. 5.7 (a1-a6) (looking from top through the nanosphere) indicate the same information: the maximum filed enhancement can be seen at λ= 470 nm for Al in Fig. 5.7 (a2), and at λ= 530 nm for Au in Fig. 5.7 (a4). In both wavelengths, there is no filed enhancement regarding to Sapphire as a dielectric substrate in Figs. 5.7 (a3,a6). The plasmonic local filed enhancement at nano junctions between the Al (Au) nanocylinder arrays and dielectric nanosphere can be also seen in the E- field maps at x-z plane (Figs. 5.7 (b1-b4). Hot spots in these maps represent the near field interactions which clearly are noticeable at λ= 470 nm for Al (Fig. 5.7 (b2)), and at λ= 530 nm for Au nanocylinders (Fig. 5.7 (b3)). Hence, the influence of the metallic substrate supports the statement that near field enhancement in the nanosized gap is due to the excitation and localization of surface plasmons of the metallic nanocylinder coupled to dielectric nanosphere on top. Such enhanced near filed can be efficiently coupled to the microsphere which launching the image to the far filed [354-356].

5.6: Conclusion

In this chapter of the dissertation, we studied the role of the nanoplasmonic array on supper resolution microscopy for point-like fluorescent (FL) nanospheres using contact microlenses compared to standard microscopy. Without using nanoplasmonic arrays, the experimental resolution approaches the solid immersion lens limit ~$\lambda/2n_{sp}$. However, by virtual imaging of FL nanospheres through microspheres, using nanoplasmonic structured illumination we are able to go beyond the diffraction limit. In our experiment, the geometrical parameters and material of nanoplasmonic arrays were varied to study the nanoplasmonic contributions to the resolution of FL nanospheres. The main results and conclusions are listed below:

- We investigated several combinations of spectral emission bands (blue, green FL, and non-FL nanospheres) with various spectral positions of localized surface plasmonic resonances (LSPRs) in the Au and Al arrays.
- It was demonstrated that the resolution about λ/7, where λ is the emission wavelength, can be obtained under conditions of spectral overlap between the Fl band of nanospheres and LSPRs in the arrays. for Al arrays resonating in blue, all the resolutions for blue FL nanospheres are higher than the green FL nanospheres. In contrast, for Au arrays resonating in green, almost all the resolutions of green FL nanospheres are higher than the blue FL nanospheres. Consequently, this comparison provided us direct experimental evidence that coupling to nanoplasmonics is a key condition for achieving optical superresolution imaging through the dielectric microspheres
- We showed that achieving superresolution also requires sufficiently small feature sizes and periods of the nanoplasmonic arrays. With the reducing array feature sizes and reduced period, the statistically

averaged distance between the emitter and the neighboring "plasmonic atoms" of the array gets smaller which increases the strength of coupling with the folded plasmonic dispersions.

- We also presented the results of numerical modeling of Au and Al nanocylinder arrays to provide a more precise description of their resonant properties.
- In our modeling calculations, we did put a task of calculating the estimated magnitude of "hot spots" excited in two closely spaced Au (or Al) nanocylinders as a function of the excitation wavelength for the geometrical parameters corresponding to our experiments (D=60 nm, g = 0),
- The calculated results showed a good spectral overlap between the emission of blue (green) FL microspheres and LSPR in Al (Au) nanoplasmonic arrays, in such a way that the maximum field enhancement can be realized at λ= 470 nm for Al, and at λ= 530 nm for Au. In both wavelengths, there was no filed enhancement regarding Sapphire as a dielectric substrate.
- We experimentally showed the influence of the metallic substrate leads to the near-field enhancement in the nanosized gap, due to the excitation and localization of surface plasmons of the metallic nanocylinder coupled to dielectric nanosphere on top. Such enhanced near filed can be

efficiently coupled to the microsphere which launching the super resolved image to the far filed.

CHAPTER 6: CONCLUSIONS AND OUTLOOK

In Chapter 2, we theoretically considered the optical properties of strongly coupled WGMs of photonic molecules formed by different configurations of identical photonic atoms. The modeling of WGM processes in photonic molecules was performed using a commercial FDTD software Lumerical in a simplified 2-D geometry for identical circular resonators with identical dimensions and refractive index contrasts similar to that used in the experimental situations. We studied the spectral properties of such photonic molecular structures based on calculations of transmission spectra through the stripe waveguide side coupled to one of the resonators comprising a given molecule. We proposed the concept of spectral signature associated with each molecular configuration as a relatively stable property which allows distinguishing between different molecules based on their spectra. The number of split supermodes and their spectral positions were studied based on the side-coupled fiber transmission spectra for 1-D and 2-D molecules formed by multiple atoms. Spectral signature can be used as a unique feature for recognizing spatial configuration of a given molecule. It can find applications in position sensing as well as anticounterfeit technology.

We proposed the concept of spectral signature as a unique feature associated with each molecular configuration as a relatively stable property which allows distinguishing between different molecules based on their spectra. The number of split supermodes and their spectral positions were studied based on the side-coupled fiber transmission spectra for 1-D and 2-D molecules formed by multiple photonic atoms. Since we used the numerical methods we cannot claim that these “spectral features” or “spectral signatures” are universal characteristics of the given molecules, but we tested that these features persist in their spectra in a certain relativity broad range of variation of parameters. Moreover, we demonstrated good agreement between the FDTD simulated and experimentally measured spectra for both 1-D chain and 2-D planar molecules.

Photonic molecules also showed Q-factor enhancement for some of the antibonding modes and the mini-band formed by a series of overlapped supermodes. Therefore, the spectrum of the molecule can be engineered, providing additional freedom in design of lasing devices, narrow line filters, delay lines and multi-wavelength sensors. The E-field enhancement in the medium surrounding certain molecular configurations provides larger detecting volume and higher sensitivity comparing to typical WGM-based sensors of a single cavity.

In Chapter 3, we provided comprehensive studies for the transmission and routing properties of side-coupled circular cavity systems based on two-dimensional finite-difference time domain modeling. In this study, we investigated the directional properties of the optical transport in an on-chip dissipative system of passive circular microresonators side-coupled to stripe-waveguides as 4-port routers by introducing uneven gaps separating circular resonators from the stripe-waveguides. It was demonstrated that spatially asymmetric and lossy systems have asymmetric optical transmission properties for the waves propagating in forward and backward directions between the ports.

We demonstrated for non-optimized single microcavity structures that introducing the spatial asymmetry results in isolation ratios (the ratio of transmission in forward and backward directions between the same ports) on the order of 10 dB for wavelengths resonant with WGMs.

We also studied the optical connectivity between different ports in more complicated structures where two identical circular resonators are strongly coupled resulting in formation of bonding and antibonding molecular modes. It is shown that at the wavelengths resonant with hybridized molecular modes the isolation ratios can be increased beyond 20 dB.

Our calculation for E-filed distribution of resonant bonding and antibonding modes in double resonators structure shows the possibility of controlling the path of different modes, in such a way that different wavelengths can be preferentially coupled to different ports. Therefore, the direction of optical coupling between the ports become frequency dependent. This opens principle possibilities to design a structure with wavelength demultiplexing functionality, and we demonstrated bigger that 10 dB path ratio difference for resonant routing between different ports in such structures.

To compensate the optical losses in such structures, we also introduced a linear gain to the compact circular resonators which exhibited remarkable isolation performance with restored forward transmitted signal in contrast with sufficiently weak backward transmitted one. Also our modeling shows that the double-microresonator photonic molecule is capable of selectively amplifying different modes with significant IR factor.

The structures considered in Chapter 3 do not possess nonreciprocity in a true sense; However, the structures do have a combination of routing, wavelength demultiplexing, and asymmetric optical transport properties which can be very useful for developing chip-scale telecom and sensor devices. The ports in such structures can be connected in narrow spectral ranges and in only one direction or in both directions. As it mentioned above, fundamentally, this is determined by many factors such as the mode conversion and coupling through asymmetric gaps, strong asymmetric losses, and a few-mode input.

In Chapter 4, we designed and optimized different microsphere lenses to increase the light collection efficiency, and angle-of-view of MWIR FPAs at for operation at higher temperature. This study was along with the previous work of the Mesophotonics Lab which proposed to use the “photonic jets”, sharply focused beams with subwavelength transversal width produced by dielectric microspheres [120, 296, 318, 357, 358]. In this Chapter, using numerical modeling, we optimized our designs for achieving maximal AOVs for microspheres with different diameters in the 30-60 μm range, as well as various indices of refraction. It should be noted that the standard solution of the light collection efficiency problem is offered by the commercial microlens arrays. This solution, however, comes at a price of very narrow AOV~1-2° of the resulting mid-IR imaging system. We have shown that the microspheres allow combining high light collection efficiencies with larger AOVs.

In this work, we also designed MWIR FPAs for different geometrical and structural parameters of spheres, substrates and additional layers. The designs are aimed at progressively larger AOVs which can be achieved by reducing the effective focal distance of the microspheres. The designs are developed for both back- and front-illuminated FPAs. We demonstrate that by increasing the refractive index of microspheres, the AOV can be increased from 5° and 8° in back-illuminated designs to 20° in front-illuminated structures. Different techniques of fixing microspheres such as their partial immersion in photoresist or their slight deliberate truncation due to temperature treatment are considered in our designs. In all cases, the addition of microspheres should result in FPAs with increased SNR for the same aperture size and detector pitch.

In Chapter 5, we studied the nanoplasmonic contributions to the resolution of nanoscale structures in microspherical nanoscopy. The microsphere plays a role of dielectric lens picking the objects' near-fields and to project them in the far-fields and, simultaneously, an antenna which creates a virtual image located at larger focusing depth below the sample surface. We experimentally studied the role of structured illumination of nanoscale objects by nanoplasmonic arrays fabricated on a substrate on super-resolution microscopy. By looking into spectral and spatial characteristics of such coupling between fluorescent dielectric nanospheres and nanoscale metallic arrays we came to the conclusion that localized surface plasmon resonances play an essential role in mechanisms of superresolution imaging properties of such structures.

REFERENCES

[1] W. G. M. M.Gomilšek, University of Ljubljana, Ljubljana, Seminar 2011.

[2] Z. Chen, A. Taflove, and V. Backman, "Photonic nanojet enhancement of backscattering of light by nanoparticles: a potential novel visible-light ultramicroscopy technique," *Optics Express,* vol. 12, no. 7, pp. 1214-1220, 2004/04/05 2004.

[3] S. V. Boriskina, "Photonic molecules and spectral engineering," *Chapter 16, Photonic Microresonator Research and Applications Springer Series in Optical Sciences,* 156, 393-421 (2010).

[4] Y. Li *et al.*, "Whispering gallery mode hybridization in photonic molecules," *Laser & Photonics Reviews,* vol. 11, no. 2, 2017.

[5] B. E. Saleh, M. C. Teich, and B. E. Saleh, *Fundamentals of photonics*. Wiley New York, 1991.

[6] L. Rayleigh, "CXII. The problem of the whispering gallery," *The London, Edinburgh, and Dublin Philosophical Magazine and Journal of Science,* vol. 20, no. 120, pp. 1001-1004, 1910/12/01 1910.

[7] V. Ginis and P. Tassin, "Transformation optics beyond the manipulation of light trajectories," *Philosophical Transactions of the Royal Society A: Mathematical, Physical and Engineering Sciences,* vol. 373, no. 2049, 2015.

[8] R. D. Richtmyer, "Dielectric Resonators," *Journal of Applied Physics,* vol. 10, no. 6, pp. 391-398, 1939.

[9] C. G. B. Garrett, W. Kaiser, and W. L. Bond, "Stimulated Emission into Optical Whispering Modes of Spheres," *Physical Review,* vol. 124, no. 6, pp. 1807-1809, 12/15/ 1961.

[10] K. Srinivasan, P. E. Barclay, O. Painter, J. Chen, A. Y. Cho, and C. Gmachl, "Experimental demonstration of a high quality factor photonic crystal microcavity," *Applied Physics Letters,* vol. 83, no. 10, pp. 1915-1917, 2003.

[11] N. Lin *et al.*, "Ultrasensitive chemical sensors based on whispering gallery modes in a microsphere coated with zeolite," *Applied Optics,* vol. 49, no. 33, pp. 6463-6471, 2010/11/20 2010.

[12] N. Lin, L. Jiang, S. Wang, H. Xiao, Y. Lu, and H. Tsai, "Thermostable refractive index sensors based on whispering gallery modes in a microsphere coated with poly(methyl methacrylate)," *Applied Optics,* vol. 50, no. 7, pp. 992-998, 2011/03/01 2011.

[13] F. Treussart, "Etude expérimentale de l'effet laser dans des microsphères de silice dopées avec des ions neodyme," Université Pierre et Marie Curie - Paris VI, 1997.

[14] M. L. Gorodetsky, A. A. Savchenkov, and V. S. Ilchenko, "Ultimate Q of optical microsphere resonators," *Optics Letters,* vol. 21, no. 7, pp. 453-455, 1996/04/01 1996.

[15] A. A. Savchenkov, A. B. Matsko, V. S. Ilchenko, and L. Maleki, "Optical resonators with ten million finesse," *Optics Express,* vol. 15, no. 11, pp. 6768-6773, 2007/05/28 2007.

[16] Y. Dumeige, S. Trebaol, L. Ghişa, T. K. N. Nguyên, H. Tavernier, and P. Féron, "Determination of coupling regime of high-Q resonators and optical gain of highly selective amplifiers," *Journal of the Optical Society of America B,* vol. 25, no. 12, pp. 2073-2080, 2008/12/01 2008.

[17] V. d. H. H., "Optics of Spherical Particles (Drukkerij J.F. Duwaer)," 1946.

[18] B. M. a. W. E., *Principles of Optics (Pergamon)*. 1980.

[19] R. S. Stein and R. L. Rowell, "The Scattering of Light and Other Electromagnetic Radiation. Milton Kerker. Academic Press, New York, 1969. xviii + 670 pp., illus. $33.50," *Science,* vol. 167, no. 3919, pp. 861-861, 1970.

[20] J. A. Stratton, *Theorie de l'electromagnetisme: trad. par J. Hebenstreit*. Dunod, 1961.

[21] S. Schiller and R. L. Byer, "High-resolution spectroscopy of whispering gallery modes in large dielectric spheres," *Optics Letters,* vol. 16, no. 15, pp. 1138-1140, 1991/08/01 1991.

[22] M. L. Gorodetsky and A. E. Fomin, "Geometrical theory of whispering-gallery modes," *IEEE Journal of Selected Topics in Quantum Electronics,* vol. 12, no. 1, pp. 33-39, 2006.

[23] S. Trebaol, "Theoretical and experimental study on the dispersive properties of photonic structures based on microresonators," Université Rennes 1, 2010.

[24] I. M. White, H. Oveys, and X. Fan, "Liquid-core optical ring-resonator sensors," *Optics Letters,* vol. 31, no. 9, pp. 1319-1321, 2006/05/01 2006.

[25] S. I. Shopova, G. Farca, A. T. Rosenberger, W. M. S. Wickramanayake, and N. A. Kotov, "Microsphere whispering-gallery-mode laser using HgTe quantum dots," *Applied Physics Letters,* vol. 85, no. 25, pp. 6101-6103, 2004.

[26] V. R. Dantham and P. B. Bisht, "High-Q whispering gallery modes of doped and coated single microspheres and their effect on radiative rate," *Journal of the Optical Society of America B,* vol. 26, no. 2, pp. 290-300, 2009/02/01 2009.

[27] S. Soria *et al.*, "High-Q polymer-coated microspheres for immunosensing applications," *Optics Express,* vol. 17, no. 17, pp. 14694-14699, 2009/08/17 2009.

[28] C.-H. Dong, F.-W. Sun, C.-L. Zou, X.-F. Ren, G.-C. Guo, and Z.-F. Han, "High-Q silica microsphere by poly(methyl methacrylate) coating and modifying," *Applied Physics Letters,* vol. 96, no. 6, p. 061106, 2010.

[29] T. A. Birks, J. C. Knight, and T. E. Dimmick, "High-resolution measurement of the fiber diameter variations using whispering gallery modes and no optical alignment," *IEEE Photonics Technology Letters,* vol. 12, no. 2, pp. 182-183, 2000.

[30] C. A. *et al.*, "Spherical whispering-gallery-mode microresonators," *Laser & Photonics Reviews,* vol. 4, no. 3, pp. 457-482, 2010.

[31] W. J. and B. O., "WGM microresonators: sensing, lasing and fundamental optics with microspheres," *Laser & Photonics Reviews,* vol. 5, no. 4, pp. 553-570, 2011.

[32] M. Sumetsky, "Whispering gallery modes in a microfiber coil with an n-fold helical symmetry: classical dynamics, stochasticity, long period gratings, and wave parametric resonance," *Optics Express,* vol. 18, no. 3, pp. 2413-2425, 2010/02/01 2010.

[33] C. Fietz and G. Shvets, "Nonlinear polarization conversion using microring resonators," *Optics Letters,* vol. 32, no. 12, pp. 1683-1685, 2007/06/15 2007.

[34] M. Borselli, K. Srinivasan, P. E. Barclay, and O. Painter, "Rayleigh scattering, mode coupling, and optical loss in silicon microdisks," *Applied Physics Letters,* vol. 85, no. 17, pp. 3693-3695, 2004.

[35] D. K. Armani, T. J. Kippenberg, S. M. Spillane, and K. J. Vahala, "Ultra-high-Q toroid microcavity on a chip," *Nature,* vol. 421, p. 925, 02/27/online 2003.

[36] Z. Shen, C.-H. Dong, Y. Chen, Y.-F. Xiao, F.-W. Sun, and G.-C. Guo, "Compensation of the Kerr effect for transient optomechanically induced transparency in a silica microsphere," *Optics Letters,* vol. 41, no. 6, pp. 1249-1252, 2016/03/15 2016.

[37] T. J. Kippenberg, S. M. Spillane, and K. J. Vahala, "Kerr-Nonlinearity Optical Parametric Oscillation in an Ultrahigh-Q Toroid Microcavity," *Physical Review Letters,* vol. 93, no. 8, p. 083904, 08/19/ 2004.

[38] M. Hossein-Zadeh and K. J. Vahala, "Free ultra-high-Q microtoroid: a tool for designing photonic devices," *Optics Express,* vol. 15, no. 1, pp. 166-175, 2007/01/08 2007.

[39] S.-H. Kim, G.-H. Kim, S.-K. Kim, H.-G. Park, Y.-H. Lee, and S.-B. Kim, "Characteristics of a stick waveguide resonator in a two-dimensional photonic crystal slab," *Journal of Applied Physics,* vol. 95, no. 2, pp. 411-416, 2004.

[40] F. Diebel, P. Rose, M. Boguslawski, and C. Denz, "Optical induction scheme for assembling nondiffracting aperiodic Vogel spirals," *Applied Physics Letters,* vol. 104, no. 19, p. 191101, 2014.

[41] M. Sumetsky, "Whispering-gallery-bottle microcavities: the three-dimensional etalon," *Optics Letters,* vol. 29, no. 1, pp. 8-10, 2004/01/01 2004.

[42] G. S. Murugan, J. S. Wilkinson, and M. N. Zervas, "Optical excitation and probing of whispering gallery modes in bottle microresonators: potential for all-fiber add–drop filters," *Optics Letters,* vol. 35, no. 11, pp. 1893-1895, 2010/06/01 2010.

[43] M. Sumetsky, Y. Dulashko, and R. S. Windeler, "Optical microbubble resonator," *Optics Letters,* vol. 35, no. 7, pp. 898-900, 2010/04/01 2010.

[44] H. Li, Y. Guo, Y. Sun, K. Reddy, and X. Fan, "Analysis of single nanoparticle detection by using 3-dimensionally confined optofluidic ring resonators," *Optics Express,* vol. 18, no. 24, pp. 25081-25088, 2010/11/22 2010.

[45] W. G. M. m. o. a. Si-chip. *INSTITUT NANOSCIENCES ET CRYOGÉNIE,* *http://inac.cea.fr/Phocea/Vie_des_labos/Ast/ast_visu.php?id_ast=844*. Available: http://inac.cea.fr/Phocea/Vie_des_labos/Ast/ast_visu.php?id_ast=844

[46] h. w. m.-s. c. p. h. MO-SCI Corporation.

[47] h. w. t. c. c. t. e. p. p.-t. h. Thermo Fisher Scientific Inc.

[48] L. Collot, V. Lefèvre-Seguin, M. Brune, J. M. Raimond, and S. Haroche, "Very High- Q Whispering-Gallery Mode Resonances Observed on Fused Silica Microspheres," *EPL (Europhysics Letters),* vol. 23, no. 5, p. 327, 1993.

[49] D. W. Vernooy, V. S. Ilchenko, H. Mabuchi, E. W. Streed, and H. J. Kimble, "High-Q measurements of fused-silica microspheres in the near infrared," *Optics Letters,* vol. 23, no. 4, pp. 247-249, 1998/02/15 1998.

[50] E. S. C. CHING, P. T. LEUNG, and K. YOUNG, "Optical Processes in Microcavities — The Role of Quasinormal Modes," in *Optical Processes in Microcavities*: WORLD SCIENTIFIC, 2011, pp. 1-75.

[51] R. K. C. a. A. J. Campillo, *[Optical Processes in Microcavities], Singapore: World Scientific*. 1996.

[52] L. D. Tobing, P., *Fundamental Principles of Operation and Notes on Fabrication of Photonic Microresonators*. Photonic Microresonator Research and Applications 156, 1-27, 2010.

[53] N. O. Anatolii, "Whispering-gallery waves," *Quantum Electronics,* vol. 32, no. 5, p. 377, 2002.

[54] T. Kippenberg, "Nonlinear Optics in Ultra-high-Q Whispering-Gallery Optical Micro-cavities," *Ph. D. Thesis, California Institute of Technology, Pasadena,* (2004), Chap. 3.

[55] O. S. Ioannis Chremmos, Nikolaos Uzunoglu, Ed. *Photonic Microresonator Research and Applications*. Springer Series in Optical Sciences (SSOS, volume 156), 2010.

[56] V. N. Astratov, "Fundamentals and Applications of Microsphere Resonator Circuits," in *Photonic Microresonator Research and*

Applications, I. Chremmos, O. Schwelb, and N. Uzunoglu, Eds. Boston, MA: Springer US, 2010, pp. 423-457.

[57] S. Yang and V. Astratov, *Spectroscopy of photonic molecular states in supermonodispersive bispheres*. 2009.

[58] S. Yang and V. N. Astratov, "Spectroscopy of coherently coupled whispering-gallery modes in size-matched bispheres assembled on a substrate," *Optics Letters,* vol. 34, no. 13, pp. 2057-2059, 2009/07/01 2009.

[59] A. Majkić, M. Koechlin, G. Poberaj, and P. Günter, "Optical microring resonators in fluorine-implanted lithium niobate," *Optics Express,* vol. 16, no. 12, pp. 8769-8779, 2008/06/09 2008.

[60] M. Hammer, K. R. Hiremath, and R. Stoffer, "Analytical Approaches to the Description of Optical Microresonator Devices," *AIP Conference Proceedings,* vol. 709, no. 1, pp. 48-71, 2004.

[61] G. Righini *et al.*, "Whispering gallery mode microresonators : Fundamentals and applications," (in English), *Rivista del Nuovo Cimento,* vol. 34, no. 7, p. 435, 2011-07 2011.

[62] C. C. Lam, P. T. Leung, and K. Young, "Explicit asymptotic formulas for the positions, widths, and strengths of resonances in Mie scattering," *Journal of the Optical Society of America B,* vol. 9, no. 9, pp. 1585-1592, 1992/09/01 1992.

[63] W. Pongruengkiat and S. Pechprasarn, "Whispering-Gallery Mode Resonators for Detecting Cancer," *Sensors,* vol. 17, no. 9, p. 2095, 2017.

[64] V. B. Braginsky, M. L. Gorodetsky, and V. S. Ilchenko, "Quality-factor and nonlinear properties of optical whispering-gallery modes," *Physics Letters A,* vol. 137, no. 7, pp. 393-397, 1989/05/29/ 1989.

[65] M. L. Gorodetsky and V. S. Ilchenko, "Optical microsphere resonators: optimal coupling to high-Q whispering-gallery modes," *Journal of the Optical Society of America B,* vol. 16, no. 1, pp. 147-154, 1999/01/01 1999.

[66] F. Treussart *et al.*, "Evidence for intrinsic Kerr bistability of high-Q microsphere resonators in superfluid helium," *The European Physical Journal D - Atomic, Molecular, Optical and Plasma Physics,* journal article vol. 1, no. 3, pp. 235-238, April 01 1998.

[67] R. Ulrich, "Optimum Excitation of Optical Surface Waves," *Journal of the Optical Society of America,* vol. 61, no. 11, pp. 1467-1477, 1971/11/01 1971.

[68] H. Chandrahalim, S. C. Rand, and X. Fan, "Evanescent coupling between refillable ring resonators and laser-inscribed optical waveguides," *Applied Optics,* vol. 56, no. 16, pp. 4750-4756, 2017/06/01 2017.

[69] V. S. Ilchenko, X. S. Yao, and L. Maleki, "Pigtailing the high-Q microsphere cavity:?a simple fiber coupler for optical whispering-

gallery modes," *Optics Letters,* vol. 24, no. 11, pp. 723-725, 1999/06/01 1999.

[70] M. K. Park *et al.*, "Label-free aptamer sensor based on silicon microring resonators," *Sensors and Actuators B: Chemical,* vol. 176, pp. 552-559, 2013/01/01/ 2013.

[71] L. Zhou, X. Sun, X. Li, and J. Chen, "Miniature Microring Resonator Sensor Based on a Hybrid Plasmonic Waveguide," *Sensors,* vol. 11, no. 7, p. 6856, 2011.

[72] B. E. Little, J. P. Laine, and H. A. Haus, "Analytic theory of coupling from tapered fibers and half-blocks into microsphere resonators," *Journal of Lightwave Technology,* vol. 17, no. 4, pp. 704-715, 1999.

[73] M. Cai, O. Painter, and K. J. Vahala, "Observation of Critical Coupling in a Fiber Taper to a Silica-Microsphere Whispering-Gallery Mode System," *Physical Review Letters,* vol. 85, no. 1, pp. 74-77, 07/03/ 2000.

[74] M. Cai and K. Vahala, "Highly efficient optical power transfer to whispering-gallery modes by use of a symmetrical dual-coupling configuration," *Optics Letters,* vol. 25, no. 4, pp. 260-262, 2000/02/15 2000.

[75] A. Yariv, "Universal relations for coupling of optical power between microresonators and dielectric waveguides," *Electronics Letters,* vol. 36, no. 4, pp. 321-322, 2000.

[76] S. Arnold, J. Comunale, W. B. Whitten, J. M. Ramsey, and K. A. Fuller, "Room-temperature microparticle-based persistent hole-burning spectroscopy," *Journal of the Optical Society of America B,* vol. 9, no. 5, pp. 819-824, 1992/05/01 1992.

[77] T. M. Benson, S. V. Boriskina, P. Sewell, A. Vukovic, S. C. Greedy, and A. I. Nosich, "MICRO-OPTICAL RESONATORS FOR MICROLASERS AND INTEGRATED OPTOELECTRONICS," Dordrecht, 2006, pp. 39-70: Springer Netherlands.

[78] S. V. Boriskina, "Photonic Molecules and Spectral Engineering," in *Photonic Microresonator Research and Applications*, I. Chremmos, O. Schwelb, and N. Uzunoglu, Eds. Boston, MA: Springer US, 2010, pp. 393-421.

[79] H. Miyazaki and Y. Jimba, "Ab initio tight-binding description of morphology-dependent resonance in a bisphere," *Physical Review B,* vol. 62, no. 12, pp. 7976-7997, 09/15/ 2000.

[80] K. A. Fuller, "Optical resonances and two-sphere systems," *Applied Optics,* vol. 30, no. 33, pp. 4716-4731, 1991/11/20 1991.

[81] Y. Hara, T. Mukaiyama, K. Takeda, and M. Kuwata-Gonokami, "Heavy Photon States in Photonic Chains of Resonantly Coupled Cavities with Supermonodispersive Microspheres," *Physical Review Letters,* vol. 94, no. 20, p. 203905, 05/26/ 2005.

[82] N. Le Thomas, U. Woggon, W. Langbein, and M. V. Artemyev, "Effect of a dielectric substrate on whispering-gallery-mode sensors," *Journal*

of the Optical Society of America B, vol. 23, no. 11, pp. 2361-2365, 2006/11/01 2006.

[83] H. Dötsch *et al.*, "Applications of magneto-optical waveguides in integrated optics: review," *Journal of the Optical Society of America B,* vol. 22, no. 1, pp. 240-253, 2005/01/01 2005.

[84] M. Levy, "Nanomagnetic route to bias-magnet-free, on-chip Faraday rotators," *Journal of the Optical Society of America B,* vol. 22, no. 1, pp. 254-260, 2005/01/01 2005.

[85] L. Bi *et al.*, "On-chip optical isolation in monolithically integrated non-reciprocal optical resonators," *Nature Photonics,* vol. 5, p. 758, 11/13/online 2011.

[86] R. L. Espinola, T. Izuhara, M.-C. Tsai, R. M. Osgood, and H. Dötsch, "Magneto-optical nonreciprocal phase shift in garnet/silicon-on-insulator waveguides," *Optics Letters,* vol. 29, no. 9, pp. 941-943, 2004/05/01 2004.

[87] S. K. Ibrahim, S. Bhandare, D. Sandel, H. Zhang, and R. Noe, "Non-magnetic 30 dB integrated optical isolator in III/V material," *Electronics Letters,* vol. 40, no. 20, pp. 1293-1294, 2004.

[88] J. Hwang *et al.*, "Electro-tunable optical diode based on photonic bandgap liquid-crystal heterojunctions," *Nature Materials,* vol. 4, p. 383, 04/24/online 2005.

[89] S. Manipatruni, J. T. Robinson, and M. Lipson, "Optical Nonreciprocity in Optomechanical Structures," *Physical Review Letters,* vol. 102, no. 21, p. 213903, 05/29/ 2009.

[90] M. S. Kang, A. Butsch, and P. S. J. Russell, "Reconfigurable light-driven opto-acoustic isolators in photonic crystal fibre," *Nature Photonics,* Article vol. 5, p. 549, 08/14/online 2011.

[91] Z. Wu *et al.*, "Optical nonreciprocal transmission in an asymmetric silicon photonic crystal structure," *Applied Physics Letters,* vol. 107, no. 22, p. 221102, 2015.

[92] A. Mostafazadeh, "Pseudo-Hermiticity versus PT symmetry: The necessary condition for the reality of the spectrum of a non-Hermitian Hamiltonian," *Journal of Mathematical Physics,* vol. 43, no. 1, pp. 205-214, 2002.

[93] A. Guo *et al.*, "Observation of $\mathcal{P}\mathcal{T}$-Symmetry Breaking in Complex Optical Potentials," *Physical Review Letters,* vol. 103, no. 9, p. 093902, 08/27/ 2009.

[94] T. Amemiya, H. Shimizu, M. Yokoyama, P. N. Hai, M. Tanaka, and Y. Nakano, "Single mode operation of 1.5 μm TM-mode waveguide optical isolators based on the nonreciprocal-loss phenomenon," in *2007 Conference on Lasers and Electro-Optics (CLEO)*, 2007, pp. 1-2.

[95] Y. Shoji, M. Ito, Y. Shirato, and T. Mizumoto, "MZI optical isolator with Si-wire waveguides by surface-activated direct bonding," *Optics Express,* vol. 20, no. 16, pp. 18440-18448, 2012/07/30 2012.

[96] W. V. Parys *et al.*, "Transverse magnetic mode nonreciprocal propagation in an amplifying AlGaInAs/InP optical waveguide isolator," *Applied Physics Letters,* vol. 88, no. 7, p. 071115, 2006.

[97] Z. Wang and S. Fan, "Optical circulators in two-dimensional magneto-optical photonic crystals," *Optics Letters,* vol. 30, no. 15, pp. 1989-1991, 2005/08/01 2005.

[98] Z. Yu and S. Fan, "Complete optical isolation created by indirect interband photonic transitions," *Nature Photonics,* Corrigendum vol. 3, p. 303, 04/15/online 2009.

[99] S.-Y. Sung, X. Qi, and B. J. H. Stadler, "Integrating yttrium iron garnet onto nongarnet substrates with faster deposition rates and high reliability," *Applied Physics Letters,* vol. 87, no. 12, p. 121111, 2005.

[100] T. Boudiar, B. Payet-Gervy, M. F. Blanc-Mignon, J. J. Rousseau, M. Le Berre, and H. Joisten, *Magneto-Optical Properties of Yttrium Iron Garnet (YIG) Thin Films Elaborated by Radio Frequency Sputtering*. 2004, pp. 77-85.

[101] M. Krause, H. Renner, and E. Brinkmeyer, "Optical isolation in silicon waveguides based on nonreciprocal Raman amplification," *Electronics Letters*, vol. 44, no. 11, pp. 691-693Available: http://digital-library.theiet.org/content/journals/10.1049/el_20080791

[102] C. G. Poulton, R. Pant, A. Byrnes, S. Fan, M. J. Steel, and B. J. Eggleton, "Design for broadband on-chip isolator using stimulated Brillouin scattering in dispersion-engineered chalcogenide waveguides," *Optics Express,* vol. 20, no. 19, pp. 21235-21246, 2012/09/10 2012.

[103] H. Lira, Z. Yu, S. Fan, and M. Lipson, "Electrically Driven Nonreciprocity Induced by Interband Photonic Transition on a Silicon Chip," *Physical Review Letters,* vol. 109, no. 3, p. 033901, 07/16/ 2012.

[104] Z. Yu and S. Fan, "Complete optical isolation created by indirect interband photonic transitions," *Nature Photonics,* vol. 3, p. 91, 01/11/online 2009.

[105] I. C. Khoo, "Nonlinear optics of liquid crystalline materials," *Physics Reports,* vol. 471, no. 5, pp. 221-267, 2009/02/01/ 2009.

[106] K. Gallo, G. Assanto, K. R. Parameswaran, and M. M. Fejer, "All-optical diode in a periodically poled lithium niobate waveguide," *Applied Physics Letters,* vol. 79, no. 3, pp. 314-316, 2001.

[107] L. Fan *et al.*, "An All-Silicon Passive Optical Diode," *Science,* vol. 335, no. 6067, pp. 447-450, 2012.

[108] B. Peng *et al.*, "Parity–time-symmetric whispering-gallery microcavities," *Nature Physics,* Article vol. 10, p. 394, 04/06/online 2014.

[109] F. Abolmaali, N. I. Limberopoulos, A. M. Urbas, and V. N. Astratov, "Observation of the influence of the gain on parity-time-symmetric properties of photonic molecules with coupled whispering gallery modes," in *2015 National Aerospace and Electronics Conference (NAECON)*, 2015, pp. 106-109.

[110] K. D. Smith *et al.*, "High operating temperature mid-wavelength infrared HgCdTe photon trapping focal plane arrays," in *SPIE Defense, Security, and Sensing*, 2012, vol. 8353, p. 7: SPIE.

[111] S. Krishna, K. T. Posani, V. Tripathi, and S. Annamalai, "Quantum dot infrared sensors with photonic crystal cavity," in *2005 IEEE LEOS Annual Meeting Conference Proceedings*, 2005, pp. 909-910.

[112] S. Maimon and G. W. Wicks, "nBn detector, an infrared detector with reduced dark current and higher operating temperature," *Applied Physics Letters,* vol. 89, no. 15, p. 151109, 2006.

[113] A. I. D'Souza *et al.*, "MWIR InAs_{1-x}Sb_x nCBn detectors data and analysis," in *SPIE Defense, Security, and Sensing*, 2012, vol. 8353, p. 8: SPIE.

[114] A. M. White, "Infra red detectors," 1983.

[115] R. C. Hardie, D. R. Droege, A. J. Dapore, and M. E. Greiner, "Impact of detector-element active-area shape and fill factor on super-resolution," (in English), *Frontiers in Physics,* Original Research vol. 3, no. 31, 2015-May-18 2015.

[116] A. Rogalski, "Progress in focal plane array technologies," *Progress in Quantum Electronics,* vol. 36, no. 2, pp. 342-473, 2012/03/01/ 2012.

[117] Z. Zhao, M. Hui, M. Liu, L. Dong, X. Liu, and Y. Zhao, "Centroid shift analysis of microlens array detector in interference imaging system," *Optics Communications,* vol. 354, pp. 132-139, 2015/11/01/ 2015.

[118] "Microlens Arrays," ed: SUSS MicroOptics SA, Neuchatel, Catalogue 2007, http://www.amstechnologies.com/fileadmin/amsmedia/downloads/2067_SMO_catalog.pdf.

[119] M. Hasan and J. J. Simpson, "Photonic nanojet-enhanced nanometer-scale germanium photodiode," *Applied Optics,* vol. 52, no. 22, pp. 5420-5425, 2013/08/01 2013.

[120] K. W. Allen *et al.*, "Increasing sensitivity and angle-of-view of mid-wave infrared detectors by integration with dielectric microspheres," *Applied Physics Letters,* vol. 108, no. 24, p. 241108, 2016.

[121] S. M. Mansfield and G. S. Kino, "Solid immersion microscope," *Applied Physics Letters,* vol. 57, no. 24, pp. 2615-2616, 1990.

[122] B. D. Terris, H. J. Mamin, and D. Rugar, "Near-field optical data storage," *Applied Physics Letters,* vol. 68, no. 2, pp. 141-143, 1996.

[123] M. Baba, T. Sasaki, M. Yoshita, and H. Akiyama, "Aberrations and allowances for errors in a hemisphere solid immersion lens for

submicron-resolution photoluminescence microscopy," *Journal of Applied Physics,* vol. 85, no. 9, pp. 6923-6925, 1999.

[124] T. D. Milster, "Near-field optical data storage: avenues for improved performance," in *Photonics Taiwan*, 2000, vol. 4081, p. 9: SPIE.

[125] K. Karrai, X. Lorenz, and L. Novotny, "Enhanced reflectivity contrast in confocal solid immersion lens microscopy," *Applied Physics Letters,* vol. 77, no. 21, pp. 3459-3461, 2000.

[126] D. M. Tom *et al.*, "Super-Resolution by Combination of a Solid Immersion Lens and an Aperture," *Japanese Journal of Applied Physics,* vol. 40, no. 3S, p. 1778, 2001.

[127] S. Moehl, H. Zhao, B. D. Don, S. Wachter, and H. Kalt, "Solid immersion lens-enhanced nano-photoluminescence: Principle and applications," *Journal of Applied Physics,* vol. 93, no. 10, pp. 6265-6272, 2003.

[128] Y. Zhang, "Design of high-performance supersphere solid immersion lenses," *Applied Optics,* vol. 45, no. 19, pp. 4540-4546, 2006/07/01 2006.

[129] K. A. Serrels, E. Ramsay, R. J. Warburton, and D. T. Reid, "Nanoscale optical microscopy in the vectorial focusing regime," *Nature Photonics,* vol. 2, p. 311, 03/09/online 2008.

[130] A. K. Bates *et al.*, "Review of technology for 157-nm lithography," *IBM Journal of Research and Development,* vol. 45, no. 5, pp. 605-614, 2001.

[131] I. Lang, *The behaviour of the plasma membrane during plasmolysis: A study by UV microscopy*. 2000, pp. 188-98.

[132] J. A. N. Scott, A. R. Procter, B. J. Fergus, and D. A. I. Goring, "The application of ultraviolet microscopy to the distribution of lignin in wood description and validity of the technique," *Wood Science and Technology,* journal article vol. 3, no. 1, pp. 73-92, March 01 1969.

[133] X. Hao *et al.*, "From microscopy to nanoscopy via visible light," *Light: Science &Amp; Applications,* Review vol. 2, p. e108, 10/25/online 2013.

[134] Rayleigh, "XXXI. Investigations in optics, with special reference to the spectroscope," *The London, Edinburgh, and Dublin Philosophical Magazine and Journal of Science,* vol. 8, no. 49, pp. 261-274, 1879/10/01 1879.

[135] C. M. Sparrow, "On spectroscopic resolving power," *Astrophysical Journal,* vol. 29(3), 478-484 1916.

[136] W. V. Houston, "A compound interferometer for fine structure work," *Physical Review,* vol. 29(3), 478-484 1927.

[137] B. R. Masters, "Ernst Abbe and the Foundation of Scientific Microscopes," *Optics and Photonics News,* vol. 18, no. 2, pp. 18-23, 2007/02/01 2007.

[138] A. Darafsheh, *Optical super-resolution and periodical focusing effects by dielectric microspheres*. 2013.

[139] J. W. Goodman, *Statistical Optics*. Wiley, New York, NY, 1985.

[140] N. E. Dickenson, K. P. Armendariz, H. A. Huckabay, P. W. Livanec, and R. C. Dunn, "Near-field scanning optical microscopy: a tool for nanometric exploration of biological membranes," *Analytical and Bioanalytical Chemistry,* journal article vol. 396, no. 1, pp. 31-43, January 01 2010.

[141] S. J. Bukofsky and R. D. Grober, "Video rate near-field scanning optical microscopy," *Applied Physics Letters,* vol. 71, no. 19, pp. 2749-2751, 1997.

[142] V. I. I. DR. MIODRAG MICIC. (Feb 2004). *Near-Field Scanning Optical Microscopy and Spectroscopy Advance*.

[143] C. M. Soukoulis, S. Linden, and M. Wegener, "Negative Refractive Index at Optical Wavelengths," *Science,* vol. 315, no. 5808, pp. 47-49, 2007.

[144] R. A. Shelby, D. R. Smith, and S. Schultz, "Experimental Verification of a Negative Index of Refraction," *Science,* vol. 292, no. 5514, pp. 77-79, 2001.

[145] J. B. Pendry, "Negative Refraction Makes a Perfect Lens," *Physical Review Letters,* vol. 85, no. 18, pp. 3966-3969, 10/30/ 2000.

[146] P. V. Parimi, W. T. Lu, P. Vodo, and S. Sridhar, "Imaging by flat lens using negative refraction," *Nature,* vol. 426, p. 404, 11/27/online 2003.

[147] D. O. S. Melville and R. J. Blaikie, "Super-resolution imaging through a planar silver layer," *Optics Express,* vol. 13, no. 6, pp. 2127-2134, 2005/03/21 2005.

[148] N. Fang, H. Lee, C. Sun, and X. Zhang, "Sub–Diffraction-Limited Optical Imaging with a Silver Superlens," *Science,* vol. 308, no. 5721, pp. 534-537, 2005.

[149] A. Salandrino and N. Engheta, "Far-field subdiffraction optical microscopy using metamaterial crystals: Theory and simulations," *Physical Review B,* vol. 74, no. 7, p. 075103, 08/15/ 2006.

[150] Z. Jacob, L. V. Alekseyev, and E. Narimanov, "Optical Hyperlens: Far-field imaging beyond the diffraction limit," *Optics Express,* vol. 14, no. 18, pp. 8247-8256, 2006/09/04 2006.

[151] S. Kawata, Y. Inouye, and P. Verma, "Plasmonics for near-field nano-imaging and superlensing," *Nature Photonics,* Review Article vol. 3, p. 388, 07/01/online 2009.

[152] B. D. Terris, H. J. Mamin, D. Rugar, W. R. Studenmund, and G. S. Kino, "Near-field optical data storage using a solid immersion lens," *Applied Physics Letters,* vol. 65, no. 4, pp. 388-390, 1994.

[153] J. Y. Lee *et al.*, "Near-field focusing and magnification through self-assembled nanoscale spherical lenses," *Nature,* vol. 460, p. 498, 07/23/online 2009.

[154] Z. Wang *et al.*, "Optical virtual imaging at 50 nm lateral resolution with a white-light nanoscope," *Nature Communications,* Article vol. 2, p. 218, 03/01/online 2011.

[155] A. K. W. *et al.*, "Super-resolution microscopy by movable thin-films with embedded microspheres: Resolution analysis," *Annalen der Physik,* vol. 527, no. 7-8, pp. 513-522, 2015.

[156] V. N. Astratov *et al.*, "Optical nanoscopy with contact microlenses overcomes the diffraction limit," *SPIE Newsroom,* 2016.

[157] K. W. Allen *et al.*, "Super-resolution microscopy by movable thin-films with embedded microspheres: Resolution analysis," *Ann. Phys. (Berlin),* vol. 527, no. 7-8, pp. 513-522, 2015.

[158] K. W. Allen *et al.*, "Overcoming the diffraction limit of imaging nanoplasmonic arrays by microspheres and microfibers," *Optics Express,* vol. 23, no. 19, pp. 24484-24496, 2015.

[159] A. Darafsheh, N. I. Limberopoulos, J. S. Derov, D. E. Walker Jr, and V. N. Astratov, "Advantages of microsphere-assisted super-resolution imaging technique over solid immersion lens and confocal microscopies," *Applied Physics Letters,* vol. 104, no. 6, p. 061117, 2014.

[160] V. Westphal, S. O. Rizzoli, M. A. Lauterbach, D. Kamin, R. Jahn, and S. W. Hell, "Video-Rate Far-Field Optical Nanoscopy Dissects Synaptic Vesicle Movement," *Science,* vol. 320, no. 5873, pp. 246-249, 2008.

[161] S. W. Hell and J. Wichmann, "Breaking the diffraction resolution limit by stimulated emission: stimulated-emission-depletion fluorescence microscopy," *Optics Letters,* vol. 19, no. 11, pp. 780-782, 1994/06/01 1994.

[162] T. A. Klar and S. W. Hell, "Subdiffraction resolution in far-field fluorescence microscopy," *Optics Letters,* vol. 24, no. 14, pp. 954-956, 1999/07/15 1999.

[163] S. W. Hell and M. Kroug, "Ground-state-depletion fluorscence microscopy: A concept for breaking the diffraction resolution limit," *Applied Physics B,* journal article vol. 60, no. 5, pp. 495-497, May 01 1995.

[164] S. Bretschneider, C. Eggeling, and S. W. Hell, "Breaking the Diffraction Barrier in Fluorescence Microscopy by Optical Shelving," *Physical Review Letters,* vol. 98, no. 21, p. 218103, 05/24/ 2007.

[165] G. M. G. L., "Surpassing the lateral resolution limit by a factor of two using structured illumination microscopy," *Journal of Microscopy,* vol. 198, no. 2, pp. 82-87, 2000.

[166] *Education in Microscopy and Digital Imaging (Superresolution Structured Illumination Microscopy)*. Available: http://zeiss-campus.magnet.fsu.edu/tutorials/superresolution/hrsim/indexflash.html

[167] F. Wei *et al.*, "Wide Field Super-Resolution Surface Imaging through Plasmonic Structured Illumination Microscopy," *Nano Letters,* vol. 14, no. 8, pp. 4634-4639, 2014/08/13 2014.

[168] J. L. Ponsetto *et al.*, "Experimental Demonstration of Localized Plasmonic Structured Illumination Microscopy," *ACS Nano,* vol. 11, no. 6, pp. 5344-5350, 2017/06/27 2017.

[169] A. Bezryadina *et al.*, *Localized plasmonic structured illumination microscopy with optically trapped microlens*. 2017.

[170] K. J. Czymmek and T. Dahms, *Future Directions in Advanced Mycological Microscopy*. 2015, pp. 143-162.

[171] L. V. Brown, H. Sobhani, J. B. Lassiter, P. Nordlander, and N. J. Halas, "Heterodimers: Plasmonic Properties of Mismatched Nanoparticle Pairs," *ACS Nano,* vol. 4, no. 2, pp. 819-832, 2010/02/23 2010.

[172] C. Sönnichsen, B. M. Reinhard, J. Liphardt, and A. P. Alivisatos, "A molecular ruler based on plasmon coupling of single gold and silver nanoparticles," *Nature Biotechnology,* vol. 23, p. 741, 05/22/online 2005.

[173] P. Nordlander, C. Oubre, E. Prodan, K. Li, and M. I. Stockman, "Plasmon Hybridization in Nanoparticle Dimers," *Nano Letters,* vol. 4, no. 5, pp. 899-903, 2004/05/01 2004.

[174] D. W. Brandl, N. A. Mirin, and P. Nordlander, "Plasmon Modes of Nanosphere Trimers and Quadrumers," *The Journal of Physical Chemistry B,* vol. 110, no. 25, pp. 12302-12310, 2006/06/01 2006.

[175] Y. A. Urzhumov, G. Shvets, J. Fan, F. Capasso, D. Brandl, and P. Nordlander, "Plasmonic nanoclusters: a path towards negative-index metafluids," *Optics Express,* vol. 15, no. 21, pp. 14129-14145, 2007/10/17 2007.

[176] M. Hentschel, M. Saliba, R. Vogelgesang, H. Giessen, A. P. Alivisatos, and N. Liu, "Transition from Isolated to Collective Modes in Plasmonic Oligomers," *Nano Letters,* vol. 10, no. 7, pp. 2721-2726, 2010/07/14 2010.

[177] I. Zorić, M. Zäch, B. Kasemo, and C. Langhammer, "Gold, Platinum, and Aluminum Nanodisk Plasmons: Material Independence, Subradiance, and Damping Mechanisms," *ACS Nano,* vol. 5, no. 4, pp. 2535-2546, 2011/04/26 2011.

[178] M. I. Stockman, "Dark-hot resonances," *Nature,* vol. 467, p. 541, 09/29/online 2010.

[179] V. N. Astratov, J. P. Franchak, and S. P. Ashili, "Optical coupling and transport phenomena in chains of spherical dielectric microresonators with size disorder," *Applied Physics Letters,* vol. 85, no. 23, pp. 5508-5510, 2004.

[180] A. V. Kanaev, V. N. Astratov, and W. Cai, "Optical coupling at a distance between detuned spherical cavities," *Applied Physics Letters,* vol. 88, no. 11, p. 111111, 2006.

[181] V. N. Astratov and S. P. Ashili, "Percolation of light through whispering gallery modes in 3D lattices of coupled microspheres," *Optics Express,* vol. 15, no. 25, pp. 17351-17361, 2007/12/10 2007.

[182] B. M. Möller, U. Woggon, and M. V. Artemyev, "Bloch modes and disorder phenomena in coupled resonator chains," *Physical Review B,* vol. 75, no. 24, p. 245327, 06/26/ 2007.

[183] C.-S. Deng, H. Xu, and L. Deych, "Effect of size disorder on the optical transport in chains of coupled microspherical resonators," *Optics Express,* vol. 19, no. 7, pp. 6923-6937, 2011/03/28 2011.

[184] J. K. S. Poon, J. Scheuer, Y. Xu, and A. Yariv, "Designing coupled-resonator optical waveguide delay lines," *Journal of the Optical Society of America B,* vol. 21, no. 9, pp. 1665-1673, 2004/09/01 2004.

[185] A. Nakagawa, S. Ishii, and T. Baba, "Photonic molecule laser composed of GaInAsP microdisks," *Applied Physics Letters,* vol. 86, no. 4, p. 041112, 2005.

[186] F. Xia, L. Sekaric, and Y. Vlasov, "Ultracompact optical buffers on a silicon chip," *Nature Photonics,* Article vol. 1, p. 65, 12/21/online 2006.

[187] M. R. Foreman, J. D. Swaim, and F. Vollmer, "Whispering gallery mode sensors," *Advances in Optics and Photonics,* vol. 7, no. 2, pp. 168-240, 2015/06/30 2015.

[188] F. Vollmer and L. Yang, "Review Label-free detection with high-Q microcavities: a review of biosensing mechanisms for integrated devices," in *Nanophotonics* vol. 1, ed, 2012, p. 267.

[189] A. Francois and M. Himmelhaus, "Optical biosensor based on whispering gallery mode excitations in clusters of microparticles," *Applied Physics Letters,* vol. 92, no. 14, p. 141107, 2008.

[190] D. V. Guzatov and U. Woggon, "Coupled microsphere clusters for detecting molecule's dipole moment orientation," *Applied Physics Letters,* vol. 94, no. 24, p. 241104, 2009.

[191] S. V. Boriskina and L. Dal Negro, "Self-referenced photonic molecule bio(chemical)sensor," *Optics Letters,* vol. 35, no. 14, pp. 2496-2498, 2010/07/15 2010.

[192] Ş. K. Özdemir *et al.*, "Highly sensitive detection of nanoparticles with a self-referenced and self-heterodyned whispering-gallery Raman microlaser," *Proceedings of the National Academy of Sciences,* vol. 111, no. 37, pp. E3836-E3844, 2014.

[193] W. Ahn, S. V. Boriskina, Y. Hong, and B. M. Reinhard, "Photonic–Plasmonic Mode Coupling in On-Chip Integrated Optoplasmonic Molecules," *ACS Nano,* vol. 6, no. 1, pp. 951-960, 2012/01/24 2012.

[194] S. V. Boriskina and B. M. Reinhard, "Spectrally and spatially configurable superlenses for optoplasmonic nanocircuits," *Proceedings of the National Academy of Sciences,* vol. 108, no. 8, pp. 3147-3151, 2011.

[195] J. Zhu *et al.*, "On-chip single nanoparticle detection and sizing by mode splitting in an ultrahigh-Q microresonator," *Nature Photonics,* vol. 4, p. 46, 12/13/online 2009.

[196] T. Mukaiyama, K. Takeda, H. Miyazaki, Y. Jimba, and M. Kuwata-Gonokami, "Tight-Binding Photonic Molecule Modes of Resonant Bispheres," *Physical Review Letters,* vol. 82, no. 23, pp. 4623-4626, 06/07/ 1999.

[197] Y. P. Rakovich *et al.*, "Fine structure of coupled optical modes in photonic molecules," *Physical Review A,* vol. 70, no. 5, p. 051801, 11/08/ 2004.

[198] J. Ng and C. T. Chan, "Size-selective optical forces for microspheres using evanescent wave excitation of whispering gallery modes," *Applied Physics Letters,* vol. 92, no. 25, p. 251109, 2008.

[199] J. J. Xiao, J. Ng, Z. F. Lin, and C. T. Chan, "Whispering gallery mode enhanced optical force with resonant tunneling excitation in the Kretschmann geometry," *Applied Physics Letters,* vol. 94, no. 1, p. 011102, 2009.

[200] E. Almaas and I. Brevik, "Possible sorting mechanism for microparticles in an evanescent field," *Physical Review A,* vol. 87, no. 6, p. 063826, 06/17/ 2013.

[201] V. N. Astratov, "Methods and devices for optical sorting of microspheres based on their resonant optical properties, U.S. patent US20140069850 A1 http://www.google.com/patents/US20140069850," 2011. Available: http://www.google.com/patents/US20140069850.

[202] Y. Li, O. V. Svitelskiy, A. V. Maslov, D. Carnegie, E. Rafailov, and V. N. Astratov, "Giant resonant light forces in microspherical photonics," *Light Sci Appl,* Original Article vol. 2, p. e64, 04/26/online 2013.

[203] V. N. Astratov *et al.*, "Microspherical Photonics: Ultra-High Resonant Propulsion Forces," *Optics and Photonics News,* vol. 24, no. 12, pp. 40-40, 2013/12/01 2013.

[204] Y. Li, A. V. Maslov, N. I. Limberopoulos, A. M. Urbas, and V. N. Astratov, "Spectrally resolved resonant propulsion of dielectric microspheres," *Laser & Photonics Reviews,* vol. 9, no. 2, pp. 263-273, 2015.

[205] Y. Li, "Microspherical photonics: Giant resonant light forces, spectrally resolved optical manipulation, and coupled modes of microcavity arrays", Ph.D. dissertation (University of North Carolina at Charlotte), https://arxiv.org/abs/1509.01306.," 2015.

[206] A. V. Maslov, "Optomechanical properties of a particle-waveguide system," *Physical Review A,* vol. 90, no. 3, p. 033825, 09/17/ 2014.

[207] A. V. Maslov and V. N. Astratov, "Microspherical photonics: Sorting resonant photonic atoms by using light," *Applied Physics Letters,* vol. 105, no. 12, p. 121113, 2014.

[208] A. V. Maslov and V. Astratov, *Microspherical photonics: Sorting resonant photonic atoms by using light.* 2014, p. 121113.

[209] I. Mahariq, V. N. Astratov, and H. Kurt, "Persistence of photonic nanojet formation under the deformation of circular boundary," *Journal of the Optical Society of America B,* vol. 33, no. 4, pp. 535-542, 2016/04/01 2016.

[210] K. W. Allen *et al.*, "Microsphere-chain waveguides: Focusing and transport properties," *Applied Physics Letters,* vol. 105, no. 2, p. 021112, 2014.

[211] A. Darafsheh, N. Mojaverian, N. I. Limberopoulos, K. W. Allen, A. Lupu, and V. N. Astratov, "Formation of polarized beams in chains of dielectric spheres and cylinders," *Optics letters,* vol. 38, no. 20, pp. 4208-4211, 2013.

[212] A. Darafsheh and V. N. Astratov, "Periodically focused modes in chains of dielectric spheres," *Applied Physics Letters,* vol. 100, no. 6, pp. 061123-061123-4, 02/10
12/25/received
01/24/accepted 2012.

[213] O. Svitelskiy *et al.*, "Fiber coupling to BaTiO3 glass microspheres in an aqueous environment," *Optics Letters,* vol. 36, no. 15, pp. 2862-2864, 2011/08/01 2011.

[214] B. D. Jones *et al.*, "Splitting and lasing of whispering gallery modes in quantum dot micropillars," *Optics Express,* vol. 18, no. 21, pp. 22578-22592, 2010/10/11 2010.

[215] S. Yang and V. N. Astratov, "Photonic nanojet-induced modes in chains of size-disordered microspheres with an attenuation of only 0.08dB per sphere," *Applied Physics Letters,* vol. 92, no. 26, p. 261111, 2008.

[216] K. R. Hiremath and V. N. Astratov, "Perturbations of whispering gallery modes by nanoparticles embedded in microcavities," *Optics Express,* vol. 16, no. 8, pp. 5421-5426, 2008/04/14 2008.

[217] A. M. Kapitonov and V. N. Astratov, "Observation of nanojet-induced modes with small propagation losses in chains of coupled spherical cavities," *Optics Letters,* vol. 32, no. 4, pp. 409-411, 2007/02/15 2007.

[218] S. P. Ashili, V. N. Astratov, and E. C. H. Sykes, "The effects of inter-cavity separation on optical coupling in dielectric bispheres," *Optics Express,* vol. 14, no. 20, pp. 9460-9466, 2006/10/02 2006.

[219] A. V. Kanaev, V. N. Astratov, and W. Cai, "Optical coupling at a distance between detuned spherical cavities," *Applied Physics Letters,* vol. 88(11), 111111 2006.

[220] S. Deng, W. Cai, and V. N. Astratov, "Numerical study of light propagation via whispering gallery modes in microcylinder coupled resonator optical waveguides," *Optics Express,* vol. 12, no. 26, pp. 6468-6480, 2004/12/27 2004.

[221] F. Abolmaali *et al.*, *Spectral signatures of photonic molecules with hybridized whispering gallery modes*. 2017, pp. 1-4.

[222] A. V. Maslov, M. I. Bakunov, and V. N. Astratov, "Dynamics of dielectric microparticles in optical fields: Taking advantage of intrinsic particle resonances and hybrid particle-waveguide resonances," in *2015 17th International Conference on Transparent Optical Networks (ICTON)*, 2015, pp. 1-4.

[223] Y. Li, F. Abolmaali, N. I Limberopoulos, A. M Urbas, and V. Astratov, *Coupling properties and sensing applications of photonic molecules*. 2015.

[224] A. V. Maslov, M. I. Bakunov, Y. Li, and V. N. Astratov, "Resonant optical forces associated with the excitation of whispering gallery modes in microparticles," in *2014 16th International Conference on Transparent Optical Networks (ICTON)*, 2014, pp. 1-4.

[225] Y. Li, A. V. Maslov, N. I. Limberopoulos, and V. Astratov, *Demonstration of whispering-gallery-mode resonant enhancement of optical forces*. 2015.

[226] Y. Li, A. V. Maslov, and V. Astratov, *Spectral control and temporal properties of resonant optical propulsion of dielectric microspheres in evanescent fiber couplers*. 2014.

[227] A. V. Maslov, M. I. Bakunov, Y. Li, and V. N. Astratov, "Resonant Optical forces associated with whispering gallery modes in microparticles," in *2014 IEEE Photonics Conference*, 2014, pp. 122-123.

[228] Y. Li, A. V. Maslov, A. Jofre, and V. Astratov, *Tuning the optical forces on- and off-resonance in microspherical photonics*. 2013, pp. 1-4.

[229] Y. Li, O. V. Svitelskiy, A. V. Maslov, D. Carnegie, E. Rafailov, and V. N. Astratov, "Resonant optical propelling of microspheres: A path to selection of almost identical photonic atoms," in *2012 14th International Conference on Transparent Optical Networks (ICTON)*, 2012, pp. 1-4.

[230] Y. Li, O. Svitelskiy, D. Carnegie, E. Rafailov, and V. N. Astratov, "Evanescent light coupling and optical propelling of microspheres in water immersed fiber couplers," in *SPIE LASE*, 2012, vol. 8236, p. 8: SPIE.

[231] A. Darafsheh and V. Astratov, *Chains of variable size spheres for focusing of multimodal beams in photonics applications*. 2011, p. Article# We.P.2.

[232] A. Darafsheh, A. Lupu, S. Adam Burand, T. C. Hutchens, N. M. Fried, and V. Astratov, *Photonic Nanojet-Induced Modes: Fundamentals and Applications*. 2012, p. 22.

[233] O. Svitelskiy, Y. Li, M. Sumetsky, D. Carnegie, E. U. Rafailov, and V. Astratov, *A microfluidic platform integrated with tapered optical fiber*

for studying resonant properties of compact high index microspheres. 2011, pp. 1-4.

[234] O. Svitelskiy *et al.*, *Characterization of high index microsphere resonators in fiber-integrated microfluidic platforms*. 2011, p. 791314.

[235] V. Astratov, *Fundamentals and applications of microsphere resonator circuits*. 2009, pp. 1-4.

[236] Y. Seungmoo and V. N. Astratov, "Spectroscopy of coherently coupled whispering gallery modes in supermonodispersive bispheres," in *2009 11th International Conference on Transparent Optical Networks*, 2009, pp. 1-4.

[237] K. R. Hiremath and V. N. Astratov, "Splitting of whispering gallery modes by nanoparticles embedded in high Q microcavities," in *2009 11th International Conference on Transparent Optical Networks*, 2009, pp. 1-4.

[238] B. Jones *et al.*, "Whispering Gallery Modes in Quantum Dot Micropillar Cavities," in *Conference on Lasers and Electro-Optics/Quantum Electronics and Laser Science Conference and Photonic Applications Systems Technologies*, San Jose, California, 2008, p. CTuW7: Optical Society of America.

[239] V. N. Astratov, S. P. Ashili, and S. Yang, "Optical Transport Phenomena in Coupled Spherical Cavities," in *2007 9th International Conference on Transparent Optical Networks*, 2007, vol. 3, pp. 65-70.

[240] V. N. Astratov *et al.*, "High-Quality-Factor WG Modes in Semiconductor Microcavity Pillars with Circular and Elliptical Cross Section," in *2007 9th International Conference on Transparent Optical Networks*, 2007, vol. 4, pp. 170-172.

[241] V. N. Astratov and S. P. Ashili, "Percolation of light in 3D lattices of coupled microspheres," in *2007 Quantum Electronics and Laser Science Conference*, 2007, pp. 1-2.

[242] V. N. Astratov *et al.*, "Observation of Whispering Gallery Resonances in Circular and Elliptical Semiconductor Pillar Microcavities," in *Frontiers in Optics*, Rochester, New York, 2006, p. FThF7: Optical Society of America.

[243] V. N. Astratov, S. P. Ashili, A. M. Kapitonov, and A. V. Kanaev, "Integrated Circuits of Coupled Mircospheres for Optoelectronics Applications," in *2006 International Conference on Transparent Optical Networks*, 2006, vol. 1, pp. 77-81.

[244] V. N. Astratov, A. V. Kanaev, S. P. Ashili, J. P. Franchak, and W. Cai, "Optical Delay Lines Formed by Circuits of Spherical Cavities with Coupled Whispering Gallery Modes," in *Adaptive Optics: Analysis and Methods/Computational Optical Sensing and Imaging/Information Photonics/Signal Recovery and Synthesis Topical Meetings on CD-ROM*, Charlotte, North Carolina, 2005, p. IThD2: Optical Society of America.

[245] E. C. H. Sykes, S. P. Ashili, A. V. Kanaev, and V. N. Astratov, "Encapsulated microsphere arrays for applications in photonic circuits," in *2005 OSA Topical Meeting on Information Photonics (IP)*, 2005, pp. 1-3.

[246] V. N. Astratov, S. P. Ashili, J. P. Franchak, A. V. Kanaev, and W. Cai, "Optical coupling between spherical dielectric atoms," in *2005 Quantum Electronics and Laser Science Conference*, 2005, vol. 1, pp. 413-414 Vol. 1.

[247] V. N. Astratov, J. P. Franchak, S. F. Ashili, W. Cai, and M. A. Hasan, "Resonant optical circuits based on coupling between whispering gallery modes in dielectric microresonators," in *InternationalQuantum Electronics Conference, 2004. (IQEC).* 2004, pp. 784-785.

[248] S. V. Boriskina, "Spectral engineering of bends and branches in microdisk coupled-resonator optical waveguides," *Optics Express,* vol. 15, no. 25, pp. 17371-17379, 2007/12/10 2007.

[249] S. Longhi, "Quantum-optical analogies using photonic structures," *Laser & Photonics Reviews,* vol. 3, no. 3, pp. 243-261, 2009.

[250] B. Peng *et al.*, "Parity-time-symmetric whispering-gallery microcavities," *Nat Phys,* Article vol. 10, no. 5, pp. 394-398, 05//print 2014.

[251] Y. Li *et al.*, "Whispering gallery mode hybridization in photonic molecules," *Laser & Photonics Reviews,* vol. 11, no. 2, p. 1600278, 2017.

[252] M. Gerlach, Y. P. Rakovich, and J. F. Donegan, "Radiation-pressure-induced mode splitting in a spherical microcavity with an elastic shell," *Optics Express,* vol. 15, no. 6, pp. 3597-3606, 2007/03/19 2007.

[253] V. N. Astratov *et al.*, "Whispering gallery resonances in semiconductor micropillars," *Applied Physics Letters,* vol. 91, no. 7, p. 071115, 2007.

[254] S. C. Hagness, D. Rafizadeh, S. T. Ho, and A. Taflove, "FDTD microcavity simulations: design and experimental realization of waveguide-coupled single-mode ring and whispering-gallery-mode disk resonators," *Journal of Lightwave Technology,* vol. 15, no. 11, pp. 2154-2165, 1997.

[255] D. T. Nguyen and R. A. Norwood, "Label-free, single-object sensing with a microring resonator: FDTD simulation," *Optics Express,* vol. 21, no. 1, pp. 49-59, 2013/01/14 2013.

[256] Y. Li, K. W. Allen, F. Abolmaali, A. V. Maslov, and V. N. Astratov, "Spectral finger-prints of photonic molecules," in *2014 16th International Conference on Transparent Optical Networks (ICTON)*, 2014, pp. 1-4.

[257] F. Abolmaali *et al.*, "Photonic molecules and sensors based on coupling between whispering gallery modes in microspheres," in *2017 IEEE National Aerospace and Electronics Conference (NAECON)*, 2017, pp. 205-208.

[258] F. Abolmaali *et al.*, "Identification of whispering gallery modes in a fiber based sensor platform," in *2017 IEEE National Aerospace and Electronics Conference (NAECON)*, 2017, pp. 284-287.

[259] Y. Li, F. Abolmaali, N. I. Limberopoulos, A. M. Urbas, and V. N. Astratov, "Coupling properties and sensing applications of photonic molecules," in *2015 National Aerospace and Electronics Conference (NAECON)*, 2015, pp. 102-105.

[260] E. F. Franchimon, K. R. Hiremath, R. Stoffer, and M. Hammer, "Interaction of whispering gallery modes in integrated optical microring or microdisk circuits: hybrid coupled mode theory model," *Journal of the Optical Society of America B,* vol. 30, no. 4, pp. 1048-1057, 2013/04/01 2013.

[261] S. V. Boriskina, "Theoretical prediction of a dramatic Q-factor enhancement and degeneracy removal of whispering gallery modes in symmetrical photonic molecules," *Optics Letters,* vol. 31, no. 3, pp. 338-340, 2006/02/01 2006.

[262] Y. P. Rakovich and J. F. Donegan, "Photonic atoms and molecules," *Laser & Photonics Reviews,* vol. 4, no. 2, pp. 179-191, 2010.

[263] F. A. Y. Li, K. W. Allen, N. I. Limberopoulos, A. Urbas, Y. Rakovich, A. V. Maslov, and V. N. Astratov, "Whispering gallery mode hybridization in photonic molecules," *Laser & Photonics Revews,* vol. 10, 2017.

[264] R. G. a. N. R. Wallach, *Representations and Invariants of the Classical Groups*. Cambridge University Press, Cambridge, 1998.

[265] S. M. Spillane, T. J. Kippenberg, O. J. Painter, and K. J. Vahala, "Ideality in a Fiber-Taper-Coupled Microresonator System for Application to Cavity Quantum Electrodynamics," *Physical Review Letters,* vol. 91, no. 4, p. 043902, 07/22/ 2003.

[266] J. C. Knight, G. Cheung, F. Jacques, and T. A. Birks, "Phase-matched excitation of whispering-gallery-mode resonances by a fiber taper," *Optics Letters,* vol. 22, no. 15, pp. 1129-1131, 1997/08/01 1997.

[267] V. S. Ilchenko, M. L. Gorodetsky, and S. P. Vyatchanin, "Coupling and tunability of optical whispering-gallery modes: a basis for coordinate meter," *Optics Communications,* vol. 107, no. 1, pp. 41-48, 1994/04/01/ 1994.

[268] D. S. Weiss, V. Sandoghdar, J. Hare, V. Lefèvre-Seguin, J. M. Raimond, and S. Haroche, "Splitting of high-Q Mie modes induced by light backscattering in silica microspheres," *Optics Letters,* vol. 20, no. 18, pp. 1835-1837, 1995/09/15 1995.

[269] B. E. Little and S. T. Chu, "Estimating surface-roughness loss and output coupling in microdisk resonators," *Optics Letters,* vol. 21, no. 17, pp. 1390-1392, 1996/09/01 1996.

[270] T. J. Kippenberg, S. M. Spillane, and K. J. Vahala, "Modal coupling in traveling-wave resonators," *Optics Letters,* vol. 27, no. 19, pp. 1669-1671, 2002/10/01 2002.

[271] M. L. Gorodetsky, A. D. Pryamikov, and V. S. Ilchenko, "Rayleigh scattering in high-Q microspheres," *Journal of the Optical Society of America B,* vol. 17, no. 6, pp. 1051-1057, 2000/06/01 2000.

[272] C. Manolatou, M. J. Khan, S. Fan, P. R. Villeneuve, H. A. Haus, and J. D. Joannopoulos, "Coupling of modes analysis of resonant channel add-drop filters," *IEEE Journal of Quantum Electronics,* vol. 35, no. 9, pp. 1322-1331, 1999.

[273] M. Lohmeyer, "Mode expansion modeling of rectangular integrated optical microresonators," *Optical and Quantum Electronics,* journal article vol. 34, no. 5, pp. 541-557, May 01 2002.

[274] M. Hammer, "Resonant coupling of dielectric optical waveguides via rectangular microcavities: the coupled guided mode perspective," *Optics Communications,* vol. 214, no. 1, pp. 155-170, 2002/12/15/ 2002.

[275] A. Maznev, A. Every, and O. Wright, "Reciprocity in reflection and transmission: What is a 'phonon diode'?," *Wave Motion,* vol. 50, no. 4, pp. 776-784, 2013.

[276] J. Tan, M. Lu, A. Stein, and W. Jiang, "High-purity transmission of a slow light odd mode in a photonic crystal waveguide," *Optics Letters,* vol. 37, no. 15, pp. 3189-3191, 2012/08/01 2012.

[277] H. A. Haus, *Waves and fields in optoelectronics*. Englewood Cliffs, NJ: Prentice-Hall, 1984.

[278] M. J. Lockyear, A. P. Hibbins, K. R. White, and J. R. Sambles, "One-way diffraction grating," *Physical Review E,* vol. 74, no. 5, p. 056611, 2006.

[279] A. E. Serebryannikov and E. Ozbay, "Isolation and one-way effects in diffraction on dielectric gratings with plasmonic inserts," *Optics Express,* vol. 17, no. 1, pp. 278-292, 2009/01/05 2009.

[280] A. Armitage *et al.*, "Polariton-induced optical asymmetry in semiconductor microcavities," *Physical Review B,* vol. 58, no. 23, pp. 15367-15370, 12/15/ 1998.

[281] W. Van Parys *et al.*, "Transverse magnetic mode nonreciprocal propagation in an amplifying AlGaInAs/InP optical waveguide isolator," *Applied Physics Letters,* vol. 88, no. 7, p. 071115, 2006.

[282] Z. Wang, Y. Chong, J. D. Joannopoulos, and M. Soljacic, "Observation of unidirectional backscattering-immune topological electromagnetic states," *Nature,* 10.1038/nature08293 vol. 461, no. 7265, pp. 772-775, 10/08/print 2009.

[283] M. D. Tocci, M. J. Bloemer, M. Scalora, J. P. Dowling, and C. M. Bowden, "Thin-film nonlinear optical diode," *Applied Physics Letters,* vol. 66, no. 18, pp. 2324-2326, 1995.

[284] C. E. Ruter, K. G. Makris, R. El-Ganainy, D. N. Christodoulides, M. Segev, and D. Kip, "Observation of parity-time symmetry in optics," *Nat Phys,* 10.1038/nphys1515 vol. 6, no. 3, pp. 192-195, 03//print 2010.

[285] L. Feng *et al.*, "Experimental demonstration of a unidirectional reflectionless parity-time metamaterial at optical frequencies," *Nat Mater,* 10.1038/nmat3495 vol. 12, no. 2, pp. 108-113, 02//print 2013.

[286] F. Abolmaali, N. I. Limberopoulos, A. M. Urbas, A. V. Maslov, and V. N. Astratov, "Resonant routing of optical pulses in coupled-cavity structures," 2017, vol. 10106, pp. 101061J-101061J-7.

[287] V. N. Astratov *et al.*, "Label-free nanoscopy with contact microlenses: Super-resolution mechanisms and limitations," in *2016 18th International Conference on Transparent Optical Networks (ICTON)*, 2016, pp. 1-4.

[288] V. N. Astratov, "Fundamentals and applications of microsphere resonator circuits," in *Photonic Microresonator Research and Applications*, O. S. I. Chremmos, and N. Uzunoglu (eds.), Ed.: Springer Series in Optical Sciences, vol. 156, pp. 423-457, 2010.

[289] W. D. Heiss, "Repulsion of resonance states and exceptional points," *Physical Review E,* vol. 61, no. 1, pp. 929-932, 2000.

[290] S. V. Boriskina, "Coupling of whispering-gallery modes in size-mismatched microdisk photonic molecules," *Optics Letters,* vol. 32, no. 11, pp. 1557-1559, 2007.

[291] L.-W. Luo *et al.*, "WDM-compatible mode-division multiplexing on a silicon chip," *Nature Communications,* Article vol. 5, p. 3069, 01/15/online 2014.

[292] A. Y. Piggott, J. Lu, T. M. Babinec, K. G. Lagoudakis, J. Petykiewicz, and J. Vučković, "Inverse design and implementation of a wavelength demultiplexing grating coupler," *Scientific Reports,* Article vol. 4, p. 7210, 11/27/online 2014.

[293] A. V. Maslov, V. N. Astratov, and M. I. Bakunov, "Resonant propulsion of a microparticle by a surface wave," *Physical Review A,* vol. 87, no. 5, p. 053848, 05/30/ 2013.

[294] A. Armitage *et al.*, "Optically induced splitting of bright excitonic states in coupled quantum microcavities," *Physical Review B,* vol. 57, no. 23, pp. 14877-14881, 1998.

[295] Y. Li *et al.*, "Whispering gallery mode hybridization in photonic molecules," *Laser & Photonics Reviews,* vol. 11, no. 2, pp. 1600278-n/a, 2017, Art. no. 1600278.

[296] K. W. Allen *et al.*, "Photonic jets for strained-layer superlattice infrared photodetector enhancement," in *NAECON 2014 - IEEE National Aerospace and Electronics Conference*, 2014, pp. 32-33.

[297] T. C. Hutchens *et al.*, "Characterization of novel microsphere chain fiber optic tips for potential use in ophthalmic laser surgery," 2012, vol. 17, p. 8: SPIE.

[298] A. Darafsheh *et al.*, "Focusing capability of integrated chains of microspheres in the limit of geometrical optics," in *SPIE LASE*, 2011, vol. 7913, p. 7: SPIE.

[299] K. W. Allen, A. Darafsheh, and V. N. Astratov, "Photonic nanojet-induced modes: From physics to applications," in *2011 13th International Conference on Transparent Optical Networks*, 2011, pp. 1-4.

[300] A. Darafsheh, A. Lupu, S. A. Burand, T. C. Hutchens, N. M. Fried, and V. N. Astratov, "Photonic nanojet-induced modes: fundamentals and applications," in *SPIE OPTO*, 2012, vol. 8264, p. 8: SPIE.

[301] A. Darafsheh *et al.*, *Photonic nanojets for laser surgery*. 2010.

[302] A. Darafsheh, A. Fardad, N. M. Fried, A. N. Antoszyk, H. S. Ying, and V. N. Astratov, "Contact focusing multimodal microprobes for ultraprecise laser tissue surgery," *Optics Express,* vol. 19, no. 4, pp. 3440-3448, 2011/02/14 2011.

[303] S. L. Pyshkin and J. Ballato, "Optoelectronics: Advanced Materials and Devices," ed: InTech Rijeka, Croatia, 2013.

[304] P. B. Catrysse and T. Skauli, "Pixel scaling in infrared focal plane arrays," *Applied Optics,* vol. 52, no. 7, pp. C72-C77, 2013/03/01 2013.

[305] K. D. Smith *et al.*, "High operating temperature mid-wavelength infrared HgCdTe photon trapping focal plane arrays," 2012, vol. 8353, pp. 83532R-83532R-7.

[306] A. I. D'Souza *et al.*, "MWIR InAs<sub>1-x</sub>Sb<sub>x</sub> nCBn detectors data and analysis," 2012, vol. 8353, pp. 835333-835333-8.

[307] S.-B. Rim, P. B. Catrysse, R. Dinyari, K. Huang, and P. Peumans, "The optical advantages of curved focal plane arrays," *Optics Express,* vol. 16, no. 7, pp. 4965-4971, 2008/03/31 2008.

[308] S. C. Lee, S. Krishna, and S. R. J. Brueck, "Quantum dot infrared photodetector enhanced by surface plasma wave excitation," *Optics Express,* vol. 17, no. 25, pp. 23160-23168, 2009/12/07 2009.

[309] W. Wu, A. Bonakdar, and H. Mohseni, "Plasmonic enhanced quantum well infrared photodetector with high detectivity," *Appl. Phys. Lett,* vol. 96, no. 16, p. 161107, 2010.

[310] S. C. Lee, S. Krishna, and S. R. J. Brueck, "Light direction-dependent plasmonic enhancement in quantum dot infrared photodetectors," *Applied Physics Letters,* vol. 97, no. 2, p. 021112, 2010.

[311] G. Gu, J. Vaillancourt, P. Vasinajindakaw, and X. Lu, "Backside-configured surface plasmonic structure with over 40 times photocurrent enhancement," *Semiconductor Science and Technology,* vol. 28, no. 10, p. 105005, 2013.

[312] P. Vasinajindakaw, J. Vaillancourt, G. Gu, R. Liu, Y. Ling, and X. Lu, "A Fano-type interference enhanced quantum dot infrared photodetector," *Applied Physics Letters,* vol. 98, no. 21, p. 211111, 2011.

[313] D. M. Schaadt, B. Feng, and E. T. Yu, "Enhanced semiconductor optical absorption via surface plasmon excitation in metal nanoparticles," *Applied Physics Letters,* vol. 86, no. 6, p. 063106, 2005.

[314] L. Tang *et al.*, "Nanometre-scale germanium photodetector enhanced by a near-infrared dipole antenna," *Nat Photon,* 10.1038/nphoton.2008.30 vol. 2, no. 4, pp. 226-229, 04//print 2008.

[315] T. Matsui, A. Agrawal, A. Nahata, and Z. V. Vardeny, "Transmission resonances through aperiodic arrays of subwavelength apertures," *Nature,* vol. 446, no. 7135, pp. 517-521, 2007.

[316] C. A. Keasler and E. Bellotti, "A numerical study of broadband absorbers for visible to infrared detectors," *Applied Physics Letters,* vol. 99, no. 9, p. 091109, 2011.

[317] K. T. Posani *et al.*, "Nanoscale quantum dot infrared sensors with photonic crystal cavity," *Applied Physics Letters,* vol. 88, no. 15, p. 151104, 2006.

[318] V. N. Astratov, Allen Jr., Kenneth W. , Limberopoulos, Nicholaos I., Urbas, Augustine, Duran, Joshua M., "Photodetector focal plane array systems and methods," United States, 2016. Available: http://www.freepatentsonline.com/9362324.html.

[319] F. Abolmaali, A. Brettin, N. I. Limberopoulos, A. M. Urbas, and V. N. Astratov, "Use of photonic jets produced by dielectric microspheres for increasing sensitivity and angle-of-view of MWIR detectors," 2017, vol. 10107, pp. 101070V-101070V-7.

[320] F. Abolmaali, A. Brettin, A. Green, N. I. Limberopoulos, A. M. Urbas, and V. N. Astratov, "Photonic jets for highly efficient mid-IR focal plane arrays with large angle‐of‐view," *Optics Express,* vol. 25, no. 25, pp. 31174-31185, 2017/12/11 2017.

[321] Y. Sun and S. R. Forrest, "Organic light emitting devices with enhanced outcoupling via microlenses fabricated by imprint lithography," *Journal of Applied Physics,* vol. 100, no. 7, p. 073106, 2006.

[322] V. Astratov *et al.*, "Experimental technique to determine the band structure of two-dimensional photonic lattices," *IEE Proceedings-Optoelectronics,* vol. 145, no. 6, pp. 398-402, 1998.

[323] A. Bristow *et al.*, "Defect states and commensurability in dual-period Al x Ga 1− x As photonic crystal waveguides," *Physical Review B,* vol. 68, no. 3, p. 033303, 2003.

[324] A. Vlad, I. Huynen, and S. Melinte, "Wavelength-scale lens microscopy via thermal reshaping of colloidal particles," *Nanotechnology,* vol. 23, no. 28, p. 285708, 2012.

[325] D. Kang *et al.*, "Shape-Controllable Microlens Arrays via Direct Transfer of Photocurable Polymer Droplets," *Advanced Materials,* vol. 24, no. 13, pp. 1709-1715, 2012.

[326] G. Gu, R. Zhou, H. Xu, G. Cai, and Z. Cai, "Subsurface nano-imaging with self-assembled spherical cap optical nanoscopy," *Optics Express,* vol. 24, no. 5, pp. 4937-4948, 2016/03/07 2016.

[327] A. Darafsheh, G. F. Walsh, L. Dal Negro, and V. N. Astratov, "Optical super-resolution by high-index liquid-immersed microspheres," *Applied Physics Letters,* vol. 101, no. 14, p. 141128, 2012.

[328] K. W. Allen, "Waveguide, Photodetector, and Imaging Applications of Microspherical Photonics," University of North Carolina at Charlotte, 2014.

[329] K. W. Allen, Y. Li, and V. N. Astratov, "Reply to "Comment on 'Super-resolution microscopy by movable thin-films with embedded microspheres: Resolution analysis' [Ann. Phys. (Berlin) 527, 513 (2015)]"," *Annalen der Physik,* vol. 528, 2016.

[330] A. V. Maslov and V. N. Astratov, "Imaging of sub-wavelength structures radiating coherently near microspheres," *Applied Physics Letters,* vol. 108, no. 5, p. 051104, 2016.

[331] R. J. Potton, "Reciprocity in optics," *Reports on Progress in Physics,* vol. 67, no. 5, p. 717, 2004.

[332] J. L. Ponsetto, F. Wei, and Z. Liu, "Correction: Localized plasmon assisted structured illumination microscopy for wide-field high-speed dispersion-independent super resolution imaging," *Nanoscale,* 10.1039/C5NR90235E vol. 8, no. 6, pp. 3848-3848, 2016.

[333] J. G. Rivas, G. Vecchi, and V. Giannini, "Surface plasmon polariton-mediated enhancement of the emission of dye molecules on metallic gratings," *New Journal of Physics,* vol. 10, no. 10, p. 105007, 2008.

[334] M. G. L. Gustafsson *et al.*, "Three-Dimensional Resolution Doubling in Wide-Field Fluorescence Microscopy by Structured Illumination," *Biophysical Journal,* vol. 94, no. 12, pp. 4957-4970, 2008/06/15/ 2008.

[335] F. Ströhl and C. F. Kaminski, "Frontiers in structured illumination microscopy," *Optica,* vol. 3, no. 6, pp. 667-677, 2016/06/20 2016.

[336] J. L. Ponsetto, F. Wei, and Z. Liu, "Localized plasmon assisted structured illumination microscopy for wide-field high-speed dispersion-independent super resolution imaging," *Nanoscale,* 10.1039/C4NR00443D vol. 6, no. 11, pp. 5807-5812, 2014.

[337] F. Jünger, P. v. Olshausen, and A. Rohrbach, "Fast, label-free super-resolution live-cell imaging using rotating coherent scattering (ROCS) microscopy," *Scientific Reports,* vol. 6, p. 30393, 07/28

04/21/received

06/30/accepted 2016.

[338] A. V. Maslov and V. N. Astratov, "Optical nanoscopy with contact Mie-particles: Resolution analysis," *Applied Physics Letters,* vol. 110, no. 26, p. 261107, 2017.

[339] https://www.thermofisher.com/us/en/home/life-science/cell-analysis/fluorophores/pacific-green-dye.html. *Fluorescence Excitation/Emission of Pacific Green dye.*

[340] https://www.thermofisher.com/us/en/home/life-science/cell-analysis/fluorophores/pacific-blue-dye.html. *Fluorescence Excitation/Emission of Pacific Blue dye.*

[341] X. Hao, C. Kuang, X. Liu, H. Zhang, and Y. Li, "Microsphere based microscope with optical super-resolution capability," *Applied Physics Letters,* vol. 99, no. 20, p. 203102, 2011.

[342] L. Li, W. Guo, Y. Yan, S. Lee, and T. Wang, "Label-free super-resolution imaging of adenoviruses by submerged microsphere optical nanoscopy," *Light Sci Appl,* Original Article vol. 2, p. e104, 09/27/online 2013.

[343] H. Yang, N. Moullan, J. Auwerx, and M. A. M. Gijs, "Super-resolution biological microscopy using virtual imaging by a microsphere nanoscope," (in eng), *Small (Weinheim an der Bergstrasse, Germany),* vol. 10, no. 9, pp. 1712-1718, 2014/05// 2014.

[344] Y. Yan, L. Li, C. Feng, W. Guo, S. Lee, and M. Hong, "Microsphere-Coupled Scanning Laser Confocal Nanoscope for Sub-Diffraction-Limited Imaging at 25 nm Lateral Resolution in the Visible Spectrum," *ACS Nano,* vol. 8, no. 2, pp. 1809-1816, 2014/02/25 2014.

[345] Z. H.-J. Wang Shu-Ying, Zhang Dong-Xian, "Location-free optical microscopic imaging method with high-resolution based on microsphere superlenses," *Acta Physica Sinica,* vol. 62, no. 3, p. 34207, 1900-01-01 2013.

[346] L. A. Krivitsky, J. J. Wang, Z. Wang, and B. Luk'yanchuk, "Locomotion of microspheres for super-resolution imaging," *Scientific Reports,* Article vol. 3, p. 3501, 12/16/online 2013.

[347] K. Allen, N. Farahi, Y. Li, and V. Astratov, *Super-resolution by microspheres and fibers - Myth or reality?* 2015.

[348] W. V. Houston, "A Compound Interferometer for Fine Structure Work," *Physical Review,* vol. 29, no. 3, pp. 478-484, 03/01/ 1927.

[349] T. Hutter, F. M. Huang, S. R. Elliott, and S. Mahajan, "Near-Field Plasmonics of an Individual Dielectric Nanoparticle above a Metallic Substrate," *The Journal of Physical Chemistry C,* vol. 117, no. 15, pp. 7784-7790, 2013/04/18 2013.

[350] Z. Liu *et al.*, "Far-Field Optical Superlens," *Nano Letters,* vol. 7, no. 2, pp. 403-408, 2007/02/01 2007.

[351] X. Wang, W. Shi, G. She, and L. Mu, "Surface-Enhanced Raman Scattering (SERS) on transition metal and semiconductor nanostructures," *Physical Chemistry Chemical Physics,* 10.1039/C2CP40080D vol. 14, no. 17, pp. 5891-5901, 2012.

[352] T. Yuto and O. Minoru, "Comparison of Resonant Plasmon Polaritons with Mie Scattering for Laser-Induced Near-Field Nanopatterning:

Metallic Particle vs Dielectric Particle," *Japanese Journal of Applied Physics,* vol. 48, no. 12R, p. 122002, 2009.

[353] S. Law, V. Podolskiy, and D. Wasserman, "Towards nano-scale photonics with micro-scale photons: the opportunities and challenges of mid-infrared plasmonics," in *Nanophotonics* vol. 2, ed, 2013, p. 103.

[354] G. Pellegrini, G. Mattei, and P. Mazzoldi, "Light Extraction with Dielectric Nanoantenna Arrays," *ACS Nano,* vol. 3, no. 9, pp. 2715-2721, 2009/09/22 2009.

[355] A. Devilez, B. Stout, and N. Bonod, "Compact Metallo-Dielectric Optical Antenna for Ultra Directional and Enhanced Radiative Emission," *ACS Nano,* vol. 4, no. 6, pp. 3390-3396, 2010/06/22 2010.

[356] M. K. Schmidt, R. Esteban, J. J. Sáenz, I. Suárez-Lacalle, S. Mackowski, and J. Aizpurua, "Dielectric antennas - a suitable platform for controlling magnetic dipolar emission," *Optics Express,* vol. 20, no. 13, pp. 13636-13650, 2012/06/18 2012.

[357] F. Abolmaali, N. I. Limberopoulos, A. M. Urbas, and V. N. Astratov, "Design and optimization of focal plane arrays integrated with dielectric microspheres," in *2016 IEEE National Aerospace and Electronics Conference (NAECON) and Ohio Innovation Summit (OIS)*, 2016, pp. 258-261.

[358] F. Abolmaali, A. Brettin, N. I. Limberopoulos, A. M. Urbas, and V. N. Astratov, "Use of photonic jets produced by dielectric microspheres for increasing sensitivity and angle-of-view of MWIR detectors," in *SPIE OPTO*, 2017, vol. 10107, p. 7: SPIE.

APPENDIX: LIST OF PUBLICATIONS

Journal Articles:

1. K. W. Allen, A. Darafsheh, **F. Abolmaali**, N. Mojaverian, N. I. Limberopoulos, A. Lupu, and V. N. Astratov, “Microsphere-chain waveguides: Focusing and transport properties,” Applied Physics Letters 105, 021112 (2014).

2. K. W. Allen, **F. Abolmaali**, J. M. Duran, G. Ariyawansa, N. I. Limberopoulos, A. M. Urbas, and V. N. Astratov, “Increasing sensitivity and angle-of-view of mid-wave infrared detectors by integration with dielectric microspheres,” Applied Physics Letters 108, 241108 (2016).

3. Y. Li, **F. Abolmaali**, K. W. Allen, N. I. Limberopoulos, A. Urbas, Y. Rakovich, A. V. Maslov, and V. N. Astratov, “Whispering gallery mode hybridization in photonic molecules,” Laser & Photonics Reviews 11, 1600278 (2017).

4. **F. Abolmaali**, A. Brettin, A. Green, N. I. Limberopoulos, A. M. Urbas, and V. N. Astratov, “Photonic jets for highly efficient mid-IR focal plane arrays with large angle-of-view,” Opt. Express 25, 31174-31185 (2017).

5. **F. Abolmaali** et al., “Observation and Analysis of the Nanoplasmonic Contributions to the Super-Resolution of Dye Doped Nanospheres” Optics Letter (to be submitted).

6. **F. Abolmaali** et al., “Resonant routing and asymmetric transmission properties of coupled-cavity structures: Design and analysis” Optics Express (to be submitted).

Conference Proceedings:

1. Y. Li, K. W. Allen, **F. Abolmaali**, A. V. Maslov, and V. N. Astratov, "Spectral finger-prints of photonic molecules," in 2014 16th International Conference on Transparent Optical Networks (ICTON)(2014), pp. 1-4.
2. **F. Abolmaali**, N. I. Limberopoulos, A. M. Urbas, and V. N. Astratov, "Observation of the influence of the gain on parity-time-symmetric properties of photonic molecules with coupled whispering gallery modes," in 2015 National Aerospace and Electronics Conference (NAECON)(2015), pp. 106-109.
3. Y. Li, **F. Abolmaali**, N. I. Limberopoulos, A. M. Urbas, and V. N. Astratov, "Coupling properties and sensing applications of photonic molecules," in 2015 National Aerospace and Electronics Conference (NAECON)(2015), pp. 102-105.
4. **F. Abolmaali**, N. I. Limberopoulos, A. M. Urbas, and V. N. Astratov, "Design and optimization of focal plane arrays integrated with dielectric microspheres," in 2016 IEEE National Aerospace and Electronics Conference (NAECON) and Ohio Innovation Summit (OIS)(2016), pp. 258-261.
5. V. N. Astratov, **F. Abolmaali**, A. Brettin, K. W. Allen, A. V. Maslov, N. I. Limberopoulos, D. E. Walker, and A. M. Urbas, "Label-free nanoscopy with contact microlenses: Super-resolution mechanisms and limitations," in 2016 18th International Conference on Transparent Optical Networks (ICTON)(2016), pp. 1-4.
6. **F. Abolmaali**, N. I. Limberopoulos, A. M. Urbas, and V. N. Astratov, "Resonance-based optical routing and nonreciprocity in photonic molecules with coupled whispering gallery modes," in 2016 IEEE National Aerospace and Electronics Conference (NAECON) and Ohio Innovation Summit (OIS)(2016), pp. 292-295.
7. A. Brettin, **F. Abolmaali**, N. I. Limberopoulos, D. E. Walker, A. M. Urbas, and V. N. Astratov, "Imaging of two-dimensional nanoplasmonic structures by nanoscopy with contact microlenses and various microscope objectives," in 2016 IEEE National Aerospace and Electronics Conference (NAECON) and Ohio Innovation Summit (OIS)(2016), pp. 272-274.
8. A. Brettin, **F. Abolmaali**, N. I. Limberopoulos, D. E. Walker, A. M. Urbas, and V. N. Astratov, "Superresolution imaging with contact

microspheres: Importance of numerical aperture," in 2016 18th International Conference on Transparent Optical Networks (ICTON)(2016), pp. 1-4.

9. **F. Abolmaali**, Y. Li, A. Lupu, M. Tchernycheva, A. V. Maslov, N. I. Limberopoulos, A. M. Urbas, and V. N. Astratov, "Identification of whispering gallery modes in a fiber based sensor platform," in 2017 IEEE National Aerospace and Electronics Conference (NAECON)(2017), pp. 284-287.
10. **F. Abolmaali**, Y. Li, K. W. Allen, N. I. Limberopoulos, A. M. Urbas, Y. Rakovich, A. V. Maslov, and V. N. Astratov, "Photonic molecules and sensors based on coupling between whispering gallery modes in microspheres," in 2017 IEEE National Aerospace and Electronics Conference (NAECON)(2017), pp. 205-208.
11. **F. Abolmaali**, Y. Li, K. Allen, N. I. Limberopoulos, A. M. Urbas, Y. Rakovich, A. V. Maslov, and V. Astratov, "Spectral signatures of photonic molecules with hybridized whispering gallery modes," (2017).
12. **F. Abolmaali**, A. Brettin, N. I. Limberopoulos, A. M. Urbas, and V. N. Astratov, "Use of photonic jets produced by dielectric microspheres for increasing sensitivity and angle-of-view of mwir detectors," in SPIE OPTO(SPIE2017), p. 7.
13. **F. Abolmaali**, N. I. Limberopoulos, A. M. Urbas, A. V. Maslov, and V. N. Astratov, "Resonant routing of optical pulses in coupled-cavity structures," in SPIE OPTO(SPIE2017), p. 7.

14. V. N. Astratov, A. Brettin, **F. Abolmaali**, C. L. McGinnis, K. F. Blanchette, Y. E. Nesmelov, A. V. Maslov, N. I. Limberopoulos, D. E. Walker, and A. M. Urbas, "Spotlight on microspherical nanoscopy: Experimental quantification of super-resolution," in 2017 19th International Conference on Transparent Optical Networks (ICTON)(2017), pp. 1-4.